



저작자표시-비영리-변경금지 2.0 대한민국

이용자는 아래의 조건을 따르는 경우에 한하여 자유롭게

- 이 저작물을 복제, 배포, 전송, 전시, 공연 및 방송할 수 있습니다.

다음과 같은 조건을 따라야 합니다:



저작자표시. 귀하는 원저작자를 표시하여야 합니다.



비영리. 귀하는 이 저작물을 영리 목적으로 이용할 수 없습니다.



변경금지. 귀하는 이 저작물을 개작, 변형 또는 가공할 수 없습니다.

- 귀하는, 이 저작물의 재이용이나 배포의 경우, 이 저작물에 적용된 이용허락조건을 명확하게 나타내어야 합니다.
- 저작권자로부터 별도의 허가를 받으면 이러한 조건들은 적용되지 않습니다.

저작권법에 따른 이용자의 권리는 위의 내용에 의하여 영향을 받지 않습니다.

이것은 [이용허락규약\(Legal Code\)](#)을 이해하기 쉽게 요약한 것입니다.

[Disclaimer](#)

Doctor of Philosophy

**Conductive polymer composite (polypyrrole, MXene) used as fillers for
water-based binder on electrochemical double-layer capacitor
electrode and lithium-ion battery**

The Graduate School of the University of Ulsan

Department of Chemical Engineering

Yanchunxiao Qi

**Conductive polymer composite (polypyrrole, MXene) used as fillers for
water-based binder on electrochemical double-layer capacitor
electrode and lithium-ion battery**

Supervisor: Professor Eun-Suok Oh

A Dissertation

Submitted to the Graduate School of the University of Ulsan

In partial Fulfillment of the Requirements for the Degree of Doctor of Philosophy

By

Yanchunxiao Qi

Department of Chemical Engineering and Bioengineering

May 2021

Conductive polymer composite (polypyrrole,
MXene) used as fillers for water-based binder
on electrochemical double-layer capacitor
electrode and Lithium-ion battery

Thesis for the degree of Doctor of Philosophy

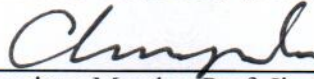
by

Yanchunxiao Qi

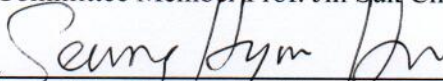
Has been approved



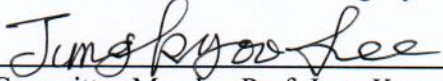
Committee Chair Prof. Won Mook Choi



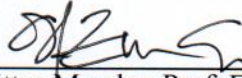
Committee Member Prof. Jin Suk Chung



Committee Member Prof. Seung Hyun Hur



Committee Member Prof. Jung Kyoo Lee



Committee Member Prof. Eun-Suok Oh

Department of Chemical Engineering and Bioengineering

University of Ulsan

May 2021

ABSTRACT

In view of global warming effect and the depletion of fossil fuels, the development of efficient energy storage and conversion devices are highly recommended. Besides, electrochemical energy storage devices are gaining rising importance due to applications in electric vehicles (EV) and hybrid electric vehicles (HEV). Lithium-ion battery (LIB) has high energy density and give attractions to many researchers. Thus, it is widely used in popular electronics devices such as cell phones, laptops, etc. For reach a higher capacity, many active materials have been studied, such as graphite and other carbonaceous materials, Si, Al, Sn and so on. Supercapacitors are widely used for EV, HEV braking and power supply system, memory backup for portable electronics, and other high current demanding applications by their high-power density. Among the supercapacitors, the electrochemical double-layer capacitor (EDLC) is the most studied. EDLC can reach a high energy density by its active material large surface area. Thus, many researchers studied on increasing the active material surface area. However, there is less attention was paid to the binder even though it played a critical role on the performance of lithium-ion batteries, and supercapacitors. Thus, in this study, we introduced conductive polypyrrole and new 2D material MXene as fillers and added to high adhesive water-based poly (butyl acrylate/acrylonitrile) (PANBA) and Poly(methyl methacrylate- butylacrylate-methacrylic acid/acrylonitrile-butylacrylate-styrene) (PMAA-BA-MMA/AN-BA-St) and applied on lithium-ion battery and supercapacitors, respectively. These water based conductive polymer named as PANBA-PPyX, MX/PANBA, MX/CS and MX/HCS were synthesized via emulsion polymerization, and they were used as binder on anode electrodes for LIB and electrodes for EDLCs in CR2032 type coin cells. Both physical and chemical tests had been studied and confirmed that PANBA-PPyX and MX/PANBA were high adhesive, good conductive, better capacity retention environmentally friendly water-based binder for LIB and EDLCs.

In PANBA-PPyX study, we use it for EDLC electrodes first. The use of the new PANBA-PPyX binder increases the specific capacitance of the EDLC electrode up to 109.7 F g^{-1} from the 101.0 F g^{-1} value of the nonconductive PANBA-containing EDLC

electrode at 10,000 cycles. This is mainly attributed to the better dispersion and lower electrical resistance of the PANBA-PPyX binder without losing the thermal, ion transport, and binding characteristics of the PANBA. For PANBA-PPyX binder applied on LIB study, The electrochemical performance of the conductive copolymers as a binder for the $\text{Li}_4\text{Ti}_5\text{O}_{12}$ (LTO) anodes of lithium-ion batteries was superior to the non-conductive PANBA binder. The LTO electrode containing the PANBA-PPy4 binder, which was copolymerized with 4 g of pyrrole in 30 g of PANBA, had lower charge transfer and electrical resistance and thus better initial discharge capacity, coulombic efficiency, and capacity retention during the charge/discharge process at a 1 C current rate than the other electrodes containing the other conductive PANBA-PPy binders and non-conductive PANBA binder. In contrast, PANBA-PPy2 showed remarkable performance in the high current rate cycling test: discharge capacities of 152 mAh g^{-1} and 136 mAh g^{-1} at 5C and 10 C, respectively. This is because PANBA-PPy2 has stronger adhesion capability than PANBA-PPy4 that allows it to endure the impact caused by the high current density.

In MX/PANBA binder applied on EDLCs study which is a first report of an in-situ polymerization method to make a conducting composite binder with enhanced mechanical, adhesion, and electronic conducting properties. An EDLC containing electrodes of activated carbon and MXene clay/PANBA composite binder shows a high specific power of 8510 W kg^{-1} with a high specific energy of 23.6 Wh kg^{-1} . This is a significant improvement over EDLC electrodes containing only activated carbon and PANBA. The improved performance is attributed to the binder's enhanced conductivity and toughness due to improved interactions among the electrode components. Moreover, it shows prior performance when MX/PANBA binder applied on LTO anode for LIB as well.

In MX/CS and MX/HCS binder applied on EDLCs studies, a series physical tests and electrochemical tests have been conducted. And the results approved that they can be used as potential water-based binder for energy storage devices since their good mechanical property and adhesive property.

Overall, both the polypyrrole and MXene can be used as the conductive filler for polymer composite with polymer matrix PANBA, core-shell and hollow core-shell polymer matrix. The emulsion polymerization is an effective way to synthesis polymer

composite at the present of fillers. The addition of polypyrrole and MXene can increase not only polymer matrix's conductivity obviously but also can improve the composite polymer matrix's mechanical property, such as relative toughness. When they used as binder for energy storage system, they can show good electrochemical stability. There is not any chemical reaction happened in a wide voltage range. In addition, the study of conductive polymer binder can help to decrease the charge transfer resistance and to increase the discharge capacitance of EDLCs resulting in improve the energy density and power density of energy devices. It is necessary to develop different properties of binder by different applications. Therefore, for increasing the fast charge discharge properties of binder, it is an imperative study to develop the conductivity of binder by using the various conductive fillers and making them into polymer composite.

ACKNOWLEDGMENTS

Spending years studying in Ulsan university is a great memory in my life. I have studied a lot in Korea, not only the scientific life, but a also a personal life. For all the people around me give me much help, I can be graduate as a Ph.D student.

First of all, I most gratitude to my advisor Professor Dr. Eun-Suok Oh. During these years, he gave me so many helpful advices to be a researcher. When I came to Ulsan university at first, I didn't have any idea about how to study on electrical chemistry. However, following his leading, I have grown up from an undergraduate student to a Ph.D student. Besides, professor usually asks us to enjoy our life in Korea, that means he really care about our life conditions in Korea as a foreigner. He is the kindest professor I have ever seen. And at the same time, he is so knowledgeable that can give us accurate suggestions promptly, this is so useful on our research. Next, I want to say thanks to all of my lab mates, they also gave me many helps to study in lab. Particularly, I intend to appreciate to Hien who studied as a post doctor in our lab. She taught me a lot, contain experiments methods and the ways of thinking as a researcher. She let me to see far more than I think. And she is so kind that I should learn more. Then, I would like to thank all of our department committee members. From their classes I took, I have learned a lot which is important for my research.

At last, I want to thanks to my family and my friends. Thank to them, I have power to continue my study, especially when I stuck in my research. They are the most treasure possession in my life.

TABLE OF CONTENTS

CHAPTER 1: Introduction.....	1
1.1 Motivation	1
1.2 Objectives	2
CHAPTER 2: Background	3
2.1 Lithium ion battery (LIB)	3
2.2 Components of LITHIUM-ION Batteries	5
2.2.1 Anode.....	5
2.2.2 Cathode	6
2.2.3 Electrolyte	6
2.3 Supercapacitors	7
2.4 Components of EDLCs	9
2.4.1 Electrode	9
2.4.2 Electrolyte.....	9
2.5 Role of Polymeric Binder in Electrodes of LIB and EDLCs	10
2.6 Classification of Polymeric Binders	12
2.6.1 Organic solvent-based binder	12
2.6.2 Water-based binder	13
2.7 Water-based conductive binder for LIB anode and EDLCs	14
2.8 In-Situ Emulsion polymerization	17
CHAPTER 3: Experimental.....	19
3.1 Synthesis of Poly (acrylonitrile/butyl acrylate)-Polypyrrole by in-situ emulsion polymerization.	19
3.2 Synthesis of polypyrrole-poly (acrylonitrile-butyl acrylate) by in-situ emulsion polymerization.	19

3.3	Synthesis of MXene/poly(acrylonitrile-butyl acrylate) by in-situ emulsion polymerization.	19
3.4	Synthesis of MXene/ core shell structured poly(styrene-acrylonitrile-butyl acrylate) by In-situ emulsion polymerization.	20
3.5	Synthesis of MXene/ Hollow core shell structured poly(styrene-acrylonitrile-butyl acrylate) by In-situ emulsion polymerization.	20
3.6	Electrode preparation and cell assembly	22
3.6.1	Lithium titanium oxide (LTO) anode electrode.....	22
3.6.2	EDLCs electrode.....	23
3.6.3	Cell assembly.....	23
3.7	Binder characterization	24
3.7.1	Sheet resistance analysis.....	24
3.7.2	Fourier-transform infrared analysis (FTIR).....	24
3.7.3	Raman analysis.....	24
3.7.4	Transmission electron microscopy (TEM).....	24
3.7.5	Scanning electron microscope analysis (SEM).....	24
3.7.6	Thermogravimetric analysis.....	24
3.7.7	Differential Scanning Calorimetry.....	25
3.7.8	Zeta potential analysis.....	25
3.7.9	Contact angle.....	25
3.7.10	Electrolyte uptake.....	25
3.8	Electrode characterization	25
3.8.1	Adhesion strength.....	25
3.8.2	Brunauer Emmett-Teller (BET) analysis.....	25
3.9	Electrochemical properties	26
	CHAPTER 4: Results and discussion	27
4.1	Poly (Acrylonitrile-Butyl Acrylate)-Polypyrrole	27

4.1.1	Physical properties	27
4.1.1.1	Stability and TEM	27
4.1.1.2	FTIR	29
4.1.1.3	Sheet resistance	29
4.1.1.4	TGA	31
4.1.1.5	Contact angle	32
4.1.1.6	Adhesive test	33
4.1.2	Electrochemical properties	34
4.1.2.1	Cycling performance	34
4.1.2.2	Electrochemical impedance spectra (EIS) performance	35
4.1.2.3	High rate performance	36
4.2	Polypyrrole-Poly (Acrylonitrile-Butyl Acrylate)	38
4.2.1	Physical properties	38
4.2.1.1	Stability	38
4.2.1.2	FTIR	39
4.2.1.3	Resistance test by electrochemical impedance spectra (EIS)	40
4.2.1.4	TGA	41
4.2.1.5	Zeta potential	42
4.2.1.6	Contact angle (CA)	43
4.2.1.7	Adhesion strength	44
4.2.1.8	BET	45
4.2.2	Electrochemical properties	47
4.2.2.1	CV	47
4.2.2.2	Electrochemical impedance spectroscopy (EIS) performance	48
4.2.2.3	Cycling performance	49
4.2.2.4	High-rate performance	50

4.3	MXene-Poly (Acrylonitrile-Butyl Acrylate)	51
4.3.1	Physical properties	51
4.3.1.1	Raman.....	51
4.3.1.2	FTIR	53
4.3.1.3	Zeta Potential.....	54
4.3.1.4	SEM.....	55
4.3.1.5	DSC	56
4.3.1.6	Polymer sheet resistance test by IMP.....	57
4.3.1.7	BET	58
4.3.1.8	Adhesive test	60
4.3.2	Electrochemical properties.....	61
4.3.2.1	Cycling performance of EDLCs without conducting agent inside ...	61
4.3.2.2	IMP performance of EDLCs without conducting agent inside	62
4.3.2.3	Cycling performance of EDLCs with conducting agent inside.....	63
4.3.2.4	IMP performance of EDLCs with conducting agent inside	64
4.3.2.5	EDLCs charge discharge profile	66
4.3.2.6	EDLCs CV profile.....	68
4.3.2.7	High-rate performance of EDLCs with conducting agent inside.....	70
4.3.2.8	Ragone plot of EDLCs	71
4.4	MXene/ Core Shell Structured Poly (Styrene-Acrylonitrile-Butyl Acrylate)	72
4.4.1	Physical properties	72
4.4.1.1	Raman and FTIR	72
4.4.1.2	SEM.....	73
4.4.1.3	Contact angle.....	74
4.4.1.4	Thermal property of binder film.....	76

4.4.1.5	Ion conductivity of binder solution and sheet resistance of binder film	77
4.4.1.6	CV of binder film	78
4.4.1.7	Electrode adhesive property	79
4.4.1.8	BET	80
4.4.2	Electrochemical properties.....	81
4.4.2.1	CV	81
4.4.2.2	IMP.....	82
4.4.2.3	Cycling and high rate performance	83
4.5	MXene/ Hollow Core Shell Structured Poly (Styrene-Acrylonitrile- Butyl Acrylate)	84
4.5.1	Physical properties	84
4.5.1.1	Raman and FTIR	84
4.5.1.2	SEM.....	87
4.5.1.3	Contact angle.....	88
4.5.1.4	Thermal property of binder film.....	90
4.5.1.5	Ion conductivity of binder solution	91
4.5.1.6	Electrode adhesive property	92
4.5.1.7	BET	93
4.5.2	Electrochemical properties.....	94
4.5.2.1	CV of EDLCs with different binder	94
4.5.2.2	IMP of EDLCs	95
4.5.2.3	Cycling and high-rate performance of EDLCs	96
CHAPTER 5: Conclusions.....		99
CHAPTER 6: References.....		101

FIGURE LIST

Figure 1: Structure and principle of lithium ion battery.....	4
Figure 2: Basic schematics of EDLC, pseudocapacitor and LIB.	8
Figure 3: EDLC charge and discharge mechanism.	8
Figure 4: Typical anode of LIB.	11
Figure 5: Calculated redox windows of various polymers.....	11
Figure 6: Mechanism of binder safety operating voltage.....	12
Figure 7: Conceptual illustration of binding between PVdF and active material.	13
Figure 8: The graphic abstract of PANBA-PPy binder applied on LTO electrode for LIB anode.....	16
Figure 9: The graphic abstract of MX/PANBA binder applied on EDLCs electrodes. .	16
Figure 10: The graphic abstract of MX/Hollow core shell binder.	17
Figure 11: Schematic diagram of emulsion polymerization mechanism.	18
Figure 12: Chemical structures of hollow core shell polymer.....	22
Figure 13: The process of LTO electrode preparation and cell assembly.....	22
Figure 14: The process of EDLCs electrode preparation and cell assembly.....	23
Figure 15: Stability and TEM.....	28
Figure 16: FT-IR spectra of PPy, PANBA, and PANBA-PPy2 binder films.	30
Figure 17: TGA results of the PANBA-PPy samples and PPy.	31
Figure 18: Contact angle of an electrolyte droplet placed on the binder films as a function of time.....	32
Figure 19: 180° peel strength of the LTO electrodes containing different PANBA-PPy samples as a binder.....	33
Figure 20: Cycling performance of the Li ₄ Ti ₅ O ₁₂ electrodes at rates of 0.1C for the first two cycles and 1C for the subsequent 100 cycles.	34
Figure 21: Electrochemical impedance spectra (EIS) of the Li ₄ Ti ₅ O ₁₂ electrodes after charging and discharging at 0.1C for two cycles and 0.5C for a further three cycles....	35
Figure 22: High rate performance.	37
Figure 23: Turbiscan stability index of polymer solution displayed in one day.	38
Figure 24: FTIR spectrum of binder film.	39

Figure 25: The resistance of polymer film examined by electrochemical impedance spectra (EIS).	40
Figure 26. (a) DSC and (b) TGA of the polymer films. Here, PPy+PANBA(phy) indicates the PANBA mixed physically with 1 wt% PPy.	41
Figure 27: Contact angle of binder film.	43
Figure 28: The adhesion strength value of SBR, PANBA, and PPyANBA supercapacitor electrodes with an error bar.	44
Figure 29: BET results.....	46
Figure 30: Cyclic voltammograms (CV) of the CR 2032 supercapacitors at various scan rates, 5 mV/s, 20 mV/s, 50 mV/s, 100 mV/s.....	47
Figure 31: Nyquist plot of supercapacitor with the frequency from 10^6 Hz to 10^{-2} Hz at 0 V after 200 cycles.	48
Figure 32: EDLCs cycling performance with different binder systems for 10,000 cycles.	49
Figure 33: EDLCs rate capability performance with different binder system for 20 cycles at each current.....	50
Figure 34: Raman spectra of PANBA, MXCs/PANBA binder film and MXenes.	52
Figure 35: FT-IR spectra of PANBA, MXCs/PANBA binder film.	53
Figure 36: FE-SEM images.....	55
Figure 37: Nyquist diagram of polymer membrane and linear correlation with Equivalent circuit (upper right corner).	57
Figure 38: BET results.....	59
Figure 39: The adhesion strength of PANBA, and MXs/PANBA EDLCs electrodes with error bars.....	60
Figure 40: Cycling performance of none conducting agent symmetrical EDLCs.	61
Figure 41: IMP profile of none conducting agent symmetrical EDLC after charge/discharge 250 cycles and fitting with equivalent circuit insert.....	62
Figure 42: EDLCs cycling performance with different binder for 10,000 cycles and charge/discharge schematic demonstration.	63
Figure 43: Nyquist plot of EDLCs with the frequency from 10^6 Hz to 10^{-2} Hz at $E = 0$ V after 10,000 cycles, and fitting with equivalent circuit insert.	65
Figure 44: EDLCs charge/discharge profile at $I = 1.54$ mA between 0.1 – 2.7 V.	67

Figure 45: Enlarged EDLCs charge/discharge profile for IR drop calculation.	67
Figure 46: Cyclic voltammetry of EDLCs.	69
Figure 47: EDLCs rate capability performance.	70
Figure 48: The ragone plot of EDLCs.	71
Figure 49: The Raman spectra (left) and FTIR (right) of polymer film.	72
Figure 50: (a) Polymer after dry (b,c) SEM image of polymer (d) TEM image of polymer € SEM image of MX/CS.	73
Figure 51: Contact angle of an electrolyte droplet fell onto the binder films during the 60 s.	75
Figure 52: Thermogravimetry (TGA) of polymer film.	76
Figure 53: Ion conductivity of polymer solution.	77
Figure 54: Cyclic voltammetry (CV) of binder film coating on e-Al foil.	78
Figure 55: The adhesion strength value of electrodes of different binder with an error bar.	79
Figure 56: (up) Nitrogen adsorption/desorption isotherms curves of supercapacitor electrodes excluding current collectors; (down) Electrodes pore diameter distribution based on the BJH method.	80
Figure 57: Cyclic voltammetry (CV) of EDLCs.	81
Figure 58: Nyquist plot of EDLCs with the frequency from 10^6 Hz to 10^{-2} Hz at E = 0 V after 10,000 cycles.	82
Figure 59: EDLCs cycling performance(left), high rate performance(right) with different binder.	83
Figure 60: Raman spectra of polymer film.	85
Figure 61: FT-IR spectra of polymer film.	86
Figure 62: (a) Polymer after dry (b,c) SEM image of hollow core-shell polymer.	87
Figure 63: Contact angle of an electrolyte droplet fell down onto the binder films during the 60 s.	88
Figure 65: Thermogravimetry (TGA) of polymer film.	90
Figure 66: Ion conductivity of polymer solution.	91
Figure 67: The adhesion strength value of electrodes of different binder with an error bar.	92

Figure 68: (up) Nitrogen adsorption/desorption isotherms curves of supercapacitor electrodes excluding current collectors; (down) Electrodes pore diameter distribution based on the BJH method.	93
Figure 70: Cyclic voltammetry (CV) of EDLCs.	94
Figure 71: Nyquist plot of EDLCs with the frequency from 10^6 Hz to 10^{-2} Hz at $E = 0$ V after 10,000 cycles.	95
Figure 72: EDLCs cycling performance with different binder for 2500 cycles.	97
Figure 73: EDLCs rate capability performance with different binder for 20 cycles at each current.	98

TABLE LIST

Table 1: Recipe of the hollow core shell polymer.....	21
Table 2: Sheet resistance of the PANBA-PPy samples containing different amounts of polypyrrole.	30
Table 3: Zeta potential and glass transition temperature of PANBA and PPyANBA. ..	42
Table 4: Porosity parameters of supercapacitor electrodes.	46
Table 5: Zeta potential of polymer solution.	54
Table 6: Glass transition temperature of polymer films.	56
Table 7: Porosity parameters of supercapacitor electrodes excluding collectors.....	59
Table 8: X-intercept of none conducting agent symmetrical EDLCs by IMP profile data fitting after charge/discharge 250 cycles.	62
Table 9: EDLCs charge transfer resistance.	65
Table 10: EDLCs equivalent series resistance (ESR) calculation via its enlarged charge/discharge profile.	67
Table 11: EDLCs coulombic efficiency (CE) calculated by cyclic voltammogram.	69
Table 12: Contact angle change of an electrolyte droplet fell onto the binder films during the 60 s.....	75
Table 13: Glass transition temperature of different polymer.	76
Table 14: Sheet resistance of different polymer.	77
Table 15: Porosity information of EDLCs electrodes with different binder.	80
Table 16: Contact angle change of an electrolyte droplet fell onto the binder films during the 60 s.....	89
Table 17: Glass transition temperature of different polymer.	90
Table 18: Porosity information of EDLCs electrodes with different binder.	93

CHAPTER 1: INTRODUCTION

1.1 MOTIVATION

In recent years, for the increase in environmental problems and the consumption of fossil fuels, people pay much attention on the eco-friendly energy storage. In dozens of years, the electric vehicles (EV) and hybrid electric vehicle (HEV) become more popular than before. They are considered as promising communication media in the future[1]–[3]. Besides, portable devices are also a vital part of our daily life. As a result, many researchers pay much attention on lithium ion battery (LIB), and supercapacitors. For receiving high energy density, LIB is used in almost all electronics devices in our life, such as laptops, cell phone power recharger, and especially smart phones have large demanded on good performance lithium ion batteries for higher capacity[4], [5]. Supercapacitor is different with LIB, it can support a large power density, thus supercapacitors are used for different applications, such as EV, HEV braking and power supply system, memory backup for portable electronics, and other high current demanding applications[6]–[8].

To get a good LIB or supercapacitors electrochemical performance, binder played a critical role. Because binder system is the connection between active materials and collectors, and among active materials and other additives in electrodes[9], [10]. Generally, active materials, for example, graphite, silicon, lithium titanium oxide ($\text{Li}_4\text{Ti}_5\text{O}_{12}$, LTO), and so on. Volumetric change usually happens during charge and discharge which is caused by the lithium ions insertion and emigration. Thus, the binder system cannot be neglected in LIB and supercapacitors.

Nowadays, there are many researchers working on the adhesive strength rather than on binder's conductive property. A conductive binder can give more electron pathways during discharging/charging. Resulting the electrons can transfer easily and making high rate discharging/charging possible.

So, in this study, we focus on improving the binder conductivity with high adhesive binder poly (acrylonitrile-butyl acrylate) (PANBA) which synthesized by our previous work[11] and applied the binder on electrode for LIB and supercapacitors. Physical performance and electrochemical characteristics have been studied.

1.2 OBJECTIVES

Nowadays, there are so many studies on the polymeric binder adhesive properties, because the volume change during discharge/charge processes compound the LIB and supercapacitors performance. However, as time goes by, many portable devices require fast charging and discharging. For overcoming this issue, in this study, we introduce the conducting polymer and 2D materials into high adhesive poly(acrylonitrile-butyl acrylate) (PANBA) water-based binder used in electrode for $\text{Li}_4\text{Ti}_5\text{O}_{12}$ (LTO) anodes of lithium-ion battery (LIB) and symmetrical electrochemical double-layer capacitors (EDLCs). These conductive binders were synthesized via emulsion polymerization.

Ultimately, the conducting, environmentally friendly, high discharge capacity at high rate current, good capacity retention and high adhesive strength binder has been synthesized in this research. And make polypyrene possible to use as binder in LIB, new 2D material MXene can apply on EDLCs.

CHAPTER 2: BACKGROUND

2.1 LITHIUM ION BATTERY (LIB)

Batteries is a device which can transfer chemical energy to electrical energy by electrochemical reactions. The modern batteries can be controlled well in applications, and they discovered by Alessandro Giuseppe Antonio Anastasio Volta in 19th century called Volta Pile. Batteries can be sort by different ways.

By its charging method, batteries can be classified in two types: primary battery and secondary battery. Primary battery cannot be recharged after using while secondary battery can be recharged many times after power off. The common secondary batteries are lead-acid battery, the nickel-cadmium battery (Ni-Cd), the nickel metal hydride battery (Ni-MH) and Lithium ion battery (LIB)[12]. Except LIB, all of the rechargeable batteries give working electrical potential as 1.2V, whereas LIB shows the highest constant voltage of 3.6-3.7V. Compared with other secondary batteries, LIB has higher gravimetric capacity, and there isn't any memory effect on LIB. With low self-discharge and environment friendly property, LIB is considered as the most promote secondary battery, and nowadays, there are many applications based on LIB including portable electrical devices, and electric vehicle[12].

LIB is constituted with cathode, anode, separator, electrolyte. And the normal cathode materials used on LIB are lithium cobalt oxides, lithium manganate (VI), lithium iron phosphate, fluorinated lithium iron phosphate and so on. LIB works simply, the positive side and negative side which separated by separator are put into organic liquid electrolyte or solid electrolyte and connected with other electricity devices. Based on the redox reaction on the cathode and anode, lithium ions transfer between cathode and anode during discharging and charging processes as shows in Fig. 1.

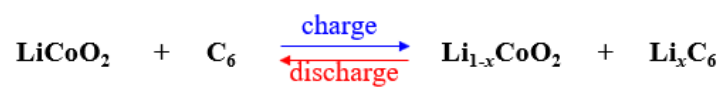
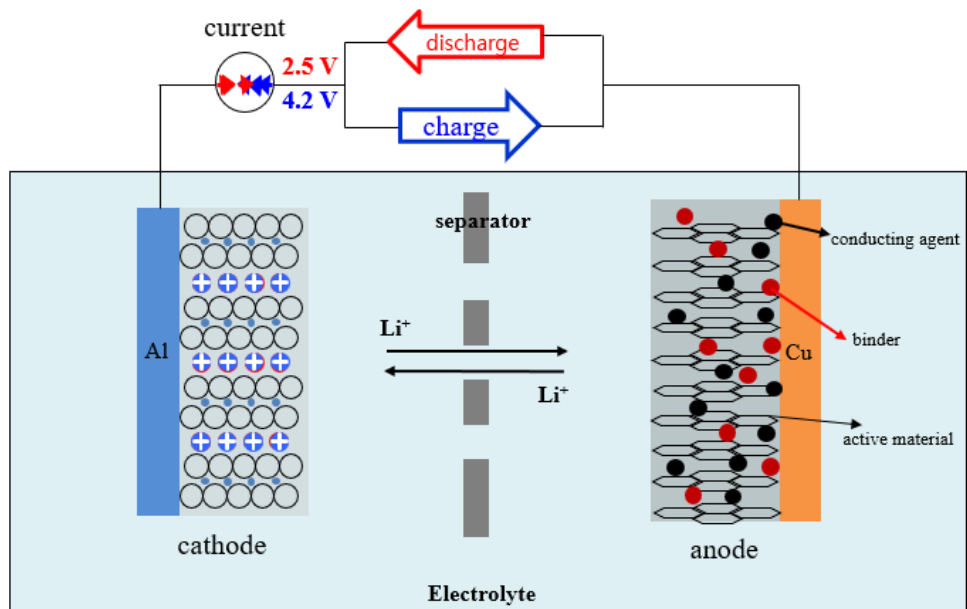


Figure 1: Structure and principle of lithium ion battery.

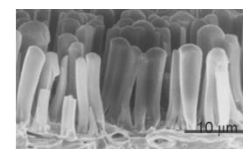
2.2 COMPONENTS OF LITHIUM-ION BATTERIES

2.2.1 Anode

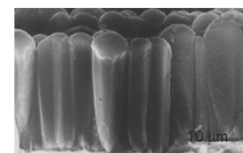
The anode in LIB is working as lithium ions reservoir. It is the place for lithium ions insertion and disinsertion during discharging and charging processes. In a formal anode electrode, there are active materials, conducting agents, binder. And depending on different active materials, the different collectors are chosen for coating. The primary material is active materials, they almost decide how much capacity the battery can carry. The traditional anode active materials are carbonaceous, such as graphite, soft carbon, and hard carbon. Graphite has a good theoretical capacity (372mAh g^{-1}) at low voltage, and with low manufacturing expenses, graphite can also reach a very stable cycling performance. Thus, graphite is one of the most promising active material used on anode for LIB. However, graphite capacity is not that high enough for the large demand of electricity storage these days. So, more potential is discovering to use on LIB anodes, for example, Sn, Pb, Al, Si, Zn, Mn, Tin, lithium titanium oxide (LTO)etc. Among them, Si attracted many researcher's attention by its large specific capacity of 4200mAh g^{-1} . Unfortunately, Si has very serious volume change during cycling (about 310%), shows as table below. So, the capacity fade seriously during charging discharging processes[13]–[15]. Thus, nowadays, many researchers are keep going to find more potential anode materials to make anode electrodes disperse lithium ions better with less volume change and have stable cycling performance with high capacity. Though, active material is the majority, the other additives conducting agent and binder are as important as active materials. It is because that conducting agent can support electron pathways, and binder gives the connections between other additives and collectors. A good anode needs the well incorporation of all the additives so that reach a remarkable battery performance.

□ Active materials for anode

Active material	Capacity (mAh/g)	Density (g/cm ³)	Vol. Change (%)	Binder
C	372	2.25	10	PVDF, SBR
Al	993	2.70	97	
Sn	994	7.29	260	
Si	4200	2.35	310	



Discharged-state of Si



Charged-state of Si

2.2.2 Cathode

Cathode face opposite to anode, it works as the provider of lithium ions. Its composition is same with anode[16], [17]. However, in cathode, the active materials are usually serving by lithium transition metal oxides such as LiNiO₂(LNO), LiCoO₂(LCO), LiMn₂O₄(LMO), and LiFePO₄(LFP), shows as table below. They have good lithium-ion mobility and let lithium ion transfer easier during charging discharging processes. Among them, LCO have been used commonly by its high specific capacity. However, in recent years, LFP draw many researcher's attention by its theoretical specific capacity (170 mAh g⁻¹), thermal safety, environmental compatibility and low cost. Thus, LFP become popular in EV and HEV especially. A good cathode should be no structural changes, stable and insoluble in the electrolyte over the entire operating voltage range, good electronic conductivity, and low synthesis cost. In this study, we are not going to talk about cathode detailly.

Properties	LiCoO ₂	LiNiO ₂	LiMn ₂ O ₄	LiFePO ₄	Sulfur
Redox couple	Co ⁴⁺ /Co ³⁺	Ni ⁴⁺ /Ni ³⁺	Mn ⁴⁺ /Mn ³⁺	Fe ³⁺ /Fe ²⁺	S/S _n ^{x-} /S ²⁻
Voltage (V)	3.6	4	3.9	3.5	2.1
Specific capacity (mAh g ⁻¹) ^a	274	274	148	170	1675
Discharge capacity (mAh g ⁻¹) ^b	145	160	105	155	400
Environment friendliness	Poor	Fair	Good	Good	Good
Availability	Low	Fair	High	High	High
Cost	High	Fair	Low	Low	Very low

^aTheoretical; ^bPractical.

2.2.3 Electrolyte

The electrolyte is one of the essential components of LIBs. It is a medium for lithium ions shuttle back and forth between electrodes which means that lithium-ion conductivity

is a key property of an electrolyte. The electrolyte can be classified as liquid electrolyte and solid electrolyte. In LIB, the liquid electrolyte usually refers to the organic solvent electrolyte are usually consisting of lithium salt (LiPF_6 , LiBF_4 or LiClO_4) in organic solvent mixtures, such as ethylene carbonate (EC), dimethyl carbonate (DMC) and ethyl methyl carbonate (EMC). However, the organic compounds are usually flammable and toxic, so they cannot be used in EV and HEV at large scale. Thus, nowadays, solid electrolyte is studied much popular than decades before. Among the solid electrolyte, polymeric membrane is considered as a promising electrolyte in the future.

Electrolyte can affect LIB performance intensely. It is due to the organic solvents can decompose on the negative electrodes surface at first charge process. The decomposition products are usually complex, and place on the negative electrodes surface around several Å thick which is also known as the solid electrolyte interphase (SEI)[18]. The appropriate SEI layer can prevent the further electrolyte degradation due to its electron isolate but lithium ion conductive. Many research have been done to increase the LIB energy density and safety.

2.3 SUPERCAPACITORS

Different with LIB, supercapacitor is a capacitor with high capacitance, and it is an electrical energy storage system can provide high power densities (10 kW/kg), long cycling stabilities, low maintenance and fast charge/discharge processes (within seconds), shown as Fig. 2. So, they can be applied in the applications such as EV, and HEV braking and power supply system, memory backup for portable electronics and other high current demanding applications[6]–[8]. Supercapacitor can be classified by its energy storage mechanism. Pseudocapacitors use transition metal oxide or conducting polymer as electrodes. During charging and discharging processes, there are electrons which have faradaic transfer with redox reactions so that response a high redox current. To the date, RuO_2 , MnO_2 , Co_3O_4 , NiO and V_2O_5 , etc have attracted many researchers due to their higher specific capacitance and better cycling stability. Among them, MnO_2 is considered as the most potential candidates because of its natural abundance, high theoretical capacitance and low cost. Recently, carbonaceous materials such as carbon nanotubes, graphene, carbon nanofibers and even conducting polymers are studied as well. Comparing with Pseudocapacitors, Electrochemical double-layer capacitors (EDLCs) energy storage mechanism is based on simple adsorption of ions on the Helmholtz double layer at the

interface between the surface of electrolyte and electrode which have high by its large specific surface area (SSA), and EDLCs is the most widely studied supercapacitors[19], [20]. In this study, we work on the EDLCs with symmetric electrodes placed face to face in the coin cell. So, we will not describe Pseudocapacitors detailly.

In charge process, the EDLCs are charged until the voltage gap reaching at the same value with external force. Cations accumulated on the positive electrode whereas anions accumulated on the negative charge. This special layer is called electric double layer which determined the capacitance of an EDLC. During discharge process, the charged EDLC support the electricity to an electric device until all the ions release.

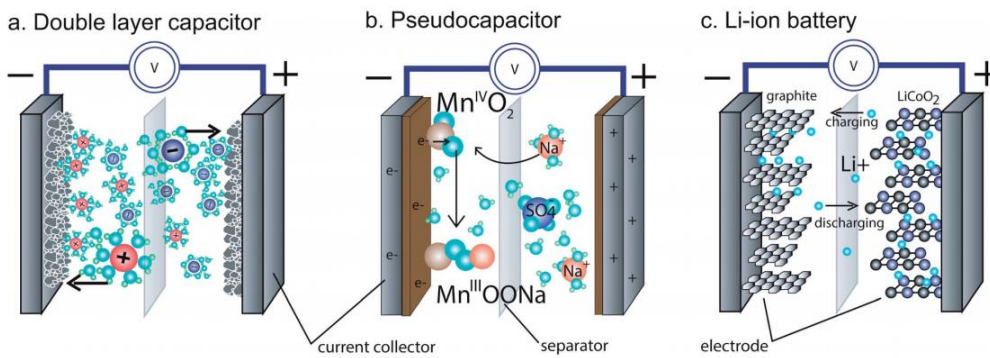


Figure 2: Basic schematics of EDLC, pseudocapacitor and LIB. (a) all carbon EDLC (left), (b) a pseudocapacitor (MnO_2 depicted center) and (c) a lithium ion battery (right). All devices have an active material (e.g., carbon, MnO_2 , $LiCoO_2$), a current collector, a separating membrane

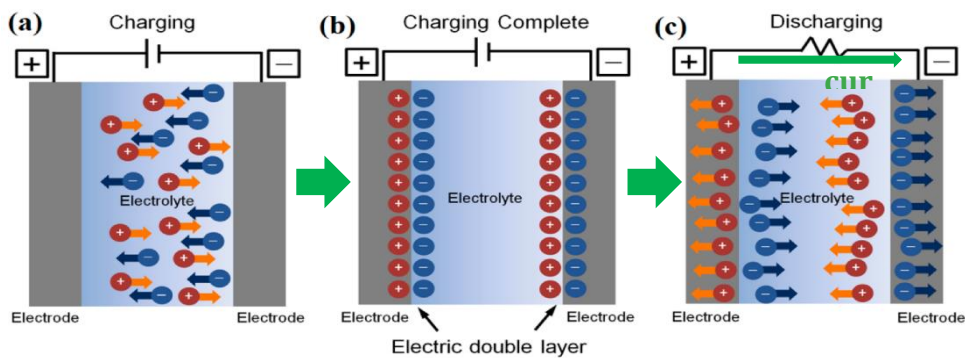


Figure 3: EDLC charge and discharge mechanism.

2.4 COMPONENTS OF EDLCs

2.4.1 Electrode

Traditional EDLCs are composed by two electrodes face to face and separated by a separator. The electrodes are generally consisted by active material, conducting agent and polymeric binder. They are mixed and coated on current collectors. Similarly, with LIB, the primary material in one electrode is active material. Moreover, the active material for EDLCs should be porous structure and having large specific surface area so that more ions can absorb on electrodes surface and lead to a high specific energy density. Porous carbonaceous materials, especially active carbons, are promising electrode materials for EDLCs because of their good stability, good electrical conductivity, relatively low cost and very high specific surface area. There are carbon materials such as carbon nanotubes, carbon aerogels, carbon xerogels, nanotubes, nanofibers, expanded graphite, template carbons, and hierarchical carbon, etc. In recent years, bio-mass derived carbon become popular because of the climate change[21].

As important as active material in electrode, conducting agent and binder are also important for EDLCs electrode[21]–[23]. The conducting agent can support more pathways for electrons, and it is the guarantee of a satisfactory power output of whole EDLCs. The conducting agent is usually referring to conductive carbon black, and it is in a range of 10-20% in one EDLCs electrode. The polymeric binder in EDLCs electrode should be chemical stability over a wide potential range, excellent adhesion to collector and other additives in the electrode, good electron conductivity, good ion conductivity.

2.4.2 Electrolyte

The electrolyte in EDLCs plays a very crucial role in transferring and balancing charge between the two electrodes. It directly influences the interaction surface between the electrolyte and electrodes and internal structure of active material. The electrolyte of EDLCs can be sort into two types by its phase[24]. The liquid electrolyte, which is considered as the traditional electrolyte for EDLCs, and liquid electrolyte can also dive to aqueous electrolyte with low operating voltage while organic electrolyte with higher operating voltage. Thus, an appropriate electrolyte for EDLCs should be suitable viscosity, high ion conductivity, wide operating voltage window, expanded applicable temperature range and safe. Another electrolyte is solid state electrolyte which is

considered as a safer and much flexible electrolyte. This may be applied on wearable devices.

2.5 ROLE OF POLYMERIC BINDER IN ELECTRODES OF LIB AND EDLCs

The crucial rule of design a LIB is to make as much active material as possible within a limited volume so that the battery can have higher capacity and higher energy density. So, the other additives should be reduced as much as possible. Even though, the little amount of conducting agent and binder make big difference. The little amount of conducting agent support a large power output at high current. Moreover, the little amount of binder should adhere other additives together with collector, shown as Fig. 4.

A good binder for operating a LIB well, there are other requires as well. First of all, the binder should have good electrochemical stability over the wide operating voltage. Therefore, there is a prediction method for choosing binder for LIB. The calculated Highest Occupied Molecular Orbital (HOMO) and Lowest Unoccupied Molecular Orbital (LUMO) of various polymers are as shown in Fig. 5 [25]. It is considered that HOMO related to oxidation potential and the LUMO related reduction potential. So, the polyvinylidene fluoride (PVdF), and styrene-butadiene rubber (SBR) are used for anode binders while considering binder solubility and other appropriate properties, the mechanism of binder safety operating voltage is shown as Fig. 6. Furthermore, binder should hold low swelling rate in electrolyte which can keep a well contact of active materials and conducting agent to the collector, and lead to a good LIB cycle performance. Moreover, If the binder has good electron conductivity and lithium-ion conductivity, the battery performance would be further improved, like higher capacity, higher energy density and power density. There are other properties to estimate a binder when the manufacturing processes have been considered, such as the suitable solubility in solvent and a low heat of vaporization to remain a constant slurry viscosity over manufacturing periods. An appropriate elastic property and mechanical properties are also necessary. This is because that a rubbery state of binder will expand again after pressed electrode, and too-rigid electrode will crack upon prolonged cycling. At present, there is none of polymer can reach all the properties talked above, so sometimes, for getting a better battery performance, the combination of binder is needed.

The binder works in EDLCs is similar with in LIB. It should be noticed that, the active material load in EDLCs is larger than LIB, so the binder in EDLCs electrodes should have better mechanical properties.

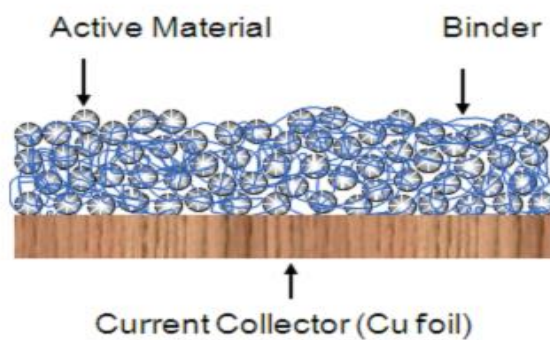


Figure 4: Typical anode of LIB.

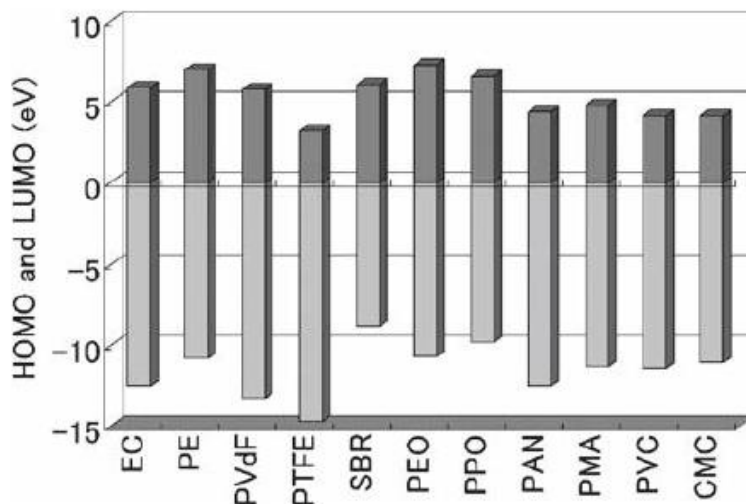


Figure 5: Calculated redox windows of various polymers.

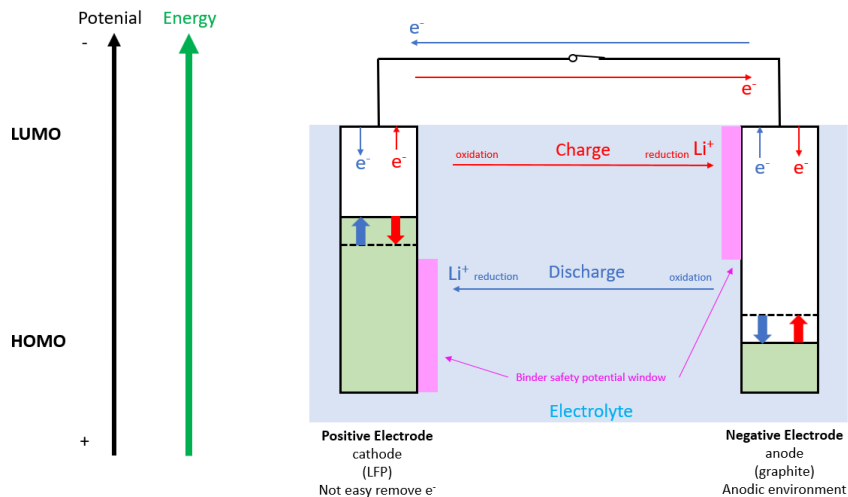


Figure 6: Mechanism of binder safety operating voltage.

2.6 CLASSIFICATION OF POLYMERIC BINDERS

2.6.1 Organic solvent-based binder

The polymeric binder used for LIB and EDLCs can be classified into two kinds by its solvents. The traditional organic solvent-based binder Polyvinylidene fluoride, or polyvinylidene difluoride (PVdF) is the most widely studied for anodes and cathodes in LIB, because it is chemically inert over the potential range used, does not react with the electrolyte or lithium and offers the possibility of high voltage operation[26], [27]. The monomer of PVdF has two hydrogen atoms and two fluorine atoms ($-\text{CH}_2-\text{CF}_2-$). After polymerization, the monomer of PVdF lines up by dipole-dipole interaction as $[-\text{CH}_2-\text{CF}_2-]_n$. Such bond connection decided the crystalline characters of PVdF, and it is sort of linear binder when applied in LIB, as shown Fig. 7. The PVdF warp up active material by fiber-like surface contact. However, in order to homogeneously mix the additives of electrode, the PVdF must dissolved into organic solvent, such as NMP (n-methyl-2-pyrrolidone) which is considered as s high cost, difficulty in recovery and chemical toxicity. Furthermore, NMP has a low evaporation rate because of its higher boiling point of 196°C , so the preparation organic-based electrode slurry will take a longer time and higher temperature to dry. Moreover, the LIB using PVdF as binder has

moderate rate of charge/discharge and high irreversible capacity by SEI layer. Besides, our society is facing serious climate changing, and PVdF is kind of fluorine-containing chemical which is highly related to “global warming”. Therefore, searching for a “green” binder for energy storage system is imperative.

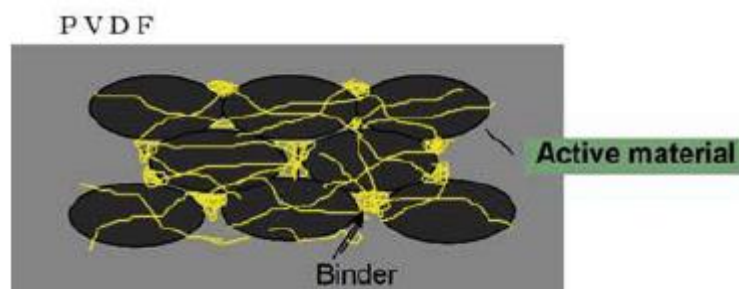


Figure 7: Conceptual illustration of binding between PVdF and active material.

2.6.2 Water-based binder

Instead of using organic-based binder, the water-based binder has promising potential for energy storage system. It is environmentally friendly, low cost, easy dried during electrodes manufacture[21]. Poly(tetrafluoroethylene) (PTFE) is known as a common water-based binder since it is highly hydrophobic with strong C–C and C–F bonds providing high chemical and mechanical stability. However, it is still fluorine-containing chemical which is not eco-friendly enough. In order to make water-based binder “fluorine-free”, there are many kinds of polymer have been investigated for using as binder for energy storage system, such as aliphatic, aromatic polymer, and acrylate type copolymer (ACM), due to the low glass transfer temperature they have, and they can be produced in large scale with low cost. For instance, polyvinyl pyrrolidone (PVP), styrene-butadiene rubber (SBR) and polyacrylonitrile (PAN). Thus, they can afford a good mechanical stability and then enhance the cycle performance for energy storage system. Nevertheless, they cannot be renewable. Consequently, researchers have changed their attraction to bio-class of binders which is also called polysaccharides. It is very common flavor in food, such as carboxymethyl cellulose (CMC), alginate, pectine, starch, gelatin, etc. Among them CMC is the most popular bio-derived compound in the current production of LIB and EDLCs. However, it cannot support a large loading of active

material, so the combination of other binder with CMC is another approach for electrodes manufacture. For example, SBR combined with CMC as binder for LIB has shown better performance than each of them plays as sole binder. It is due to the high flexibility, good adhesion strength, and electrochemical stability of SBR, and the good solubility of CMC making electrodes slurry mixed homogenously.

2.7 WATER-BASED CONDUCTIVE BINDER FOR LIB ANODE AND EDLCs

In this study, we choose poly (acrylonitrile/butyl acrylate) water-based binder which introduced in our previous work. It is an ACM type binder, the high polar poly acrylonitrile (PAN) can afford a good electrochemical stability and a good lithium ion conductivity[28], [29], meanwhile poly butyl acrylate (PBA) can support a good mechanical property by its low glass transition temperature ($T_g=-45$ °C). So, the copolymer, poly(acrylonitrile-butylacrylate) (PANBA) is considered as a competitive polymer as SBR while applied as binder for LIB, since it has good adhesion strength, stable electrical and electrochemical properties and good mechanical characteristic[11], [30]. However, it is not electronic conductive enough for improve the power density of energy storage system.

Adding a conductive filler into a polymer matrix is a normal way to increase polymer conductivity, and these kinds of polymer composites are called conductive polymer composites (CPC)[31]. The conductive polymer composites can be classified by their fillers dimensionality. And their conductivity can be explained and fitted by percolation theory[32]. In this study, we introduced two fillers. One is 0D polypyrrole, and the other is 2D conductive material MXene. They have been combined with PANBA and hollow core-shell structure polymer, and applied on EDLCs and LIB.

Typical electrically conducting polymers (ECPs), such as polyaniline (PANi), polypyrrole (PPy), polyacetylene, and polythiophene (PT), have conjugated bonds so that delocalized pi electrons can move freely through the polymeric chain. Of these, PANi and PTs have often been applied to LIBs as the binder of electrodes[33]–[35]. Unfortunately, conducting polymers usually have low adhesion and do not maintain the mechanical integrity of the electrodes after long-term cycling. Therefore, conducting polymers are normally used in conjunction with highly adhesive polymers, such as carboxymethyl chitosan and polyacrylic acid, when applied to a binder. PPy is air stable and easy to prepare by either chemical or electrochemical methods and shows very good electrical

properties when used in electrochemical applications. Consequently, in this study, PPy was introduced to the conductive component of the water dispersed PANBA binder. The PANBA-PPy binder system was applied to LTO electrodes as an eco-friendly conductive water-dispersed binder, which is the first report of such use. A variety of physical and electrochemical characterization techniques were employed to examine how the conductive PPy component in a binder affects the electrochemical performance of LTO electrodes. The graphic abstract is shown in Fig. 8 The same composition but different polymerization sequenced PPy-PANBA had also investigated and used as EDLCs electrodes.

For further increasing electronic conductivity of water-based binder, 2D material is a good candidate such as graphene, graphene oxide, transition-metal dichalcogenides, metal-organic frameworks (MOFs) and MXene. because they are extremely electrically conductive, thermal conductive and strong mechanical strength with large aspect ratio. MXenes are 2D titanium-based carbides discovered by Gogotsi in 2011, and they are known for their high conductivity and hydrophilic nature[36], [37]. Moreover, with MXene reactive surface, it may offer a prospective platform for synthesis MXene/polymer composites[38]. In 2016, Faisal Shahzad et al. demonstrate the MXene sodium alginate composites used for high electromagnetic interference shielding effectiveness with good mechanical flexibility[39]. In 2018, Jianjian Fu et al. applied MXene with polyaniline to form graphene encapsulated MXene Ti₂CTx@polyaniline composite for asymmetric supercapacitor and show remarkable performance which may suggest that potentials of MXene as promising materials for energy storage devices[40]. In this work, we introduced MXenes/poly acrylonitrile/butyl acrylate composites by in-situ polymerization and apply as environment-friendly water-based binder for symmetric EDLCs. The graphic abstract is shown in Fig. 9.

Moreover, we also investigated the hollow core-shell shaped copolymer composite with MXene work as conductive binder for EDLCs electrodes. The hollow core-shell shaped copolymer is comprised by poly styrene, poly acrylonitrile and poly butyl acrylate which is similar with PANBA. Since the specialist structure of the copolymer, the electrolyte can pass through the copolymer shell easily so that a well electronic and ionic conductive binder can be formatted by the introducing of MXene. A series of property tests were conducted.

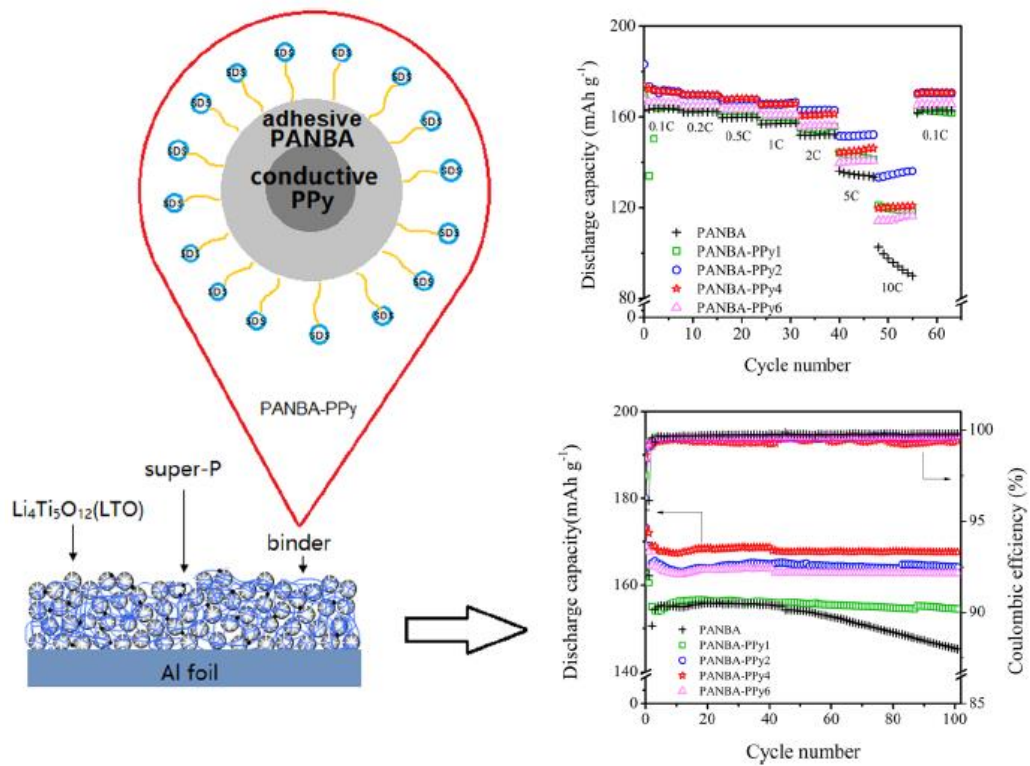


Figure 8: The graphic abstract of PANBA-PPy binder applied on LTO electrode for LIB anode.

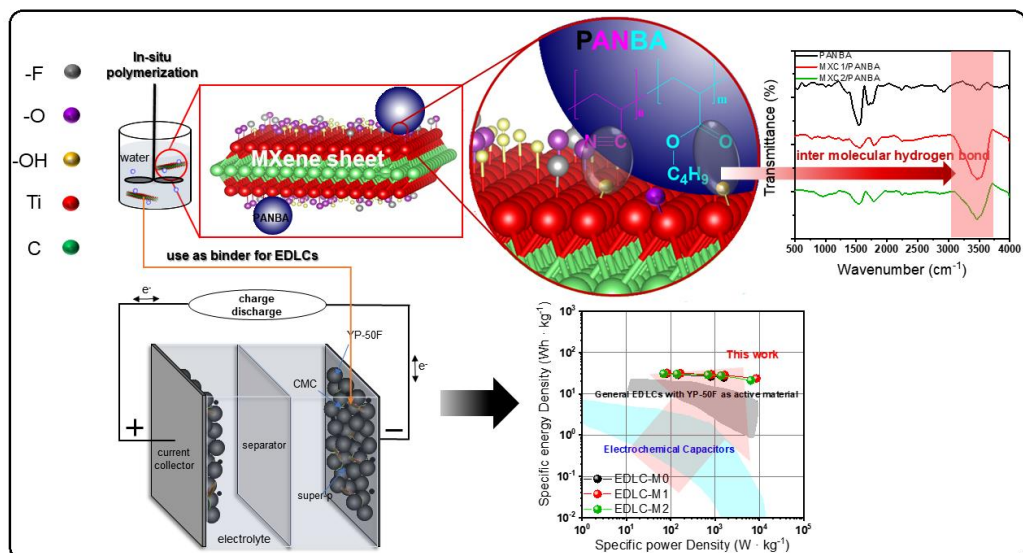


Figure 9: The graphic abstract of MX/PANBA binder applied on EDLCs electrodes.

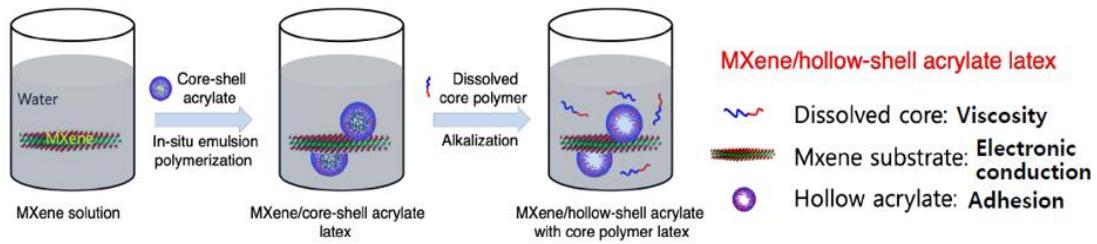


Figure 10: The graphic abstract of MX/Hollow core shell binder.

2.8 IN-SITU EMULSION POLYMERIZATION

There are three basic method to synthesis CPC, melting blending, solution blending and in-situ emulsion polymerization[41]. The in-situ emulsion polymerization has developed into a widely used process for the production of synthetic latexes, since it can disperse the filler well and lead a good conductivity network of polymer, and it is suitable for the material that is not stable with heat[42]. Moreover, the shear force during the polymerization can afford the power for some bond's formation, such as hydrogen bond or some covalent bond.

The definition for in-situ is synthesis the polymer on the filler surface or around filler, it is sort of residence of polymer, and the emulsion phase is consisted of colloids which dispersed in solution stably while the present of emulsifier or surfactants. The emulsion polymerization is conducted in a well filler dispersed medium (usually water) with other ingredients, for instance, monomers, surfactants and initiators. The latex is formed by a free-radical-initiated chain polymerization in which a monomer or a mixture of monomers in the presence of a surfactant. The use of emulsion polymerization process has several distinct advantages such as the physical state of the emulsion (colloidal) system makes it easy to control the process, thermal and viscosity problems are much less significant than in bulk polymerization, the product of an emulsion polymerization can in many instances be used directly without further separations and so on.

According to the Smith-Ewart description (Fig. 11) of emulsion polymerization mechanism, there are 3 stage of polymerization[43]. First of all, the monomers exist in surfactant micelles ($\approx 2.5\%$), dissolved in water ($\approx 2.5\%$) and monomer droplet that surrounded by surfactant ($\approx 95\%$) when the concentration of a surfactant exceeds its critical micelle concentration (CMC). The first monomer molecules was first polymerized

while they met the waterborne free radicals dissolved in the continuous aqueous phase, the oligomers chain length keep growing until they are hydrophobic enough to enter into the monomer-swollen micelles, and then continue to propagate by reacting with the monomers therein. As a consequence, the premier particle nuclei formed. In order to keep the colloidal stable, the empty micelles will disband and afford the surfactant to other monomer-needed micelles. The first stage of particle nucleation ends after all the micelles exhausted. Next, as the particles grow in micelles, the large monomer storage monomer droplet keep supply the monomers for them until about 60% monomer converted. This particle growth stage ends when monomer droplets disappear in the system. The last stage is completed while all the monomer converted, and the converting rate will decrease until polymerization stop. What needs to be noticed is that in the first particle nuclei formation, the reason of a free radical reacted oligomer will enter into a micelle rather than monomer droplet is that the total surface area of the micelles is much greater than the total surface area of the fewer, larger monomer droplets. Monomer in the micelle quickly polymerizes and the growing chain terminates.

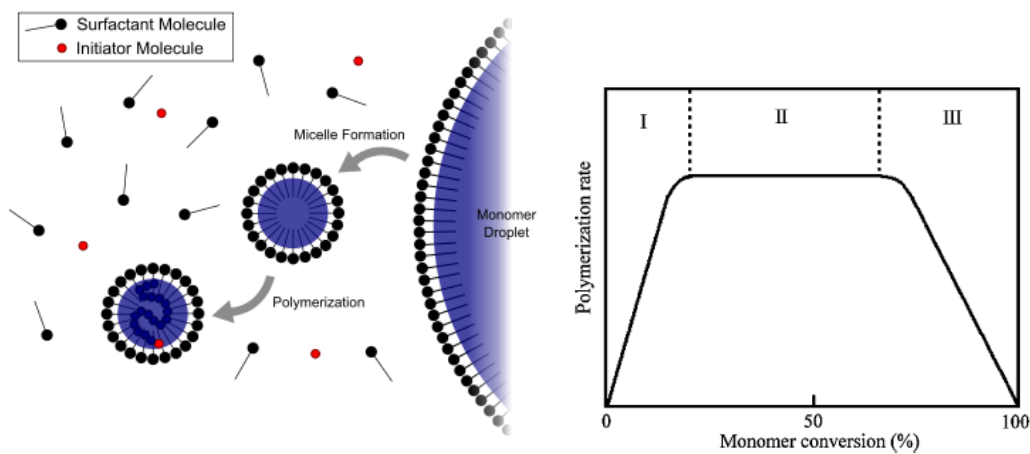


Figure 11: Schematic diagram of emulsion polymerization mechanism. (left) and typical rate (right) of emulsion polymerization.

CHAPTER 3: EXPERIMENTAL

3.1 SYNTHESIS OF POLY (ACRYLONITRILE/BUTYL ACRYLATE)-POLYPYRROLE BY IN-SITU EMULSION POLYMERIZATION.

PANBA was first synthesized using the emulsion polymerization method described elsewhere. To prepare for PPy polymerization, a small amount of sodium dodecyl sulfate (SDS, Tokyo Chemical Industry Co.) was then added to 115g of PANBA emulsion containing 30 g PANBA with pyrrole (Alfa Aesar) monomer ranging in weight from 1 to 6g. Finally, a certain amount of potassium persulfate (KPS, Sigma-Aldrich) corresponding to one part of the pyrrole monomer was introduced to initiate the polymerization of pyrrole. The reaction was carried out at a constant temperature of 70 °C for 2 h before being cooled to room temperature. For convenience, the PANBA-PPy binders are referred to as follows: PANBA-PPy1, PANBA-PPy2, PANBA-PPy4, and PANBA-PPy6, where the number indicates the mass of PPy (in grams) in the binder. The results were compared with PANBA origin binder.

3.2 SYNTHESIS OF POLYPYRROLE-POLY (ACRYLONITRILE-BUTYL ACRYLATE) BY IN-SITU EMULSION POLYMERIZATION.

Polypyrrole (PPy) was synthesized firstly by emulsion polymerization. The reaction happened in a double-wall reactor connected with a reflux condenser. A certain amount of sodium dodecyl sulfate (SDS, Tokyo Chemical Industry Co.) was added into distilled deionized (DDI) water. Next, 1 wt% of pyrrole monomer (Alfa Aesar) based on ANBA monomer was added. The polymerization was initiated by adding potassium persulfate (KPS, Sigma-Aldrich) when the temperature up to 70 °C. The reaction kept for 2 h before starting synthesizing PANBA which method was studied in our previous work. The product was cooling down to room temperature before testing.

3.3 SYNTHESIS OF MXENE/POLY(ACRYLONITRILE-BUTYL ACRYLATE) BY IN-SITU EMULSION POLYMERIZATION.

Two types of MXenes clay (Ti_2CT_x and $Ti_3C_2T_x$) were purchased from Advanced Material Esoterica (China). A small amount of MXene was dispersed in distilled deionized (DDI) water and sonicated in an ice bath for 4 h. The weight percentage of MXene to total weight of acrylonitrile/butylacrylate (AN/BA) monomer was 1 %. The

dispersed MXene solution filled a double-wall reactor connected with a reflux condenser. Certain amounts of sodium dodecyl sulfate (Tokyo Chemical Industry Co.), AN/BA monomers, and potassium persulfate (Sigma-Aldrich) were subsequently added to the reactor in order to prepare emulsion polymerization. The in-situ emulsion polymerization of poly(acrylonitrile-butylacrylate) (PANBA) in the dispersed MXene solution was performed at 70 °C under nitrogen atmosphere. More details on the polymerization are available in our previous work. The products $Ti_2CT_x/PANBA$ and $Ti_3C_2T_x/PANBA$ are called MX1/PANBA and MX2/PANBA, respectively.

For comparing the difference between in-situ polymerization and physical mixing, the same amount of MXene as MXs/PANBA was simply mixed with the PANBA and noted as MX1+PANBA and MX2+PANBA, respectively.

3.4 SYNTHESIS OF MXENE/ CORE SHELL STRUCTURED POLY(STYRENE-ACRYLONITRILE-BUTYL ACRYLATE) BY IN-SITU EMULSION POLYMERIZATION.

The seed and core emulsion polymerization was conducted according to the recipe as Table 1 in a four-neck double jacket flask reactor. Before the shell polymerization happened, a small amount of MXene (Ti_2CT_x and $Ti_3C_2T_x$) was dispersed in distilled deionized (DDI) water and sonicated in an ice bath for 4 h. The weight percentage of MXene to total weight of shell styrene/acrylonitrile/butylacrylate (St/AN/BA) monomer was 1 %. The shell polymerization was carried out at the present of MXene dispersed solution, and the other ingredients are added as the recipe Table 1. The whole polymerization was kept for 6 h (2 h for each step) with 200 rpm stirring at 80 °C, 80 °C and 70 °C, respectively. The monomer and initiator were feed continuously at the same time.

3.5 SYNTHESIS OF MXENE/ HOLLOW CORE SHELL STRUCTURED POLY(STYRENE-ACRYLONITRILE-BUTYL ACRYLATE) BY IN-SITU EMULSION POLYMERIZATION.

For remove the core, the alkalization treatment was conducted by mixing the core-shell latex with 15 wt% NaOH at 80 °C for 3h, the solution was stirred by heating-magnetic stirrer 1000 rpm.

Components	Seed (g)	Core (g)	Shell (g)	Alkalization (g)
Methyl methacrylate(MMA)	5.5	23	-	-
Methacrylic acid(MAA)	0.56	10	-	-
Butyl acrylate(BA)	6.5	-	60	-
Styrene(St)	-	-	30	-
Acrylonitrile(AN)	-	-	10	-
Divinylbenzene(DVB)	-	-	1	-
Ammonium persulfate(APS)	1.0	0.562	0.8	-
Sodium dodecyl Benzene Sulfonate(SDBS)	0.06	0.009	0.2	0.1
Seed	-	50	-	-
Core	-	-	130	-
Shell	-	-	-	30
Distilled water	500.0	250	55	20
15 wt% NaOH sol.	-	-	-	5
Temperature/°C	80	80	70	80

Table 1: Recipe of the hollow core shell polymer.

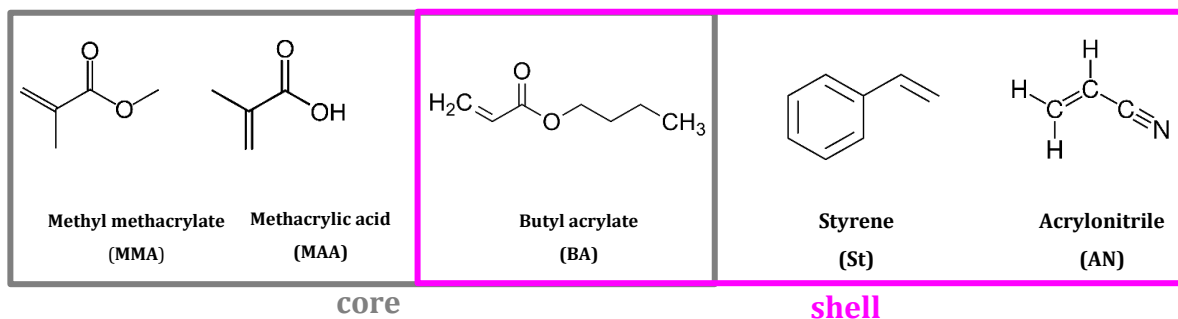


Figure 12: Chemical structures of hollow core shell polymer.

3.6 ELECTRODE PREPARATION AND CELL ASSEMBLY

3.6.1 Lithium titanium oxide (LTO) anode electrode

LTO electrodes were prepared with 90 wt% LTO active material, 5 wt% conductive super-P, 2 wt% high-viscosity CMC (Daicel FineChem Ltd., Japan), and 3 wt% binders based on the solid contents. All the materials were mixed using a homogenizer (Nissei ACE AM-2, Japan) for 45 min. For comparison, PANBA was also used as a binder for the LTO electrode. The mixed slurry was casted onto a 20- μm -thick Al foil. After drying in a convection oven at 60 °C for 30 min, the electrodes were roll pressed and placed in a vacuum oven maintained at 70 °C for 1 day before being assembled into CR2032-type coin-half cells in an argon-filled glove box.

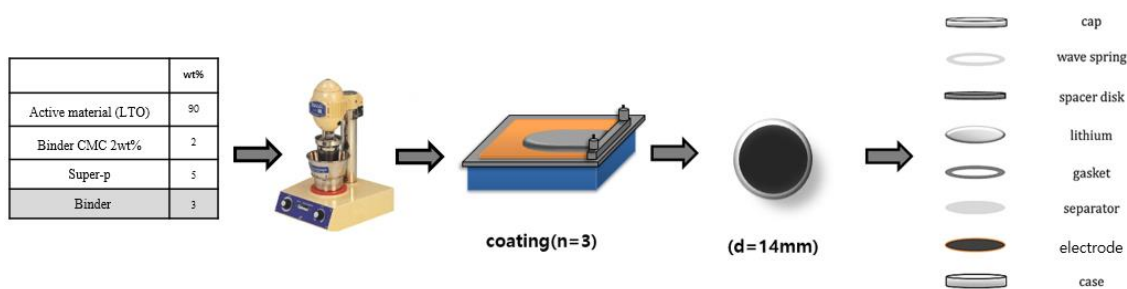


Figure 13: The process of LTO electrode preparation and cell assembly.

3.6.2 EDLCs electrode

Electrodes were prepared with activated carbon (YP-50F, Kuraray Chemical Co., Ltd., Japan), conducting agent Super-P (SP), carboxymethyl cellulose (CMC, Daicel FineChem Ltd, Japan), styrene butadiene rubber (Nippon Zeon BM-400B), and polymeric binder, and their composition (91.5/1.5/4.5/2.5 YP-50F/CMC/polymeric binder /SP) is close to commercial EDLC electrodes. In addition, a moderate amount of DDI water was used for adjusting the slurry viscosity. The electrode slurry was well mixed with a moderate amount of distilled de-ionized (DDI) water and coated onto etching aluminium foil. The electrodes were then dried in a convection oven at 60 °C for 30 min. The loading of electrode was $4.7 \pm 0.5 \text{ mg cm}^{-2}$ with the thickness of 100 μm to 115 μm .

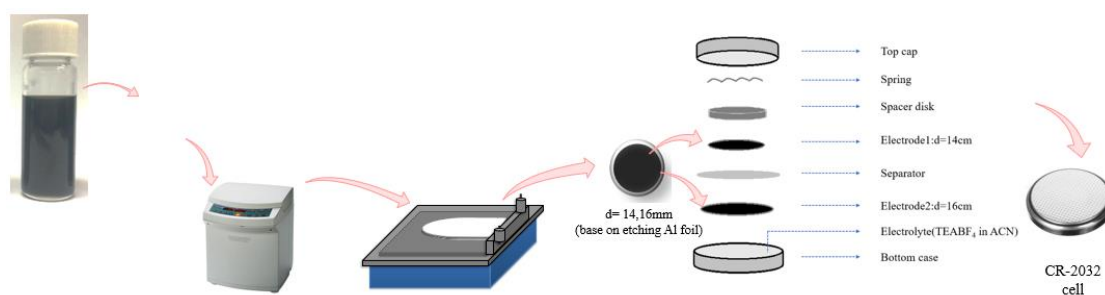


Figure 14: The process of EDLCs electrode preparation and cell assembly.

3.6.3 Cell assembly

The LTO electrodes after totally dried in vacuum oven were then cut into $d=14\text{mm}$ circuit shape, the electrodes weightiness and thickness were measured. 1 M LiPF₆ in 1:1:1 ethylene carbonate (EC): dimethyl carbonate (DMC): ethyl methyl carbonate (EMC) by volume (Panaxetec Co., Korea) was used as an electrolyte to produce the CR2032 type coin-half cells in an argon-filled glove box. Lithium metal was used as a counter electrode. Additionally, cells were fabricated with a working electrode composed of only a binder film coated on Cu-foil and the electrochemical properties were also characterized.

The EDLCs electrodes weightiness and thickness were measured after dried in vacuum oven and cut into $d=14\text{mm}$ and 16mm circuit shape to make sure the active area is equal to the area of $d=14\text{mm}$ circle. The two electrodes were placed face to face as shown in

Fig. 2 and all the parts were assembled to the symmetrical CR2032 type coin cells in an argon-filled glove box. Polypropylene film was used as a separator and 1 M tetraethylammonium tetrafluoroborate (TEABF₄) in acetonitrile (AcN) was used as electrolyte.

3.7 BINDER CHARACTERIZATION

3.7.1 Sheet resistance analysis

The electrical resistance of binder films was measured using a 4-point probe (CMT-100MP, Advanced Instrument Technology). Thin polymer coating on Al foil was dried in a convection oven at 60 °C overnight, and then cut to 14-mm diameter circle. Their sheet resistances were measured 10 times for each sample, and the average number was recorded.

3.7.2 Fourier-transform infrared analysis (FTIR)

The polymers function groups were characterized by Fourier-transform infrared (FT-IR, Thermo Scientific Nicolet iS5) spectroscopy over the wavenumber range, 500–3900 cm⁻¹.

3.7.3 Raman analysis

The Raman spectroscopy was conducted using (DXR Raman Microscope, Thermo Fisher Scientific), under $\lambda_{exc} = 532$ nm laser excitation.

3.7.4 Transmission electron microscopy (TEM)

The Transmission electron microscopy (TEM, JEM-2100F, JEOL, Japan) was used to examine the morphology of the polymer.

3.7.5 Scanning electron microscope analysis (SEM)

The binder morphology was examined by field emission scanning electron microscope (FE-SEM, JSM-600F, JEOL, Japan) at an acceleration voltage of 15 kV and 5 kV.

3.7.6 Thermogravimetric analysis

The thermal stability was investigated by Thermogravimetric analysis (TGA) with a nitrogen atmosphere and 10 °C/min heating, carried out by TA Instruments Q50. The synthesized polymers were dried at 60 °C overnight. The cut polymer film heated up from 30 °C to 750 °C. A platinum pan was used to hold the sample.

3.7.7 Differential Scanning Calorimetry

Differential scanning calorimetry (DSC, TA Instruments Q50) with a nitrogen atmosphere and 10 °C/min heating/cooling was used to determine the glass transition temperature (T_g) of the polymers. The observation range is from -50 °C to 150 °C. Sample was put in an aluminum pan (Tzero Hermetic aluminum pan) and hermetic sealed.

3.7.8 Zeta potential analysis

The zeta potential of polymer solution was measured by ZEN3600, Zetasizer Nano ZS, Malvern Instruments Ltd.

3.7.9 Contact angle

The polymeric binder was coated on an Al-foil and dried in a convection oven at 60 °C overnight. A square thin sample was cut and attached on a glass substrate by a double-sided tape to avoid any displacement then placed on the sample stage. The binder film contact angle in the duration of 60s was measured by an optical tensiometer (Theta Lite, Biolin Scientific) exposing to a fixed volume of electrolyte droplet (1:1:1 EC: DMC:EMC by volume) for LTO electrode, and 1 M TEABF₄ in ACN for EDLCs electrode.

3.7.10 Electrolyte uptake

The polymer films coated on Cu foil were also fully soaked in the electrolyte solution (1:1:1 EC: DMC: EMC by volume) at room temperature for 24 h in order to examine their chemical stability. After that, the samples were dried by blotting and immediately weighed. The change in weight before and after the soaking was the amount of solvent absorbed used to calculate the electrolyte uptake of the binder.

3.8 ELECTRODE CHARACTERIZATION

3.8.1 Adhesion strength

The adhesion strength of the electrodes with respect to etching-Al foil were measured by 2-cm-wide electrode strips in the peeling mood on a texture analyzer (TA-Plus, Lloyd Instruments Ltd.) at a propagation speed of 60 mm min⁻¹.

3.8.2 Brunauer Emmett-Teller (BET) analysis

The surface area and pore volume of electrodes were measured by Brunauer Emmett-Teller (BET) with N₂ adsorption/desorption using on porosity analyzer (Micromeritics

ASAP 2020). Degassing treatment of the electrode excluding etching Al foil was hold at 300 °C for 20 h before analyzing. The Barrett-Joyner-Halenda (BJH), and t-plot methods were used to analyze the information on the pores of the electrode.

3.9 ELECTROCHEMICAL PROPERTIES

The EIS of cells was examined with a frequency range of 10^5 Hz to 10^{-2} Hz at open voltage and 10^6 Hz to 10^{-2} Hz at $E = 0$ V for LIB and EDLCs, respectively. The EDLCs Cyclic voltammetry (CV) tests were also carried out in the same VSP electrochemical station at various voltage scan rates 5, 20, 50, 100 $\text{mV} \cdot \text{s}^{-1}$ in the voltage of 1 V to 2.6 V and 0 V to 3 V for LIB and EDLCs, respectively. Galvanostatic charge/discharge performance and rate capability tests for LIB were performed in a battery cycler (WBCS3000, Wonatech, Korea for LIB). at 0.1 C for the first two cycles and at 1 C for the subsequent 100 cycles. Rate capability tests of the cells were also performed in a variety of charge/discharge currents ranging from 0.1 to 10 C. Galvanostatic charge/discharge performance and rate capability tests for EDLCs were conducted in a battery cycler (PNE solution Co., Korea for EDLCs) through constant current and constant voltage mode in the range of 0.1 V to 2.7 V at 1.54 mA for the first 5 charge/discharge cycles and in the range of 1.35 V to 2.7 V at 4 mA for the subsequent 10,000 cycles. A variety of charge/discharge currents: 0.5, 1.0, 5.0, 10.0, 50.0 $\text{mA} \cdot \text{cm}^{-2}$ were selected for rate capability test at room temperature as well.

CHAPTER 4: RESULTS AND DISCUSSION

4.1 POLY (ACRYLONITRILE-BUTYL ACRYLATE)-POLYPYRROLE

4.1.1 Physical properties

4.1.1.1 Stability and TEM

A water-dispersed emulsion is normally stored at most for 6 months before being applied to LIBs as a polymer binder. Therefore, the emulsion stability must be checked. In this study, the stability of the PANBA-PPy emulsion was examined using a Turbiscan aging station (Turbiscan LAB, Formulaction Co., France) by scanning the samples at 30 °C for 24 h. The Turbiscan analysis technique describes the sample destabilization, such as creaming, sedimentation, flocculation, aggregation, and coalescence, according to the backscattering and transmission signals, and represents the destabilization as a value of the Turbiscan Stability Index (TSI). Higher TSI values mean that more destabilization occurred in the sample. Figure 1a presents the TSI of the PANBA-PPy emulsion samples over a 24 h period. The PANBA-PPy6 emulsion containing a relatively large amount of PPy (6 g) showed a much higher TSI compared to the other samples. This explains why a sample exceeding 6 g PPy could be synthesized, despite the potential increase in electrical conductivity with increasing PPy content. In addition to TSI, the morphology of the PANBA-PPy2 sample, as an example, was observed by TEM, as shown in Fig. 15 b. The sample was coated on a copper grid and dried before being characterized. Owing to the two-step emulsion polymerization, an approximately 10-nm-thick thin outer shell, probably corresponding to PPy, encompasses the inner PANBA core. This morphology is similar to that of the PPy/poly(styrene sulfonate) composite reported elsewhere[44]. Although a few particles aggregated, as shown in the figure, the PANBA-PPy2 sample was much more stable than the PPy sample.

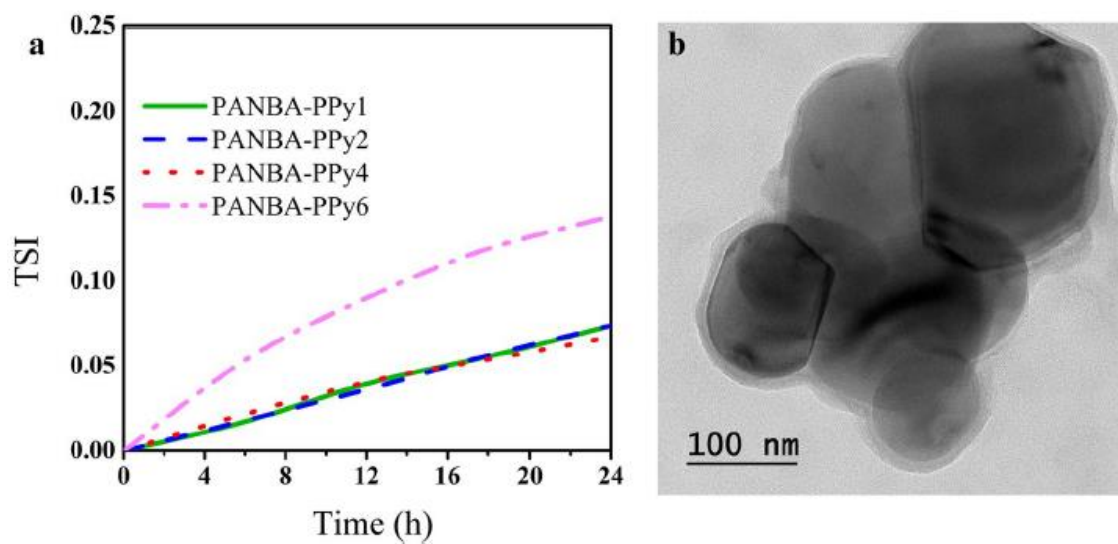


Figure 15: Stability and TEM.

(a) Turbiscan stability index of the PANBA-PPy samples measured over a 24 h period.

(b) High-resolution TEM image of the PANBA-PPy2 sample.

4.1.1.2 FTIR

In addition to the TEM result, the FT-IR spectra of PPy, PANBA, and PANBA-PPy2 binder films in Fig. 16 indicate a successful copolymerization of PPy to PANBA. The spectrum of PANBA-PPy2 reveals the characteristic peaks at 1545 cm^{-1} (C=N), 1731 cm^{-1} (C=O), and 2241 cm^{-1} (C \equiv N) which are attributed to the fundamental vibrations of PPy ring, the stretching vibration of carbonyl in butyl acrylate, and the stretching vibration of nitrile groups in acrylonitrile, respectively [45]–[47].

4.1.1.3 Sheet resistance

As mentioned previously, the main objective to incorporate PPy in PANBA is to improve the electrical conductivity of the binder system, ultimately leading to significant improvements in the electrochemical performance of the LTO electrodes. The improvement in the electrical conductivity of the PANBAs copolymerized with different amounts of PPy is highlighted by the sheet resistance of the thin PANBA-PPy films, which are listed in Table 2. As expected, the presence of PPy in the copolymer reduced the sheet resistance of the PANBA to a measurable value from out of the range of the 4-point probe station, and an increase in the PPy content decreased the sheet resistance significantly. This produced a better electron transfer pathway in the LTO electrode.

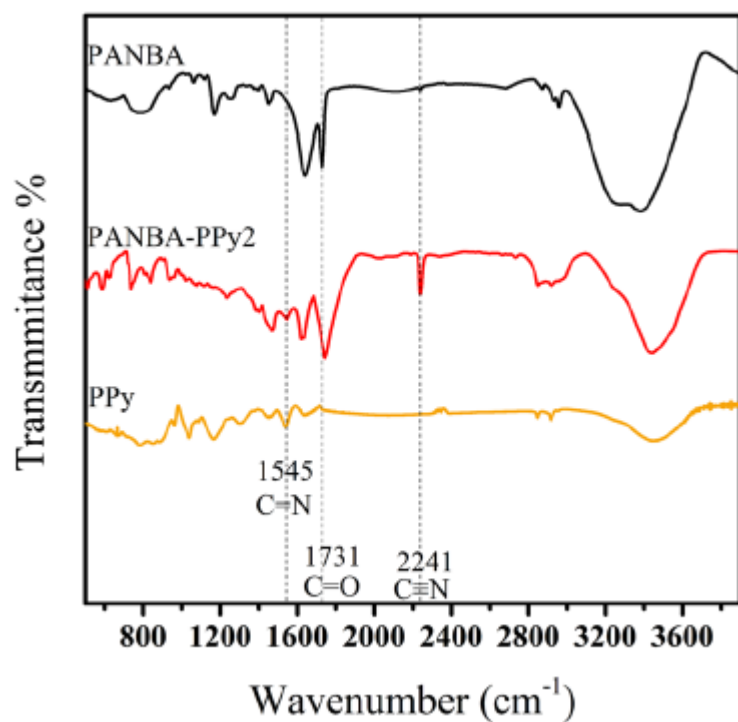


Figure 16: FT-IR spectra of PPy, PANBA, and PANBA-PPy2 binder films.

	PANBA-PPy1	PANBA-PPy2	PANBA-PPy4	PANBA-PPy6	PANBA
R(Sq-1)	133.8	114.7	91.3	72.3	Out of range

Table 2: Sheet resistance of the PANBA-PPy samples containing different amounts of polypyrrole.

4.1.1.4 TGA

Electrodes are generally exposed to temperatures higher than 100 °C during the drying process and to extremely high temperatures under thermal runaway initiated for several reasons, such as overcharge, solid electrolyte interface breakdown, and undesirable electrolyte reactions with lithium ions. In such harsh situations, decomposition of the polymer binder at low temperatures worsens the situation, making it uncontrollable. Unfortunately, the synthesized PPy begins to decompose at relatively low temperatures (< 200°C) compared to typical polymers, as shown in Fig. 17. This is one of the reasons why the sole use of PPy is not applicable to the binder of LIBs, regardless of its low adhesion capability. On the other hand, all of the PANBA-PPy samples decomposed at temperatures higher than 350 °C and an increase in the PPy content reduced the thermal stability of the samples slightly. In addition, the PANBA-PPy6 sample showed clear weight loss caused by the decomposition of PPy, even though the loss was much smaller than that caused by the decomposition of random PANBA blocks in the PANBA-PPy.

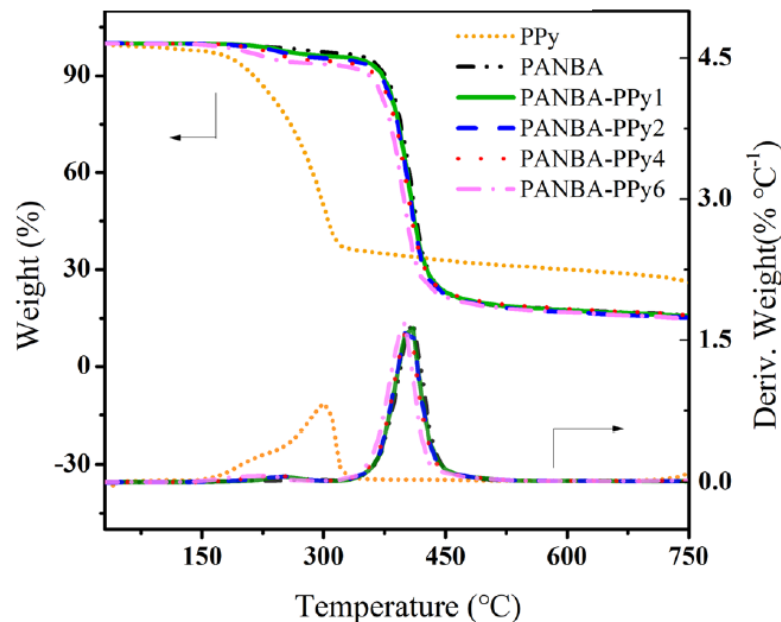


Figure 17: TGA results of the PANBA-PPy samples and PPy.

4.1.1.5 Contact angle

To check the wettability of the PANBA-PPy binder over the electrolyte, the contact angle of an electrolyte droplet placed on the binder film was measured as a function of time; the results are shown in Fig. 18. The contact angle provides information on the affinity between the polymer binder and the electrolyte. A lower contact angle generally indicates higher affinity between the polymer and electrolyte and implies a favorable circumstance for the transport of lithium ions in the electrolyte through the binder film. As shown in Fig. 4a, after placing an electrolyte droplet onto the binder film, the contact angles of all the samples were quite stable for 60 s. The increase in PPy content reduced the contact angle considerably from 75° for PANBA to approximately 30° for 4 or 6 g of PPy-containing PANBAPPy. This might be due to the hydrogen bonding between the NH groups in the PPy and the carbonyl groups in the carbonates of the electrolyte. Geißler et al. [48] suggested that a hydrogen bond arises from the interactions between the carbonyl groups in the insulating poly(bisphenol-A-carbonate) polymer and NH groups in the PPy. In addition to hydrogen bonding, the use of an extra SDS surfactant during PPy polymerization might also contribute to the lower contact angle by decreasing the surface tension.

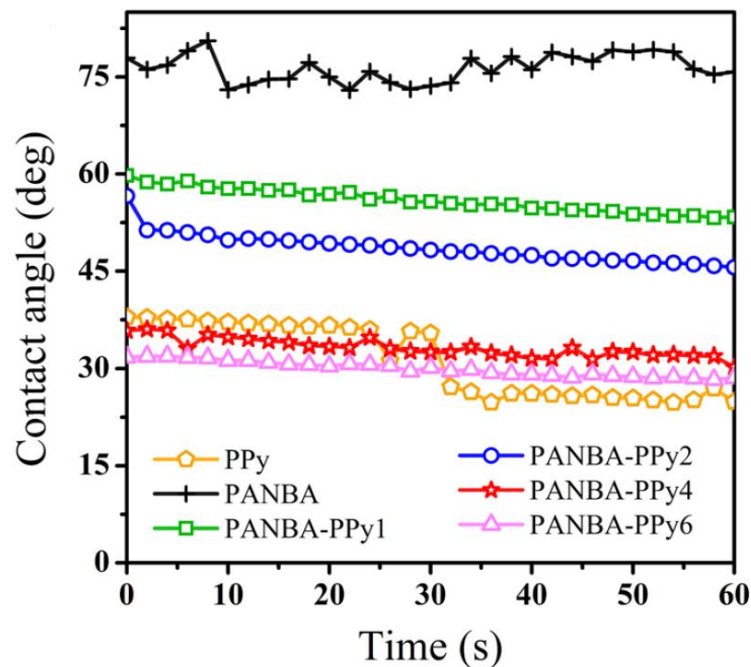


Figure 18: Contact angle of an electrolyte droplet placed on the binder films as a function of time.

4.1.1.6 Adhesive test

The adhesion strength of the LTO electrodes containing different PANBA-PPy binders was examined, even though the adhesion property of the LTO is not as important as that for graphite or silicon electrodes experiencing relatively large volume changes during cycling [49]. The LTO electrode has almost zero strain during use so that its electrochemical cycling performance is quite stable for lengthy cycling durations without mechanical damage, such as cracks and delamination. Nevertheless, critical adhesion for manufacturing the electrode and enduring the high current cycles is required for the LTO electrodes. Figure 19 presents the adhesion strength of the LTO electrodes measured through 180° peel tests. As expected from the lower contribution of PPy to the adhesion and its morphology shown in Fig. 15, an increase in the amount of PPy in the binder content decreases the adhesion of the LTO electrodes gradually.

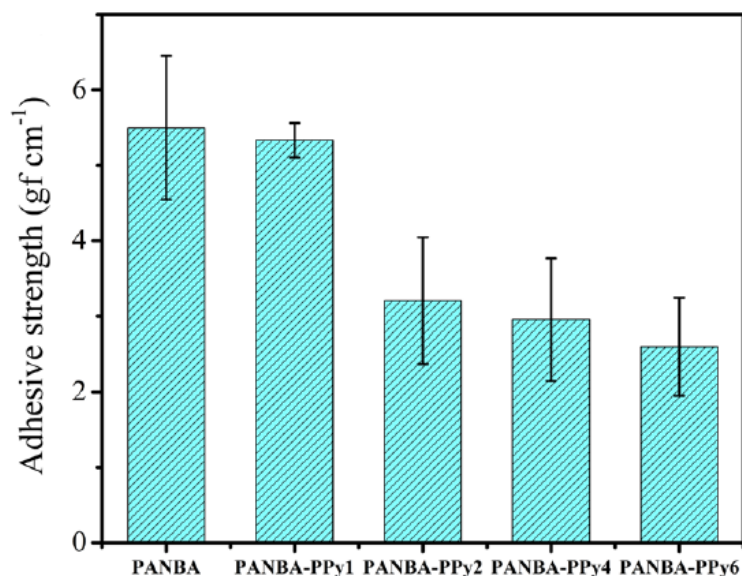


Figure 19: 180° peel strength of the LTO electrodes containing different PANBA-PPy samples as a binder.

4.1.2 Electrochemical properties

4.1.2.1 Cycling performance

The cycling performance of the LTO electrodes using the synthesized binders was characterized, as shown in Fig. 20. Compared to previous studies [49], [50], the initial coulombic efficiency of 95.6% for the non-conductive PANBA-containing electrode was higher, and the results were much better for the conductive PANBA-PPy samples, up to 98.6%. In addition, all the LTO electrodes containing the PANBA-PPy samples showed very stable capacities for 100 cycles at 1 C with capacity retention in the range of 94.7–96.8%. The PANBA-PPy4 sample showed the highest cycling capacity of 162.62 mAh g⁻¹ at the 100th cycle, which is close to the theoretical capacity of 175 mAh g⁻¹. In contrast, the PANBA-containing LTO electrode retained only 88.9% of its original capacity. This can be explained by the higher electrical conductivity (see Table 2) and better electrolyte wettability (see Fig. 18) of the PPy-containing binders, providing more effective ways for electron and ion transfer, respectively. These led to relatively small capacity loss in PANBA-PPy2, PANBA-PPy4, and PANBA-PPy6 electrodes compared to the PANBA-PPy1 and PANBA electrodes. This helps confirm the effect of PPy conducting moiety in the PANBA-PPy binders on enhancing the electrochemical performance of the LTO electrodes.

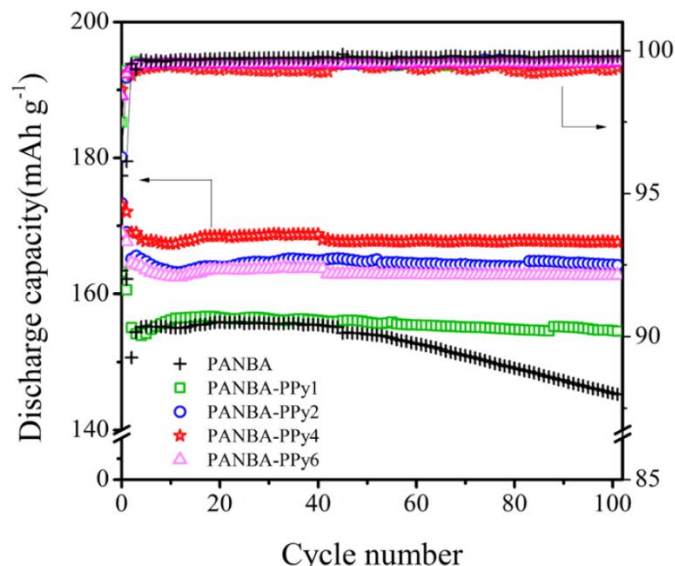


Figure 20: Cycling performance of the $\text{Li}_4\text{Ti}_5\text{O}_{12}$ electrodes at rates of 0.1C for the first two cycles and 1C for the subsequent 100 cycles.

4.1.2.2 Electrochemical impedance spectra (EIS) performance

Figure 21 shows the EIS results of the five-cycled LTO electrodes. The charge transfer resistance of the electrodes was determined from the size of the semicircles at the middle frequency range. These were 22.58 Ω , 19.23 Ω , 17.47 Ω , 14.29 Ω , and 17.93 Ω for the PANBA, PANBA-PPy1, PANBA-PPy2, PANBA-PPy4, and PANBA-PPy6-containing electrodes, respectively. The LTO electrodes containing the PPy component in the binder have lower charge transfer resistance than those composed of the PANBA binder only. In particular, the PANBA-PPy4-containing LTO electrode has the least charge transfer resistance. Obviously, the improvement in the electrical conductivity and ion transportation helps reduce the charge transfer resistance for the electrochemical reactions. On the other hand, the LTO electrode containing PANBA-PPy6 showed relatively larger charge transfer resistance than that of the PANBA-PPy4 sample. This may be due to the loose electrode contact to the current collector caused by the relatively low adhesion of the PANBA-PPy6 sample, as shown in Fig. 19. Nevertheless, the impedance result is in accordance with the cycling performance result.

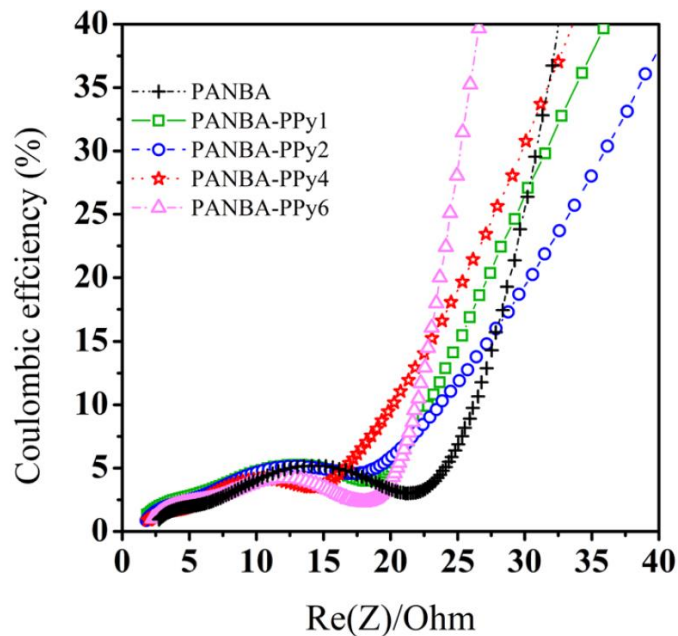


Figure 21: Electrochemical impedance spectra (EIS) of the $\text{Li}_4\text{Ti}_5\text{O}_{12}$ electrodes after charging and discharging at 0.1C for two cycles and 0.5C for a further three cycles.

4.1.2.3 High rate performance

Separately, the effects of the conductive PANBA-PPy binders on the rate capability of the LTO electrodes were investigated, as shown in Fig. 22 (left). As expected, the LTO electrodes using the conductive PANBA-PPy binders exhibited much better performance than the non-conductive PANBA binder for any current density. In particular, the difference in performance between the conductive and non-conductive binders was slightly clearer at relatively large current densities. Of the conductive binder, the PANBA-PPy2 samples showed the best rate capability with high cycling capacity. To observe the difference clearly, Fig. 22 (right) shows the percentage of average capacity at a certain current density compared to the average capacity at 0.1 C. At relatively low current densities (< 1 C), there was little difference among PANBAPPy1, PANBA-PPy2, and PANBA-PPy4. They maintained greater than 95% capacity at 1 C, compared to that at 0.1 C. The difference became greater as the current density was increased. At the highest charge/discharge currents of 10 C, the PANBA-PPy2-containing LTO electrode was found to be superior to any other conductive PANBA-PPy binders. This was attributed to the mechanical strength of the electrodes. The electrode can be damaged easily at such a large current, so that it is favorable to have high mechanical strength imparted by the adhesion. This is why the PANBA-PPy2 sample exhibited better rate capability than the PANBAPPy4 sample, which has the best cycling performance, as shown in Fig. 20, even though the electronic and ionic transport of PANBA-PPy2 were inferior to those of PANBAPPy4. The electrodes recovered their capacities up to 93% when they were returned to 0.1 C from 10 C current rates.

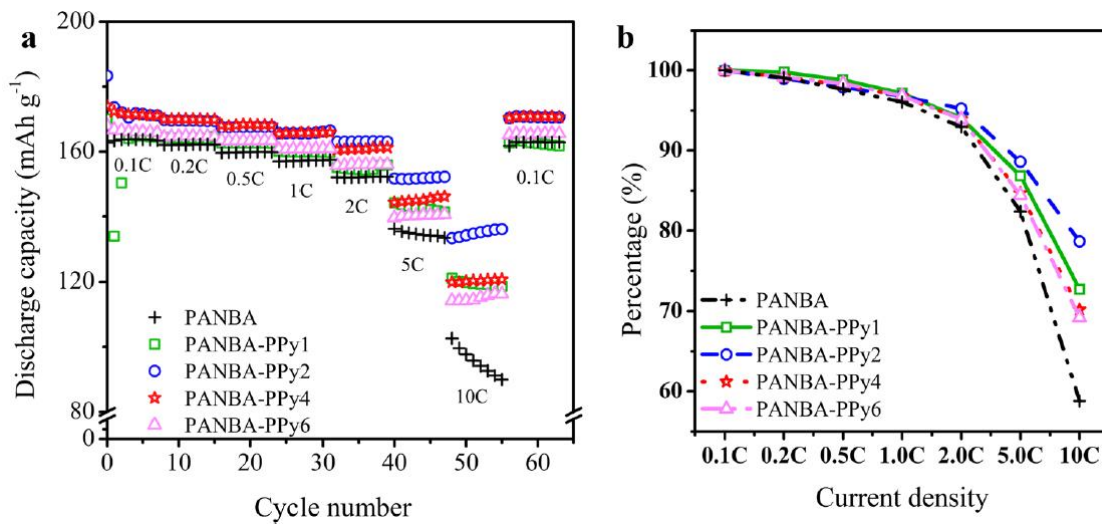


Figure 22: High rate performance.

(left) Cycling behavior of the Li₄Ti₅O₁₂ electrodes at rates of 0.1C, 0.2C, 0.5C, 1C, 2C, 5C, and 10C. (right) Percentage of the average capacity at a certain current density compared to the average capacity at 0.1C.

4.2 POLYPYRROLE-POLY (ACRYLONITRILE-BUTYL ACRYLATE)

4.2.1 Physical properties

4.2.1.1 Stability

The water-based binder should be able to storage for a long term before making into supercapacitor electrodes. So, its necessary to record stability of polymer solution after polymerization. In this study, we scan the polymer solution every 30 min at a constant temperature of 30 °C for 24 h. The examination was carried out in the Turbiscan station which was mentioned in our previous work[51]. And the Turbiscan Stability Index (TSI) has been representing by times as Fig. 23. The much lower TSI values of PPy-PANBA demonstrate that it is a stable polymer used as a binder. And it can be storage at least 24 h before making supercapacitor electrodes.

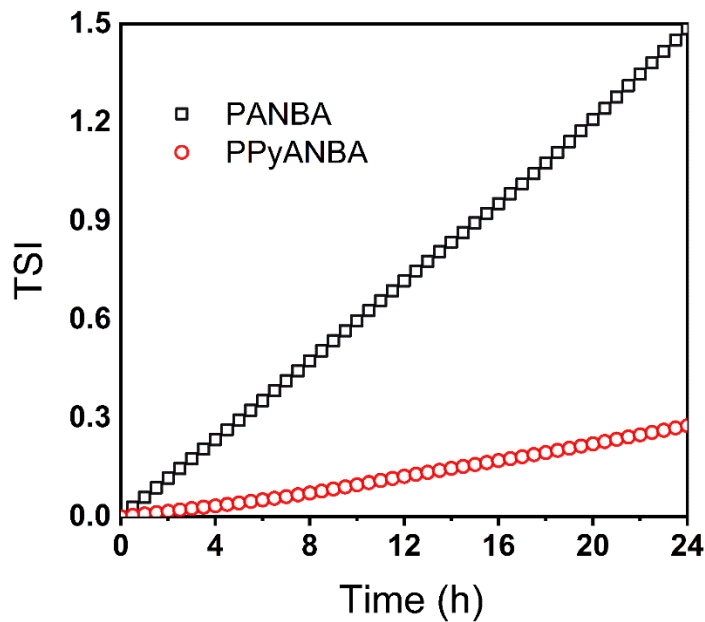


Figure 23: Turbiscan stability index of polymer solution displayed in one day.

4.2.1.2 FTIR

The successful synthesis of PPyANBA is also confirmed from the FTIR spectra of the PPy, PANBA, and PPyANBA binder films, as shown in Fig. 24, with those of polyacrylonitrile (PAN) and polybutylacrylate (PBA). The characteristic peaks of PPy are visible at 1168 cm^{-1} and 1644 cm^{-1} for C=N, at 1464 cm^{-1} and 1537 cm^{-1} for C=C, and at 1300 cm^{-1} for C-N [52], [53]. As shown in the FT-IR spectra of PAN and PBA, the characteristic peaks of PANBA at 1780 cm^{-1} and 2240 cm^{-1} are assigned to the stretching vibrations of carbonyl groups in butyl acrylates and of nitrile groups in acrylonitrile, respectively [54], [55]. All the above peaks are present in the PPyANBA spectrum, which implies that the in-situ emulsion polymerization of PPyANBA is successfully achieved.

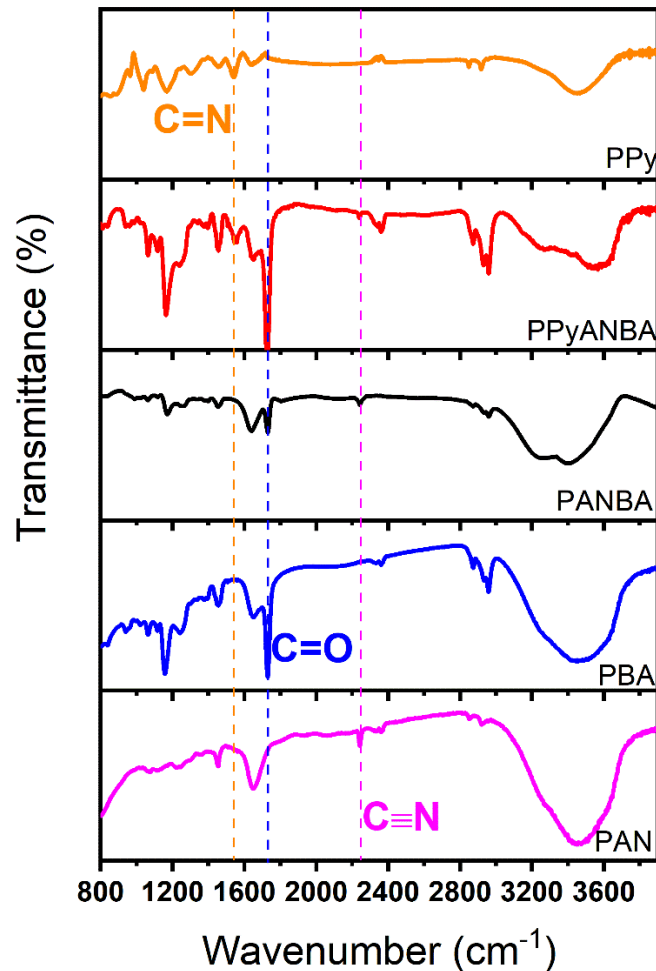


Figure 24: FTIR spectrum of binder film.

4.2.1.3 Resistance test by electrochemical impedance spectra (EIS).

In this study, we introduced conductive polymer PPy to increase the PANBA's conductivity. For proving that, we assembled CR2032 cells with the same thickness polymer film inside only, and the electrochemical impedance spectra (EIS) had been tested at a frequency from 10^5 Hz to 10 Hz. The cells resistance and capacitance in EIS has been simulated as a resistor and a capacitor in series respectively. We can record the cells impedance information at a high frequency. Especially we can get the resistance value when the frequency is infinite [56]. Base on this, we did linear for two samples impedance at high frequency, and PPy-PANBA group shows more than half smaller resistance (1.04 k Ω) than PANBA (2.35 k Ω). In other words, PPy-PANBA revealed that conductive PPy worked with PANBA, and PPy-PANBA is a much more conductive binder than PANBA, and it can be a potential conductive binder apply on supercapacitor electrodes.

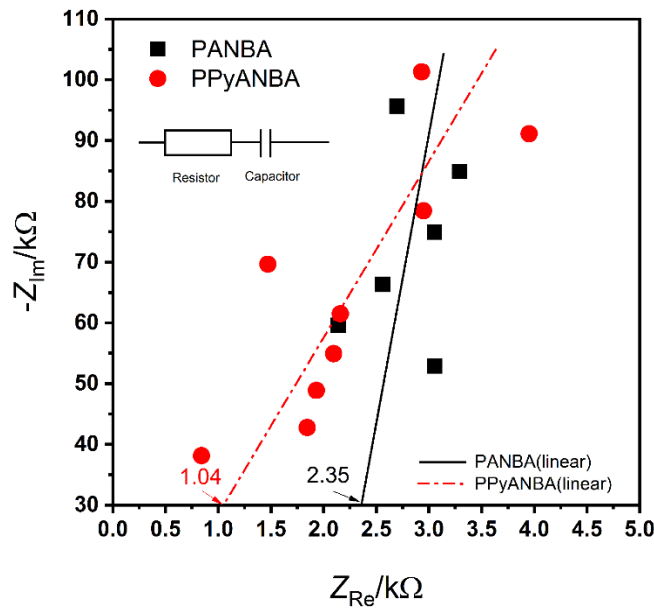


Figure 25: The resistance of polymer film examined by electrochemical impedance spectra (EIS).

4.2.1.4 TGA.

The thermal characteristic of the synthesized binders is investigated by DSC and TGA analyses, and the results are displayed in Fig. 26. Due to the relatively high T_g of PPy ranging between 65–95 °C [57], the T_g of PPyANBA slightly increases to 6.6 °C from 4.5 °C of PANBA. Such a low increase does not substantially change the rubbery state of the emulsified binders because the electrode works normally at room temperature, which is much higher than the T_g . In addition, as shown in Fig. 26(b), the thermal stability of the binders is almost unchanged by the in-situ polymerization of PANBA within PPy emulsion. Both PANBA and PPyANBA are thermally stable up to 350 °C. By contrast, the PANBA mixed physically with the same amount of PPy as PPyANBA shows considerably larger weight loss between 200 and 300 °C compared to those of both PANBA and PPyANBA. The temperature corresponds to the decomposition of PPy [51]. In summary, this in-situ emulsion polymerization is an efficient way to introduce a conducting polymer into a rubbery nonconducting polymer without losing its thermal characteristics.

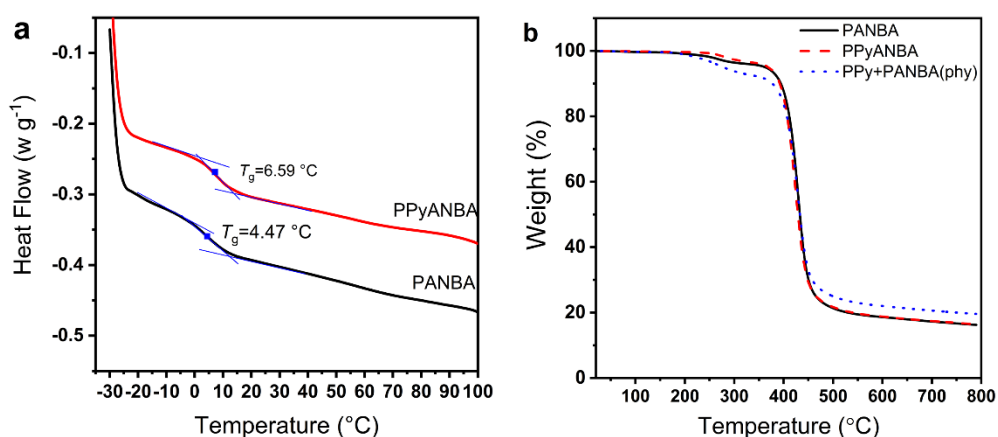


Figure 26. (a) DSC and (b) TGA of the polymer films. Here, PPy+PANBA(phy) indicates the PANBA mixed physically with 1 wt% PPy.

4.2.1.5 Zeta potential

The zeta potential and glass transition temperature (T_g) of different binder have been measured as shown Table. 3. Both PANBA and PPyANBA particle surface perform negative charge. It may due to the anionic surfactant SDS surrounding polymer particles. Besides, PPyANBA polymer particles' zeta potential absolute value is larger than PANBA which implying there is a stronger electrostatic force among PPyANBA particles. This result in a much more stable property of PPyANBA which is agree with the long term stability results tested by Turbiscan.

Another important polymer thermal propterty is the polymer T_g. The PANBA and PPyANBA polymer film T_g are shown as Table. 3. Due to the present of PPy, the PPyANBA T_g is bigger than PANBA. It is probably because that PPy has a T_g range 65-95 °C [57]. Consequently, the movement of PPyANBA polymer chain is not as freedom as PANBA. In other words, T_g is a proof that polymerization of PANBA with PPy is accomplished.

Sample	Zeta Potential (mV)	T _g (°C)
PANBA	-45.7	4.74
PPy-PANBA	-52.4	6.59

Table 3: Zeta potential and glass transition temperature of PANBA and PPyANBA.

4.2.1.6 Contact angle (CA)

The contact angle can reveal wettability of binder film, and the relationship between binder film and electrolyte. The contact angle between binder film and electrolyte droplet had been recorded during 40 s in an optical tensiometer (Theta Lite, Biolin Scientific) as shown in Fig. 27. These two kinds binder films show similar contact angle during measurement which demonstrates that PANBA and PPyANBA have a similar surface function groups. As time goes by, the contact angle keeps going down from around $\theta = 53^\circ$ to $\theta = 37^\circ$. It means that both PANBA and PPyANBA binder film have a good wettability with electrolyte.

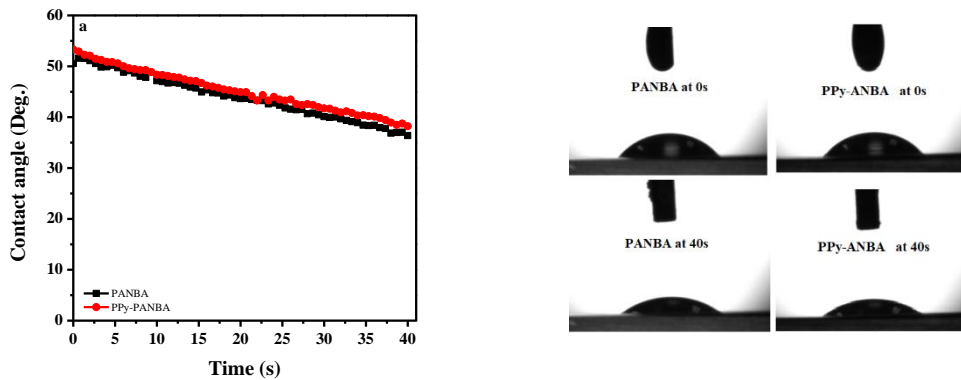


Figure 27: Contact angle of binder film.

(a) Contact angle of an electrolyte droplet fell down onto the binder films during the 40 s. (b) Photographs of the electrolyte droplet over binder film at 0 s and 40 s respectively.

4.2.1.7 Adhesion strength

The adhesion strength between collector and electrode except etching Al foil of a different kind of binder with an error bar, as shown in Fig. 28. Since, styrene butadiene rubber (SBR, 400B) has been known as a high adhesive water-based binder, especially, co-working with CMC as a binder for supercapacitors [58], and lithium-ion battery electrodes [54], [56], it also has been tested and compared. The inserted graph gives the adhesive property information of PANBA and PPyANBA intensively. Comparing with SBR, PANBA and PPyANBA samples show similar adhesion strength which is around 1/6 of SBR. As we know, due to the high adhesion strength can support a good connection among electrode components and stick electrode components on collectors. It plays a key role in high rate current charge/discharge performance. This adhesion strength results agree well with these three kinds of binder supercapacitor results while the charge/discharge current flow at 100mA/cm².

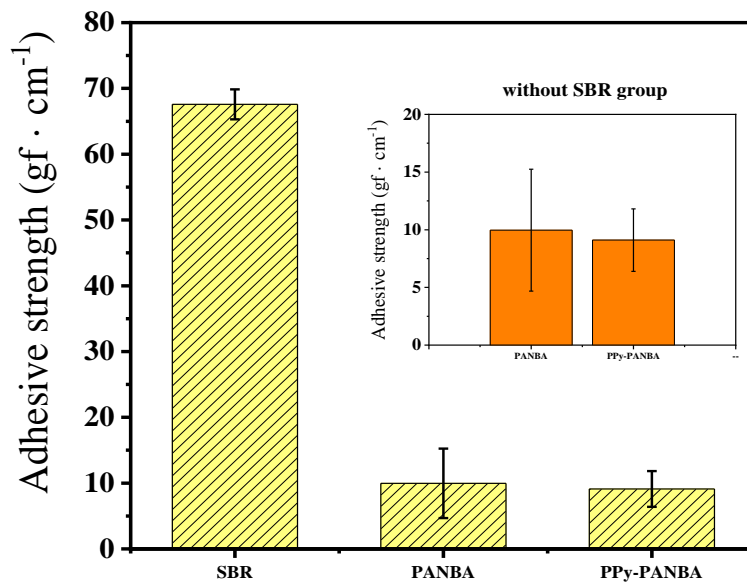


Figure 28: The adhesion strength value of SBR, PANBA, and PPyANBA supercapacitor electrodes with an error bar.

4.2.1.8 BET

In general, the specific surface area (SSA) and the porosity characteristic of the electrode affects the electrochemical performance of EDLCs. In particular, a large SSA can provide more space for charge storage and thus leads to a higher capacitance [59]. The EDLC electrode powders containing PANBA or PPyANBA binder have been degassed at 300 °C for 24 h before BET analysis. The results of nitrogen sorption isotherms performed at 77 K are shown in Fig. 29(a). Both of the electrodes exhibit mainly Type I isotherm curves combined with Type IV behavior. The dramatic increase in the isotherm curves at a relatively low pressure ($P/P_0 < 0.1$) is attributed to the presence of a large number of micropores. The H4 hysteresis loops in the range of $P/P_0 = 0.4-0.9$ indicate the presence of a small number of mesopores [60]. These are confirmed from Fig. 29(b) and Table 4. Figure 29(b) exhibits their pore size distribution measured using the BJH method. The electrodes are mainly composed of both micropores ($d < 2$ nm) and mesopores ($d = 2-50$ nm) without any sensible difference. The majority of mesopores are located between 3.0 - 4.5 nm regardless of the binders. More clear data on the SSA of the pores are listed in Table 4. The PPyANBA-containing electrode powder has higher SSA than the PANBA-containing electrode, even though the PPyANBA binder has a slightly larger size than the PANBA binder, as shown in Fig. 4. In general, bigger binder particles may block larger amounts of pores in the electrode powders. Therefore, the higher SSA of the PPyANBA-containing electrode powder may be attributed to the improved dispersion of the PPyANBA binder particles proven by the zeta potential and TSI values, leading to the homogeneous dispersion and less blocking of binder particles in the electrode, and thus, higher SSA.

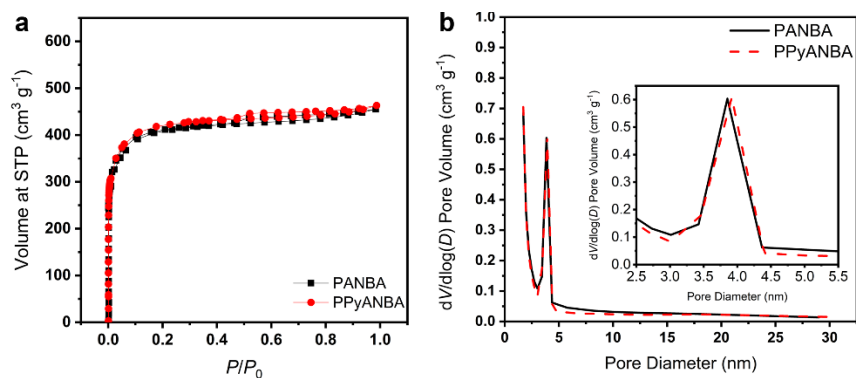


Figure 29: BET results.

(a) Nitrogen adsorption/desorption isotherms curves of supercapacitor electrodes. (b) Electrodes pore diameter distribution based on the BJH method.

	S_{BET}	S_{micro}	S_{meso}	Pore V_{total}
	(m² g⁻¹)	(m² g⁻¹)	(m² g⁻¹)	(cm³ g⁻¹)
PANBA	1517	1222	295	0.70
PPyANBA	1585	1280	305	0.72

Table 4: Porosity parameters of supercapacitor electrodes.

4.2.2 Electrochemical properties

4.2.2.1 CV

Base on the electrolyte we use, the cyclic voltammetry (CV) was carried out between voltage 0 and 3V at scan rate 5 mV/s, 20 mV/s, 50 mV/s, 100 mV/s, respectively. The response of SBR, PANBA, PPyANBA types CR 2032 supercapacitors current was recorded as Fig. 30. All groups show formal and neat shape without any faradaic peak. These display a normal supercapacitor CV looks and without any redox reaction happened during the test. The symmetric shape of CV did not change while increasing the scan rate. This manifest that the charge exchanges freely during the positive sweep signal and negative sweep signal [61]. And it is probable the reason for their stable and reversible charge/discharge performance.

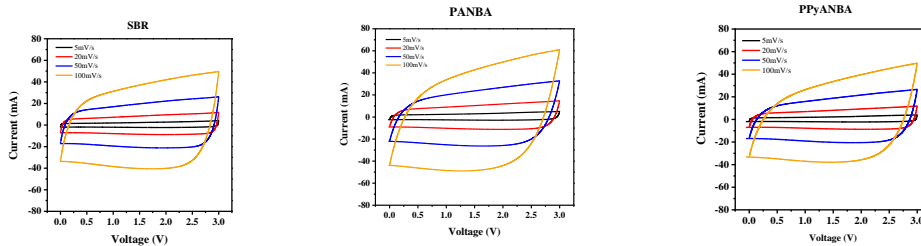


Figure 30: Cyclic voltammograms (CV) of the CR 2032 supercapacitors at various scan rates, 5 mV/s, 20 mV/s, 50 mV/s, 100 mV/s.

4.2.2.2 Electrochemical impedance spectroscopy (EIS) performance.

For a thorough assessment of our supercapacitor, it is essential to examine the inter resistance and charge transfer resistance of a supercapacitor. The electrochemical impedance spectroscopy (EIS) is the best way to acquire this information detailly. Fig. 31 illustrate the effect of PANBA and PPyANBA binder on supercapacitor electrodes impedance with a normal carbon-based supercapacitor impedance shape [62]. From the intercept, at high frequency part, a similar entire inter resistance that owing to the resistance from electrolyte solution and electrode active material is around 0.8Ω . However, the charge transfer resistance of PPyANBA (6.3Ω) is much smaller than PANBA (10.0Ω). This reveal that electrons transfer is easier in PPyANBA type electrodes than PANBA. It is probable taking account with PPy effect by its higher conductivity. This plays a crucial role in explaining why PPyANBA group supercapacitor has a better cycling performance.

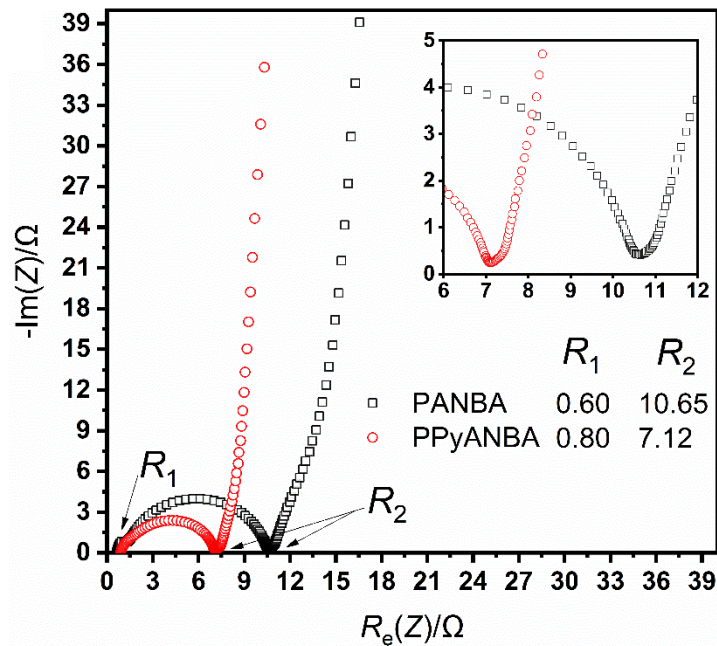


Figure 31: Nyquist plot of supercapacitor with the frequency from 10^6 Hz to 10^{-2} Hz at 0 V after 200 cycles.

4.2.2.3 Cycling performance.

The supercapacitor discharged specific capacitance(F/g) with different binder system have been recording as shown in Fig. 32. And the high adhesive SBR serve as a binder for supercapacitor has also been taken account for comparison. All the groups show stable cycle lives during 10,000 cycles with discharge specific capacitance retention over than 82 %. The PPyANBA shows the highest specific capacitance while PANBA sample exhibit the lowest. Besides, PPyANBA has the highest first discharge specific capacitance as 133.70 F/g (PANBA is 122.20 F/g, SBR is 125.72 F/g). This is probably because of the PPyANBA's conductivity. In addition, PPyANBA shows a higher discharge specific capacitance than high adhesive SBR binder. We can speculate that current at or below 4.00 mA, the conductivity is a more important property for supercapacitor cycling performance rather than adhesive property.

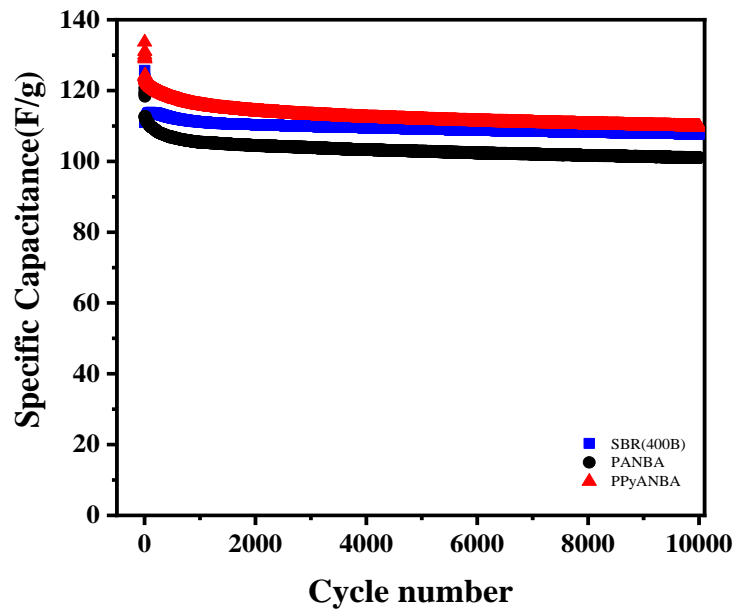


Figure 32: EDLCs cycling performance with different binder systems for 10,000 cycles.

4.2.2.4 High-rate performance.

For testing the supercapacitors capacitance change at a series of different current density (0.5 mA/cm^2 , 1.0 mA/cm^2 , 5.0 mA/cm^2 , 10 mA/cm^2 , 50 mA/cm^2), charge and discharge between 0.1 V and 2.7 V have been taken out for 20 cycles at each current density. Besides, the current back to 0.5 mA/cm^2 has also been examined to study their diversity and capacity retention percentage. As seen in Fig. 33, the general trend of specific capacitance of rate capability test agrees with the results of cycling performance at current density 0.5 mA/cm^2 , 1.0 mA/cm^2 . As current density increasing, the PANBA, and PPy-PANBA specific capacitance reduce more than SBR, and it is the fact that the specific capacitance values are identified with the adhesive value in Fig. 28. It is demonstrated that the adhesive characteristics decide supercapacitor specific capacitance performance when at high current flow. Which means, at high current the bonding property can provide more easier paths for electrons. In addition, the specific capacitance recover percentage of PANBA, PPy-PANBA and SBR are all over than 98 %. It proved that they could maintain a stable capacitance even after charging and discharging at high current density.

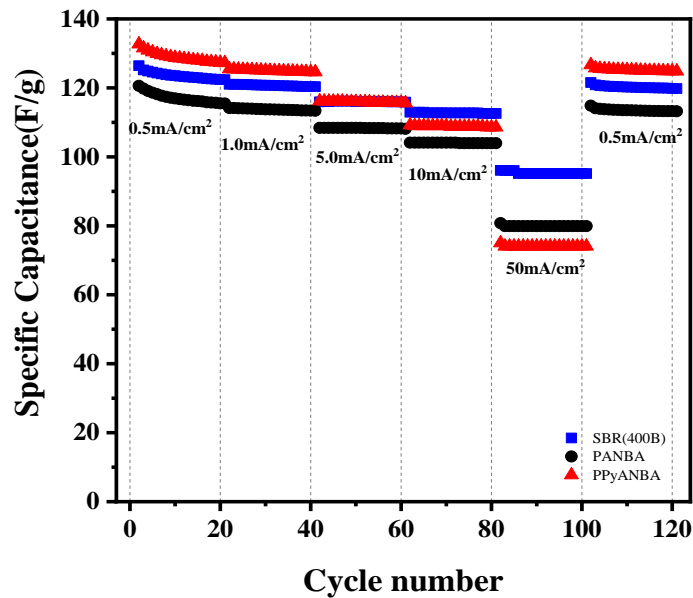


Figure 33: EDLCs rate capability performance with different binder system for 20 cycles at each current.

4.3 MXENE-POLY (ACRYLONITRILE-BUTYL ACRYLATE)

4.3.1 Physical properties

4.3.1.1 Raman

Raman spectra of the MXCs (Ti_2CT_x and $Ti_3C_2T_x$), PANBA, and the composite binder films are displayed in Fig. 34. The MXCs display peaks at 220 cm^{-1} corresponding to the vibration of nonstoichiometric Ti–C. The other peaks observed in the Raman spectra are attributed to the surface functional groups [40], [63]–[66]. The Raman spectra of PANBA shows notable peaks at 1731 cm^{-1} and 2240 cm^{-1} that are attributed to the carbonyl stretching vibration of butyl acrylate and the nitrile stretching vibration of acrylonitrile, respectively [67], [68]. The Raman spectra of both MXC1/PANBA and MXC2/PANBA consist of peaks from both MXCs and PANBA, which implies successful polymerization of PANBA with the addition of MXCs.

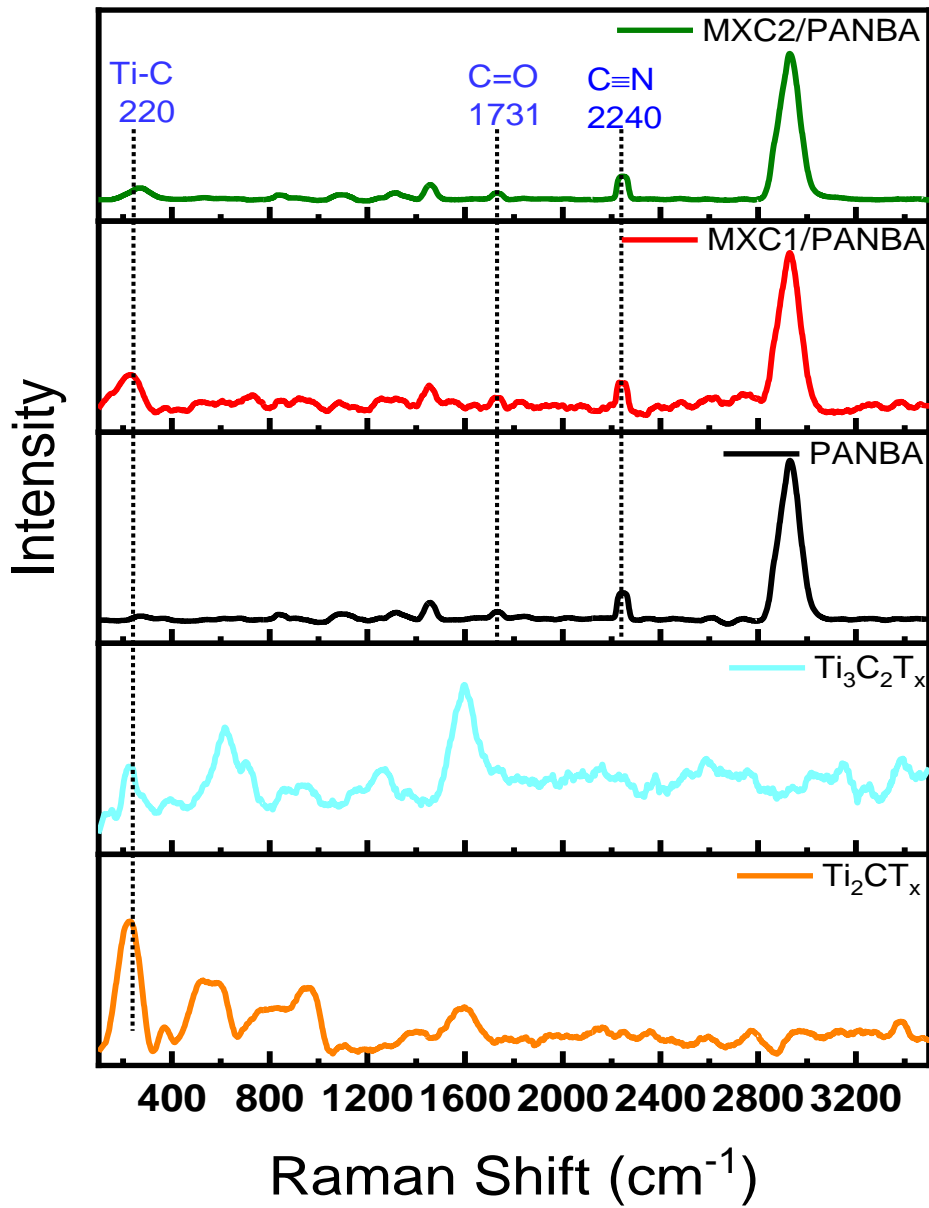


Figure 34: Raman spectra of PANBA, MXCs/PANBA binder film and MXenes.

4.3.1.2 FTIR

we examined the functional groups in MXC/PANBAs and PANBA by FT-IR spectroscopy (Fig. 35). For all samples, the characteristic peak at 1763 cm^{-1} is due to the carbonyl stretching vibration in the butyl acrylate[55], and the peak at 2240 cm^{-1} is due to the nitrile stretching vibration in the acrylonitrile[54]. This also confirms the successful polymerization of the PANBA with the MXCs. In addition, the peak observed at 3384 cm^{-1} for the MXCs/PANBA may be attributed to the stretching vibration of intermolecular hydrogen bonds formed between the MXC and the PANBA[38], [69].

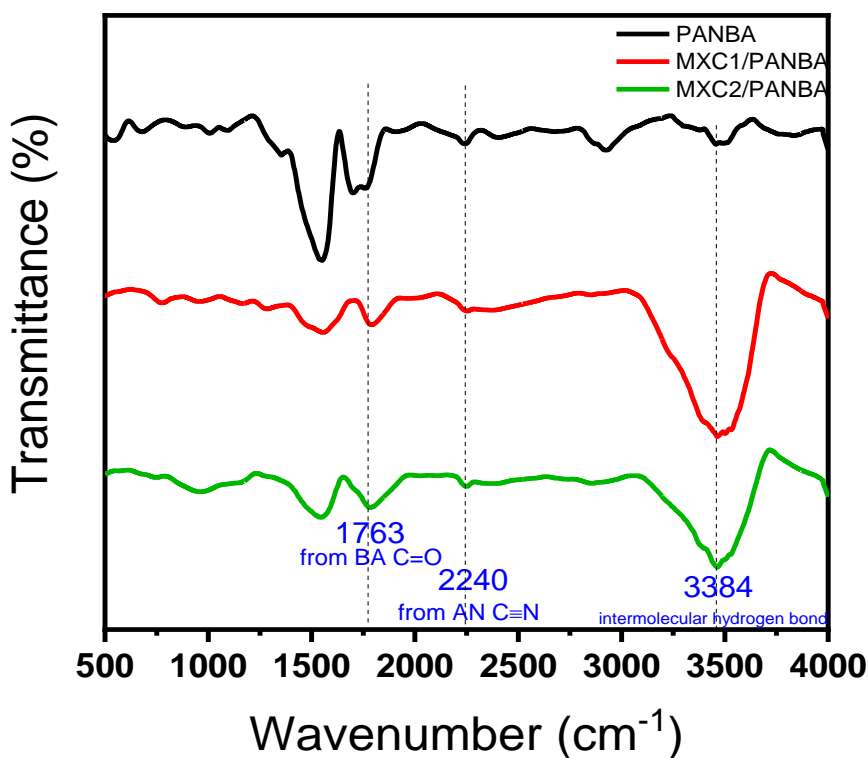


Figure 35: FT-IR spectra of PANBA, MXCs/PANBA binder film.

4.3.1.3 Zeta Potential

The zeta potential and the ion conductivity of polymer solution were measured by the electrophoresis method which is based on Henry equation, and the values are listed in Table. 5. The negative charges on all the samples are due to the anionic surfactant sodium dodecyl sulfonate, which was used during the emulsion polymerization. Moreover, the MXenes increase the absolute value of zeta potential, indicating stronger electrostatic repulsive forces among MXCs/PANBA particles. Consequently, there will be less chance for flocculation, aggregation, and agglomeration of MXCs/PANBA particles than PANBA. Besides, the MXene slightly increases the ion strength of MXCs/PANBA, since the electrical double layer have been compressed as the present of MXene in solution. It is probably due to the MXene changed the concentration of polymer solution.

Sample Name	Zeta Potential	Mobility	Conductivity
unit	mV	$\mu\text{mcm/Vs}$	mS/cm
PANBA	-56.6 ± 1.1	-4.6 ± 0.2	6.0 ± 0.2
MXC1/PANBA	-64.9 ± 1.7	-5.1 ± 0.1	7.8 ± 0.1
MXC2/PANBA	-57.1 ± 0.8	-4.5 ± 0.1	7.4 ± 0.1
MX1	-23.2 ± 0.4	-1.8 ± 0.03	0.2 ± 0.003
MX2	-29.6 ± 0.8	-2.3 ± 0.07	0.3 ± 0.004

Table 5: Zeta potential of polymer solution.

4.3.1.4 SEM

The FE-SEM analysis results of the as-received MXC2 and synthesized MXC2/PANBA binder are shown in in Fig. 36. FE-SEM images of MXC1 and MXC1/APNBA are not shown in the text. The as-received MXC2 showed a multilayered morphology as expected. [70]–[72]. The lateral size of the multilayered MXC2 was $\sim 7\ \mu\text{m}$. The sonication step done before polymerization may exfoliate some multilayers of the MXC2 into single thin layers. The polymerized MXC2/PANBA sample shows the presence of spherical PANBA particles attached to the surface of MXC2, which were not observed in the SEM images of the physically mixed PANBA + MXC2 sample (Fig. 36(b)-(c)). This may be attributed to the hydrogen bonding interactions between the functional groups ($=\text{O}$, $-\text{COO}$) of PANBA and the MXC2 termination groups ($-\text{OH}$, $-\text{F}$, $=\text{O}$) [38], [39], as confirmed from the FT-IR in Fig. 35.

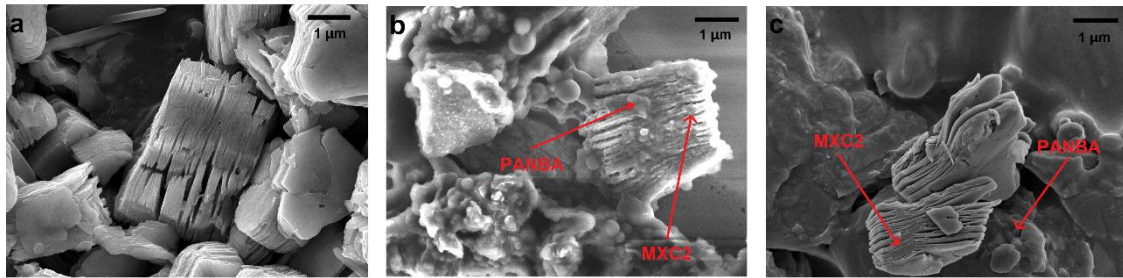


Figure 36: FE-SEM images.

(a) MX2 (Ti₃C₂T_x) powder and (b) MXC2/PANBA (c) MXC2+PANBA

4.3.1.5 DSC

For comparing the difference between polymerization of MXCs/PANBA and simply physical mixing of MXene with PANBA (MXCs+PANBA), their film glass transition temperatures (T_g) was measured and listed in Table. 6. As expected, the T_g of MXCs/PANBA increased compared to PANBA, whereas almost no change appeared in the T_g of the sample which was simply mixed. This implies that MXene confines the movement of polymer chains resulting in hindering the polymer flexibility. Combined with FT-IR in Fig. 35 and FE-SEM in Fig. 36, these results confirm that the polymerization of PANBA on the surface of MXCs leads to strong interaction between MXCs and PANBA.

	PANBA	MXC1+PANBA	MXC2+PANBA	MXC1/PANBA	MXC2/PANBA
T_g (°C)	4.3±0.1	4.5±0.1	4.5±0.1	9.3±0.3	5.3±0.4

Table 6: Glass transition temperature of polymer films.

4.3.1.6 Polymer sheet resistance test by IMP

The electrical resistance of the PANBA, MXC1/PANBA, and MXC2/PANBA binders alone were measured using AC impedance spectroscopy. Binder films with a thickness ranging from 25 - 35 μm cast on e-Al foil were placed between two stainless-steel spacers in a CR2032 coin cell without added electrolyte. The Nyquist plots shown in Fig. 37 consist of semi-circles. The data from this plot were fitted using an equivalent circuit consisting of a resistor and capacitor in parallel (inset on Fig. 37), which is a typical circuit for a single dominant pathway for the charge transport [73], [74]. The intercept of the semicircle with the real axis marks the bulk resistance for the migration of electronic charge in the binder film over the applied electrical field[73]–[76]. The values of the electrical resistance are provided in the table in the figure inset. The addition of MXCs significantly lowered the electrical resistance as compared to the PANBA binder film (Fig. 37). Additionally, the polymerized MXC/PANBA samples showed much lower electrical resistance (MXC1/PANBA – 604.6 Ω and MXC2/PANBA – 655.0 Ω) as compared to physically mixed MXC+PANBA samples (MXC1+PANBA – 937.3 Ω and MXC2+PANBA – 2117.8 Ω).

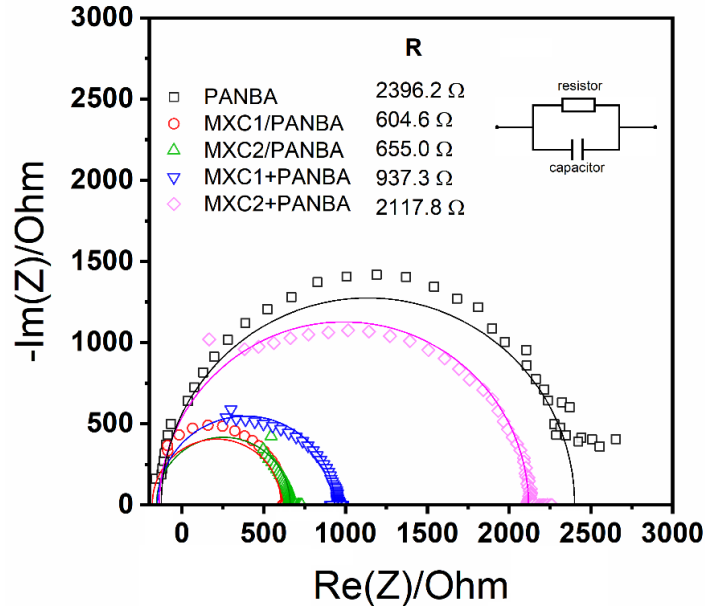


Figure 37: Nyquist diagram of polymer membrane and linear correlation with Equivalent circuit (upper right corner).

4.3.1.7 BET

EDLC electrodes were prepared by mixing YP-50 activated carbon, Super P carbon black, CMC, and the as-synthesized binder in the weight ratio of 91.5:2.5:1.5:4.5, respectively. Three such EDLC electrodes were fabricated and they were denoted as EDLC-M0 (consisting of PANBA binder), EDLC-M1 (consisting of MXC1/PANBA binder), and EDLC-M2 (consisting of MXC2/PANBA binder). We first performed BET analysis on the electrodes to determine the specific surface area and porosity of the fabricated electrodes. The capacitances of EDLCs are highly dependent upon the specific surface area (SSA) and pore characteristic of EDLC electrodes. In general, a higher SSA provides more area for charge distribution, leading to a higher capacitance. However, the polymer binder inevitably blocks the pores, which decreases the electrode capacitance. Therefore, the effect of the binder on the surface area and porosity was first examined before the subsequent electrochemical tests. For BET analysis, all samples were degassed at 300 °C for 20 h. As depicted in Fig. S5, all samples show type I isotherm curves combined with type IV having H4 hysteresis loops[60]. Almost no difference in terms of the pore size distribution of electrodes was observed, regardless of the binders used. The majority of mesopores (2~50 nm pore diameter) are in the range of 3.0 – 4.5 nm, which is sufficiently large to allow the passage of electrolyte ions, such as TEA⁺ of 1.30 nm and BF₄⁻ of 1.16 nm[77]. Further data on the porosity is provided in Table 1. The electrodes containing the MXC/PANBA binders, EDLC-M1 and EDLC-M2, showed slightly lower SSAs as compared to the electrode containing the PANBA binder, EDLC-M0. This can be attributed to pore-blocking caused by MXCs. The pore blocking (in %) is quantified through the change in pore volume as compared to the volume of the pristine YP-50F active material. The values of $\Delta V/V$ for EDLC-M1 and EDLC-M2 are 11.5 % and 14.1%, respectively, whereas the EDLC-M0 electrode has 9.0% pore blocking. This supports our claim that the MXCs probably block some of the pores in the electrodes. Moreover, the MXC1/PANBA binder blocks the mesopores less than the PANBA binder does, although the difference is not substantial. The surface area of the mesopores is closely related to the capacitance of the EDLCs because the movement of ions is relatively free in the mesopores, which leads to higher capacitance[78], [79].

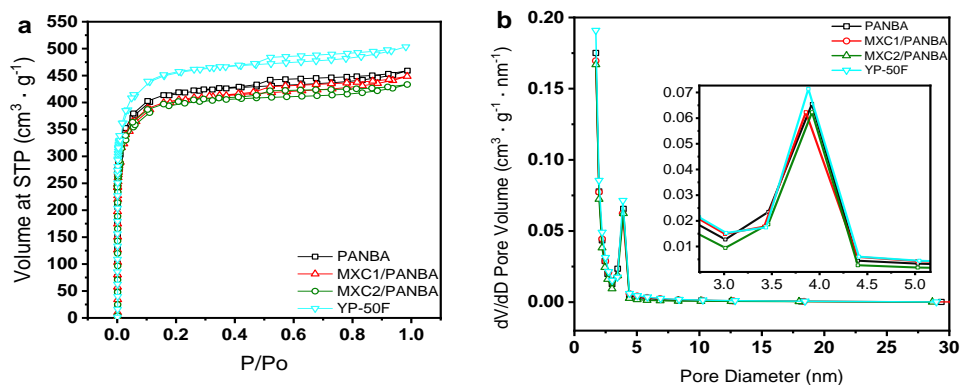


Figure 38: BET results.

(a) Nitrogen adsorption/desorption isotherm curves of the EDLC electrodes; (b) pore diameter distribution of the electrodes based on the BJH method.

	S_{BET} ($\text{m}^2 \text{g}^{-1}$)	S_{micro} ($\text{m}^2 \text{g}^{-1}$)	S_{meso} ($\text{m}^2 \text{g}^{-1}$)	$V_{\text{total pore}}$ ($\text{cm}^3 \text{g}^{-1}$)	$\Delta V/V$ (%)
YP-50F	1524.5	1215.3	309.2	0.8	-
EDLC-M0 (PANBA)	1392.5	1106.1	286.4	0.7	9.0
EDLC-M1 (MXC1/PANBA)	1373.9	1082.5	291.4	0.7	11.5
EDLC-M2 (MXC2/PANBA)	1354.3	1072.0	282.3	0.7	14.1

Table 7: Porosity parameters of supercapacitor electrodes excluding collectors.

4.3.1.8 Adhesive test

As we know, due to the high adhesion strength can support a good connection among electrode components and stick electrode components on collectors providing much easier path for electrons. It plays a key role in high-rate current charge/discharge performance. So, the adhesion strength between collector and electrode except e-Al foil with different kinds of binder with an error bar have been considered and shown as Fig. 39. Ti₂CTx and Ti₃C₂Tx decrease binder adhesive property.

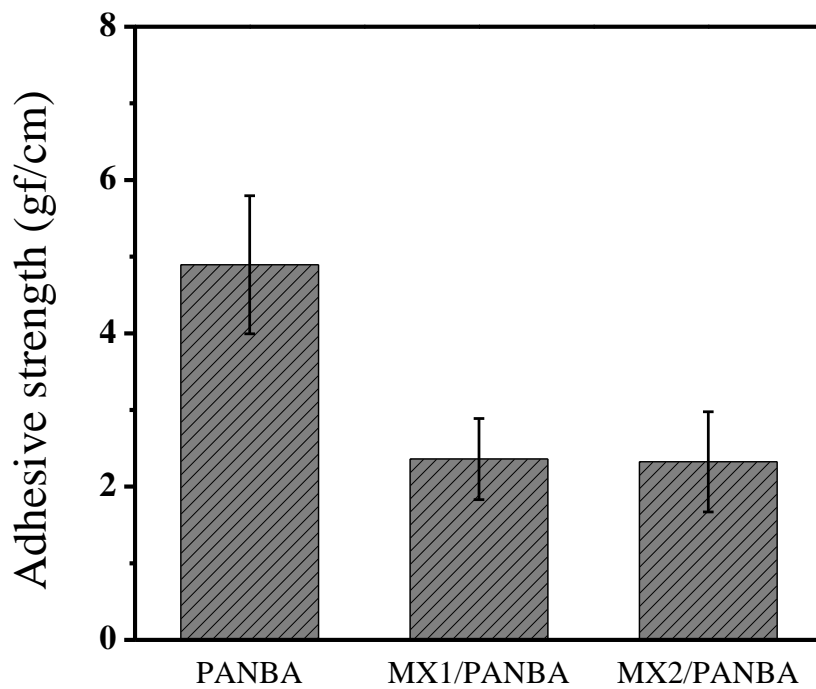


Figure 39: The adhesion strength of PANBA, and MXs/PANBA EDLCs electrodes with error bars.

4.3.2 Electrochemical properties

4.3.2.1 Cycling performance of EDLCs without conducting agent inside

The galvanostatic charge-discharge of the fabricated EDLCs is demonstrated in Fig. 40. The EDLCs which contained polymerized MXCs/PANBA and physical mixed MXC1+PANBA as binder can be charge and discharge at $I = 1.54$ mA whereas the EDLCs only with PANBA and physical mixed MXC2+PANBA as binder cannot come through. Besides, the EDLCs with polymerized MXC1/PANBA and MXC2/PANBA binder exhibit a distinguished first discharge capacitance as 75.83 F/g and 70.59 F/g. Meanwhile, MX1+PANBA shows 31.20 F/g which even not enough half of the EDLCs with polymerized MXs/PANBA as binder. The capacitance retention of MXC1/PANBA, MXC2/PANBA and MXC1+PANBA are 72.0 %, 64.9 % and 51.4 %, respectively. These are indicated that polymerized MXCs/PANBA can afford a more effective pathway for electrons while they applied as binder for EDLCs.

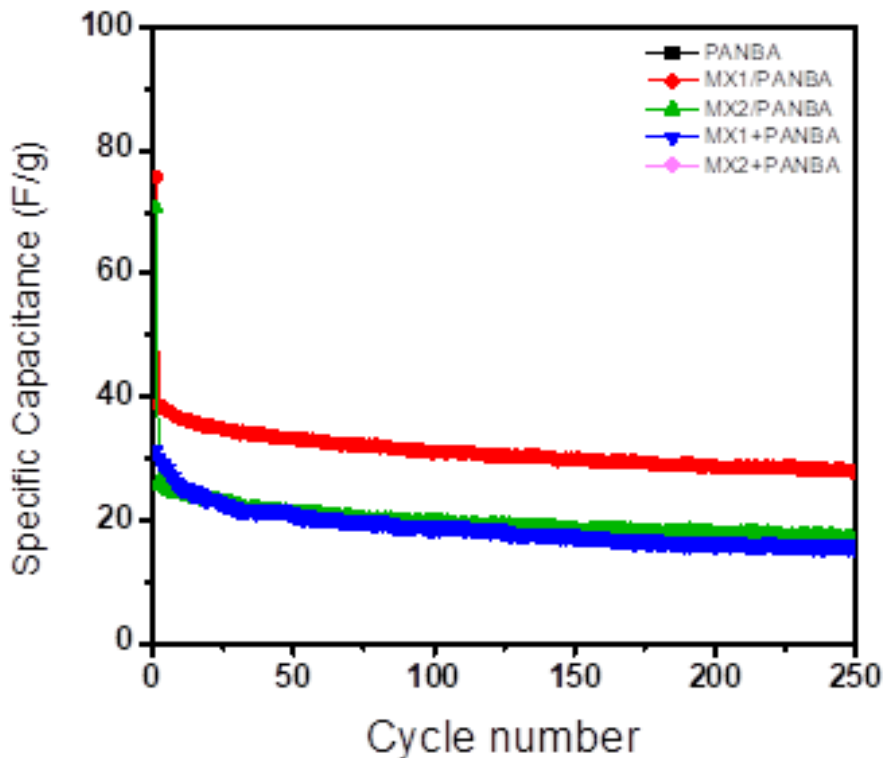


Figure 40: Cycling performance of none conducting agent symmetrical EDLCs.

4.3.2.2 IMP performance of EDLCs without conducting agent inside

The impedance test of none conducting agent EDLCs were recorded after galvanostatic cycling as shown in Fig. 41. Their data have been fitted, and the X-intercept which stand for charge transfer resistance have been displayed as Table. 9. The impedance shows a semicircle due to presence of both resistive and capacitive element in parallel. The equivalent circuit is shown in the inset of Fig. 41. However, the diffusion region cannot get from none conducting agent EDLCs at low frequency. It may indicate that the charge transfer resistances are too large to flow current. Therefore, we cannot get the information at low frequency. After fitting as equivalent circuit, the EDLCs charge transfer resistance has been calculated. The polymerized MXCs/PANBA show around 3 times smaller charge transfer resistance than original PANBA. So, the polymerized MXCs/PANBA reveal their potential to use as binder for symmetrical EDLCs.

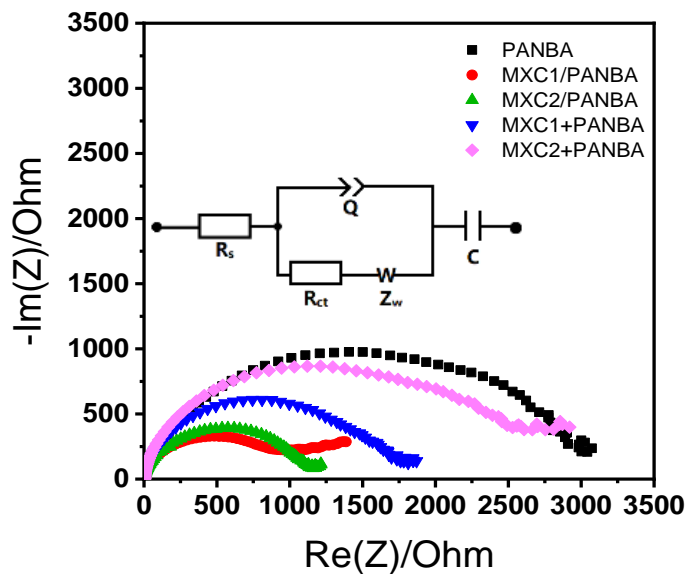


Figure 41: IMP profile of none conducting agent symmetrical EDLC after charge/discharge 250 cycles and fitting with equivalent circuit insert.

	PANBA	MXC1/PANBA	MXC2/PANBA	MXC1+PANBA	MXC2+PANBA
Charge transfer resistance	3076.2±76.8 Ω	978.4±34.1 Ω	1100.8±38.9 Ω	1549.3±148.0Ω	2386.1±356.1 Ω

Table 8: X-intercept of none conducting agent symmetrical EDLCs by IMP profile data fitting after charge/discharge 250 cycles.

4.3.2.3 Cycling performance of EDLCs with conducting agent inside

Prolonged galvanostatic cycling at 2.6 mA cm^{-2} of the EDLC electrodes with different binders is shown in Fig. 42. The initial capacitance of the EDLC-M0 was 120 F g^{-1} , whereas an increase in electrode capacitance was observed for MXC-containing electrodes. The EDLC-M1 and EDLC-M2 showed an initial capacitance of 129.8 F g^{-1} and 128.4 F g^{-1} , respectively. All electrodes show stable cycling performance for 10,000 cycles with specific capacitance retention over 90 % for each electrode with slight differences. The higher specific capacitance of EDLC-M1 and EDLC-M2 as compared to EDLC-M0 is attributable to the improved electronic conduction in the MXC/PANBA binder. Though commercial SP is a good conducting agent, it exhibits the conductivity by the point-to-point mechanism with active materials[80], that leaves void spaces in the electrodes. The use of large lateral size of MXC helps reduce these void spaces and make the EDLCs more active in a given electrical field.

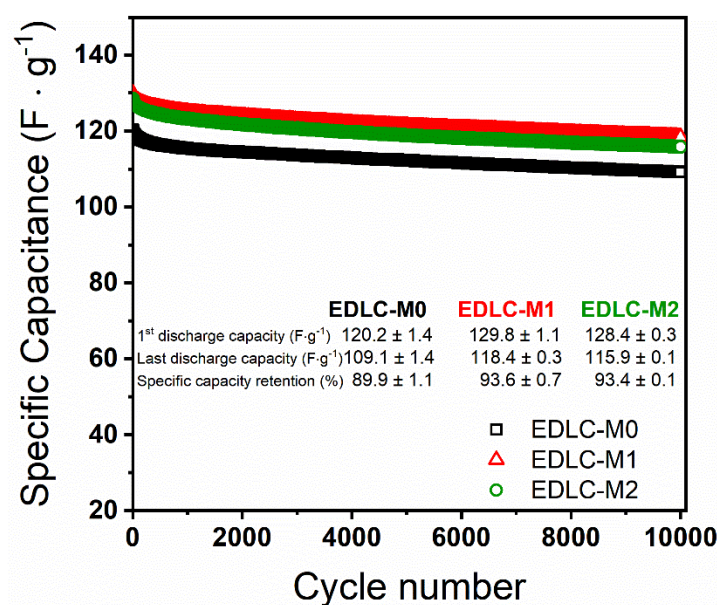


Figure 42: EDLCs cycling performance with different binder for 10,000 cycles and charge/discharge schematic demonstration.

4.3.2.4 IMP performance of EDLCs with conducting agent inside

Fig. 43 shows typical experimental Nyquist plots of the carbon-based EDLC cells obtained by performing EIS after 10,000 charge-discharge cycles. These consist of a semicircle at high-middle frequency ranges, a short low-slope line at the middle-low frequencies, and a relatively long high-slope line at the low frequencies, although there is not a clearly distinguishable boundary between the two slopes. As shown in Fig. 6(a), three resistance are evaluated: bulk electrolyte resistance (R_s – high frequency region), charge transfer resistance (R_{ct} – medium to high frequency region), and diffuse layer resistance (R_{dl} – low frequency region) [81]–[83]. Since there is no actual “charge transfer” occurring in EDLC, the R_{ct} is represented as a combination of three resistances: the electrolyte resistance in the pores of the electrode, the electrode resistance, and the contact resistance between the electrode and Al current collector. R_{dl} is assigned to ion transport limitation through nonuniform pathways from the bulk to the surface of the porous electrode [84]–[86]. Table 3 lists the resistances of the EDLC cells. The EDLC-M1 and EDLC-M2 cells showed lower internal resistances as compared to the EDLC-M0. This can be attributed to the enhanced electron transfer in the electrode due to MXC (shown in Fig. 3 and Table 2) which facilitates the charge-complexes in the electrolyte to migrate in the pores as a response to the frequent change in the given voltage[87]–[89]. In addition, the lower R_{dl} of the EDLC-M1 and EDLC-M2 cells indicate that addition of MXC leads to faster diffusion of the electrolyte ions. These advantages of the MXC/PANBA binder contributes to the improved cycling performance of the EDLC cells

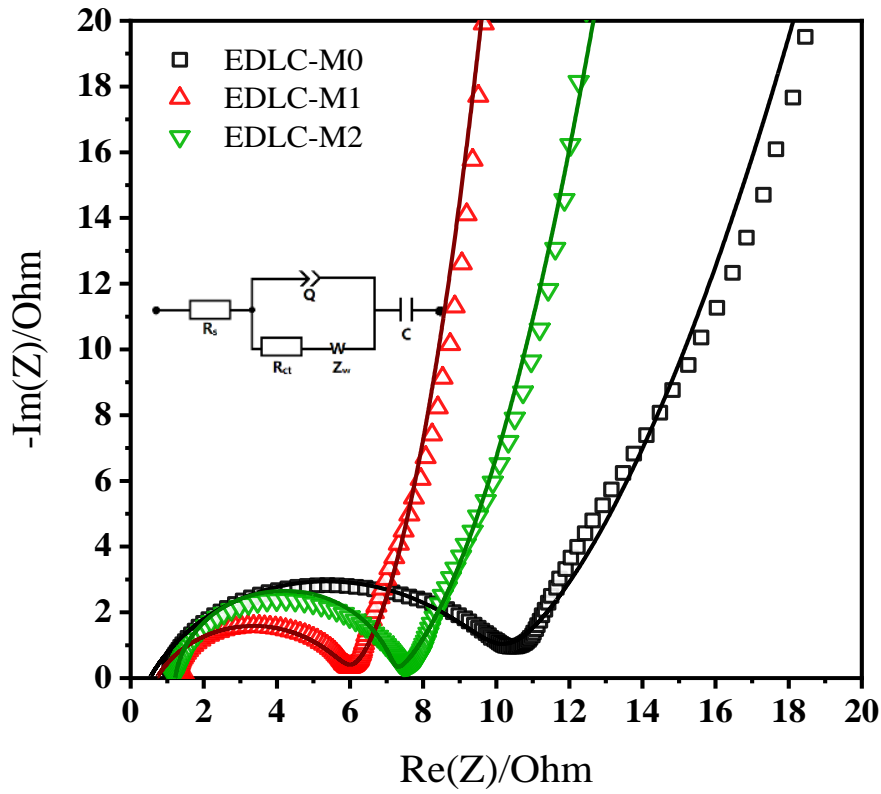


Figure 43: Nyquist plot of EDLCs with the frequency from 10^6 Hz to 10^{-2} Hz at $E = 0$ V after 10,000 cycles, and fitting with equivalent circuit insert.

	<i>EDLC-M0</i>	<i>EDLC-M1</i>	<i>EDLC-M2</i>
R_s (Ω)	0.52	0.71	1.22
R_{ct} (Ω)	9.49	5.24	5.93
A ($\Omega \cdot s^{1/2}$)	3.63	1.53	2.10
α	0.69	0.70	0.93

Table 9: EDLCs charge transfer resistance.

EDLCs charge transfer resistance, Warburg coefficient and a constant phase element exponent calculate by EIS data equivalent electrical circuits fitting.

4.3.2.5 EDLCs charge discharge profile

The charge-discharge profile of EDLCs is shown in Fig. 44. After charging/discharging for 10,000 cycles, the EDLCs have been charged at constant current mode from open circuit voltage to 2.7 V. The constant current discharge mode followed at once until voltage goes back to 0.1 V. The voltage values have been recorded at each second. The charge and discharge voltage are almost linear with time and exhibit a symmetric triangular shape which is consistent to that reported in literature for a typical EDLC [90]. Additionally, there is an IR drop which indicating the EDLCs equivalent series resistance (ESR) when the current was reversed immediately. For comparing the ESR differences via alternating current (AC) method EIS and direct current (DC) method galvanostatic charge-discharge (GCD), the ESR calculated by charging/discharging have been taking palce as follows. Comparing with ESR measured by EIS, GCD can give more information based on operating conditions, particularly [91]. The ESR values are as shown Table. 11. The ESR per gram of active material have been taken accounted as well. The equivalent series resistivity of MXCs/PANBA EDLCs are smaller than PANBA EDLCs when they used at DC mode.

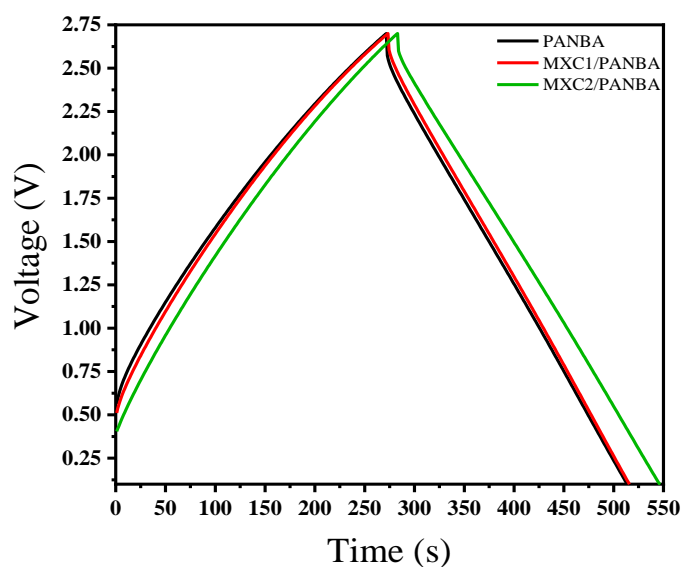


Figure 44: EDLCs charge/discharge profile at $I = 1.54 \text{ mA}$ between $0.1 - 2.7 \text{ V}$.

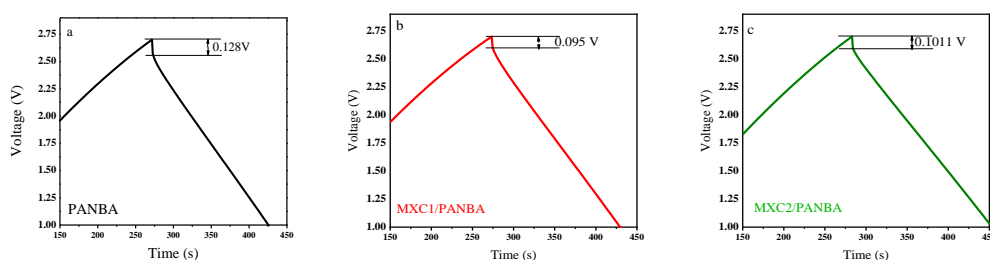


Figure 45: Enlarged EDLCs charge/discharge profile for IR drop calculation.

	<i>EDLC-M0</i>	<i>EDLC-M1</i>	<i>EDLC-M2</i>
$V=IR \text{ (v)}$	0.128	0.095	0.1011
$R=V/2I \text{ (}\Omega\text{)}$	16	11.93	12.64
$R/m \text{ (}\Omega\text{/mg)}$	2.16	1.73	1.69
$\rho = RA/l \text{ (}\Omega\text{-m)}$	23.04	17.25	16.7

Table 10: EDLCs equivalent series resistance (ESR) calculation via its enlarged charge/discharge profile.

4.3.2.6 EDLCs CV profile

Each EDCL sample after charging/discharging for 10,000 cycles have been linear sweep voltammetry scanned from 0 V to 3 V at $5 \text{ mV} \cdot \text{s}^{-1}$, $20 \text{ mV} \cdot \text{s}^{-1}$, $50 \text{ mV} \cdot \text{s}^{-1}$, $100 \text{ mV} \cdot \text{s}^{-1}$ as shown as Fig.46 (a). Absence of redox peaks in CV plot implies that electrodes demonstrated electrical double layer character. Due to $dQ = I \cdot dt$ and $C = dQ / dV$, the current response by voltage change at a constant capacitance. The cyclic voltammograms can hold a nearly rectangular shape at small scan rate. However, they lost their rectangular shape by increasing scan rate, since there are inter resistance that influence the current responses. The cyclic voltammograms of each EDLCs at $100 \text{ mV} \cdot \text{s}^{-1}$ have been compared as Fig. 46 (b). The PANBA curve which caused by inter resistance when voltage went back to 0 V become larger than MXs/PANBA. In MXs/PANBA samples, the current become stable at $5 \text{ A} \cdot \text{g}^{-1}$ when voltage drop to 0.55 V where as PANBA samples never hold its current. The CE have also been calculated by CV as Table. 12. The MXs/PANBA have a higher CE. It is implying that MXs/PANBA binder improve charge reversibility over than 95 %. The trend of CE is consistent with CE calculated by cycling results.

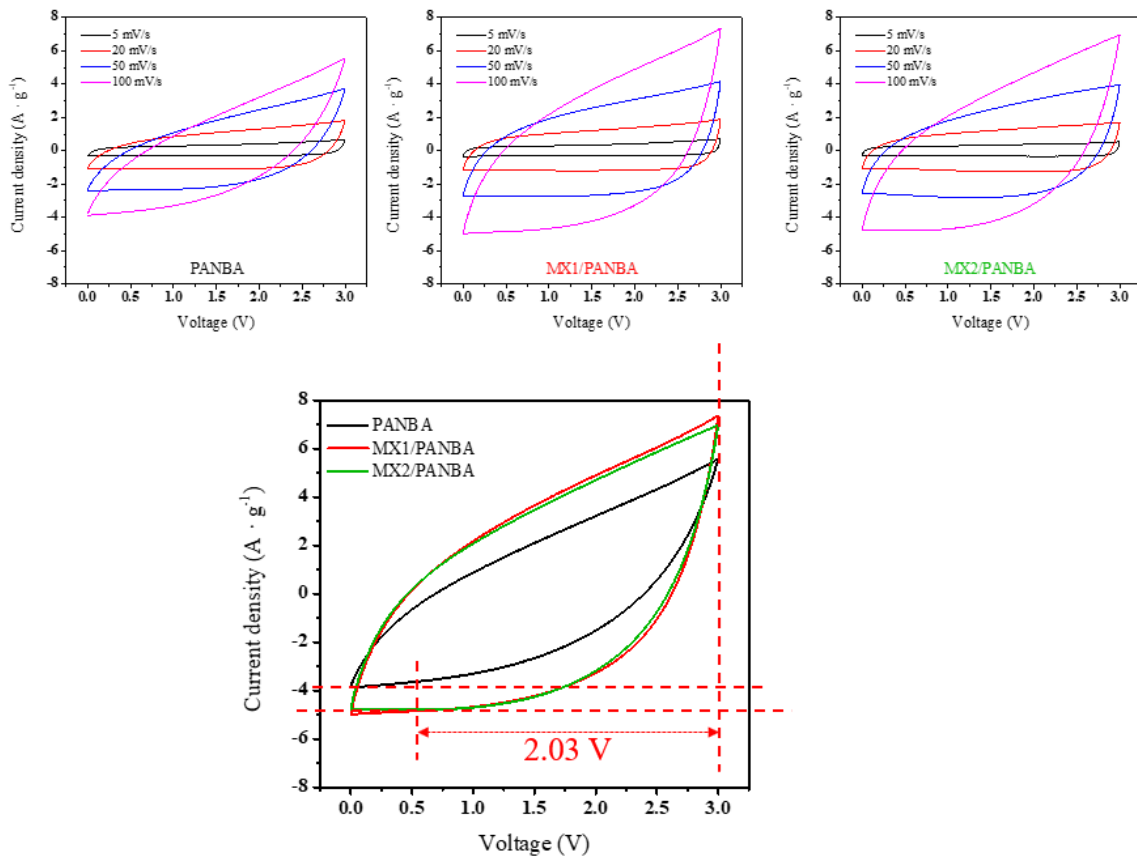


Figure 46: Cyclic voltammetry of EDLCs.

(a) Cyclic voltammetry (CV) of the EDLCs at various scan rates, $5 \text{ mV} \cdot \text{s}^{-1}$, $20 \text{ mV} \cdot \text{s}^{-1}$, $50 \text{ mV} \cdot \text{s}^{-1}$, $100 \text{ mV} \cdot \text{s}^{-1}$; (b) CV of EDLCs at $100 \text{ mV} \cdot \text{s}^{-1}$.

	PANBA	MX1/PANBA	MX2/PANBA
CE	94.33%	98.97%	95.57%

Table 11: EDLCs coulombic efficiency (CE) calculated by cyclic voltammogram.

4.3.2.7 High-rate performance of EDLCs with conducting agent inside

Galvanostatic charge-discharge at different current densities of $0.5 \text{ mA} \cdot \text{cm}^{-2}$, $1.0 \text{ mA} \cdot \text{cm}^{-2}$, $5.0 \text{ mA} \cdot \text{cm}^{-2}$, $10 \text{ mA} \cdot \text{cm}^{-2}$, $50 \text{ mA} \cdot \text{cm}^{-2}$ was carried out for EDLCs with PANBA, MXCs/PANBA binder. As seen in Fig. 47(a), the general trend of specific capacitance of rate capability test agrees with the results of cycling performance at current density under $50 \text{ mA} \cdot \text{cm}^{-2}$. The specific capacitance of PANBA dropped to a very low value when the current density of $50 \text{ mA} \cdot \text{cm}^{-2}$ was applied. However, MXC1/PANBA and MXC2/PANBA retained a capacitance of 68% (with respect to to initial capacitance value) at $50 \text{ mA} \cdot \text{cm}^{-2}$. In addition, they retained almost 97 % of their capacitance when the current density was brought back to $0.5 \text{ mA} \cdot \text{cm}^{-2}$. It proved that they can maintain a stable capacitance even after charging and discharging at high current density.

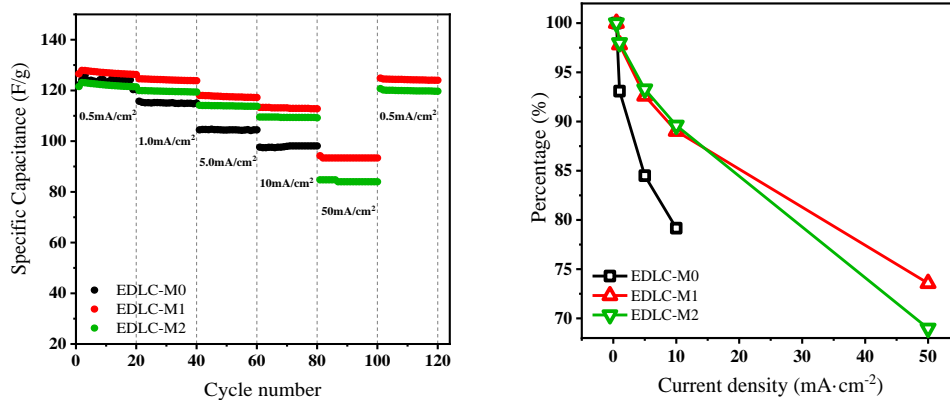


Figure 47: EDLCs rate capability performance.

- (a) EDLCs rate capability performance with different binder for 20 cycles at each current; (b) Capacitance retention at diverse current density.

4.3.2.8 Ragone plot of EDLCs

We then compared the performance our EDLCs with those reported in literature via a Ragone plot (Fig. 8 and Table S2). The shadowed area in Fig. 8 indicates the specific energy against the specific power region occupied by typical electrochemical capacitors, which was reviewed by Simon and Gogotsi[92]. Our EDLCs show substantially higher specific energies and power than typical EDLCs, and the specific power increases while maintaining relatively high energy densities. Further, they are even better than the results obtained in recent studies[23], [91], [93]–[96]. In particular, the EDLC-M1 cell showed specific energy of 23.6 Wh kg^{-1} at very high specific power of 8510 W kg^{-1} and the EDLC-M2 cell showed specific energy of 21.3 Wh kg^{-1} at a specific power of 6396 W kg^{-1} . By contrast, the EDLC-M0 retained a specific energy of 23 Wh kg^{-1} at a very low specific power of 1472.6 W kg^{-1} . Consequently, the use of MXC in the binder significantly enhances the high-power performance of the EDLCs, even though a tiny amount of MXC is used in comparison to other component electrode materials.

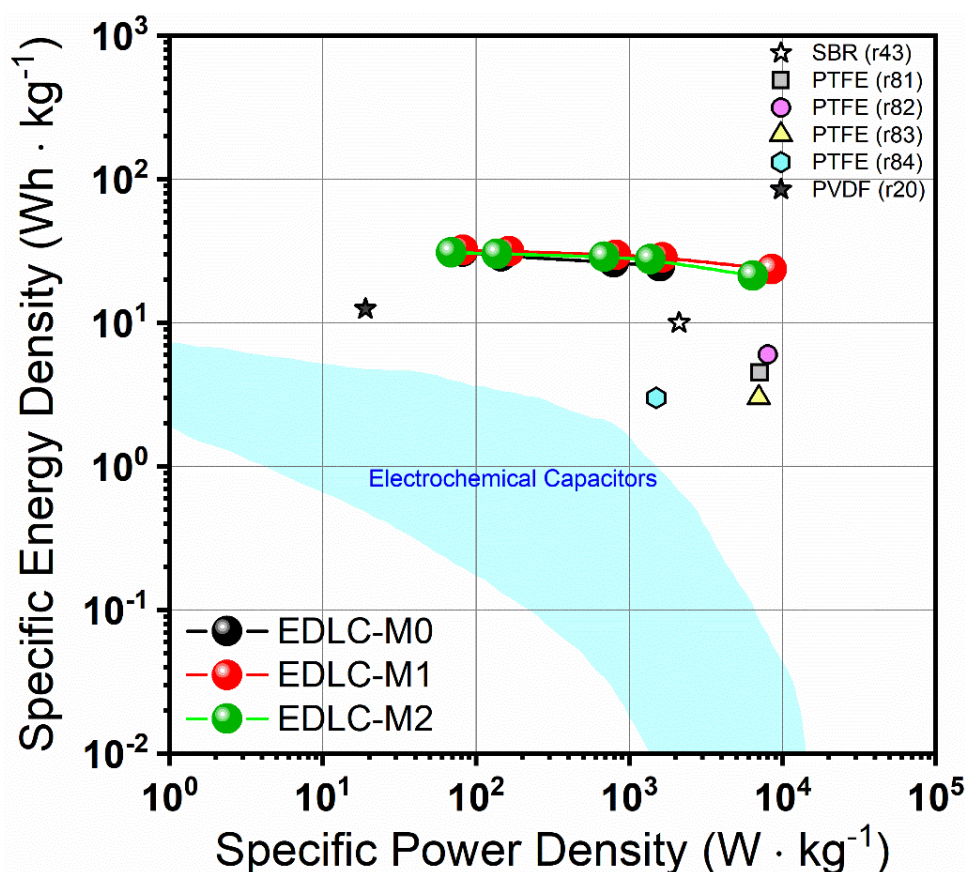


Figure 48: The ragone plot of EDLCs.

4.4 MXENE/ CORE SHELL STRUCTURED POLY (STYRENE-ACRYLONITRILE-BUTYL ACRYLATE)

4.4.1 Physical properties

4.4.1.1 Raman and FTIR

For confirm the typical peaks of polystyrene, polyacrylonitrile and poly butylacrylate, the Raman and FTIR of binder film has been conducted and showed in Fig. 49. The typical peak of MXene at Raman shift 200 cm^{-1} can be found clearly in Raman (Fig. 49 left). The function group of styrene benzene peak can also be seen at Raman shift 1000 cm^{-1} . The typical peak of C=O of poly butylacrylate and the typical peak of C \equiv N of poly acrylonitrile can be found both in Raman and FTIR. Besides, the inter molecular hydrogen bond of MXs/CS implying the core shell polymer particles attached on MXene sheets surface. In summary, the core shell structured poly (styrene-acrylonitrile-butyl acrylate) has been synthesized successfully and the intermolecular hydrogen bonds formed between polymer particles and MXene sheets.

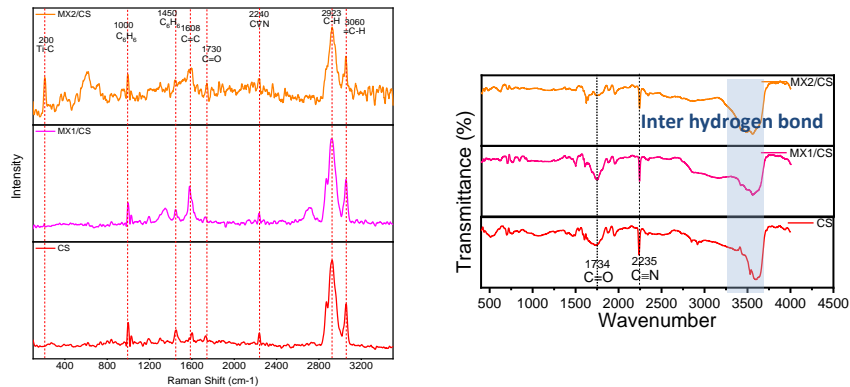


Figure 49: The Raman spectra (left) and FTIR (right) of polymer film.

4.4.1.2 SEM

After polymerization, the polymer solution has been dried in conventional oven for 24h at 60°C to form binder film and as shown in Fig. 50(a). The binder film can keep its integrity even after peeling off from aluminum dishes which implying core-shell structured polymer possess a strong mechanical strength. Furthermore, the SEM and TEM of core-shell structure can be seen clearly at Fig. 50(b,c,d). The polymer particles can be found at the surface of MXene (Fig. 50 e). This is agreed with the FTIR and Raman results that mentioned above. However, some of polymer particles covered the MXene sheets which indicating a good flexibility of core-shell structured polymer.

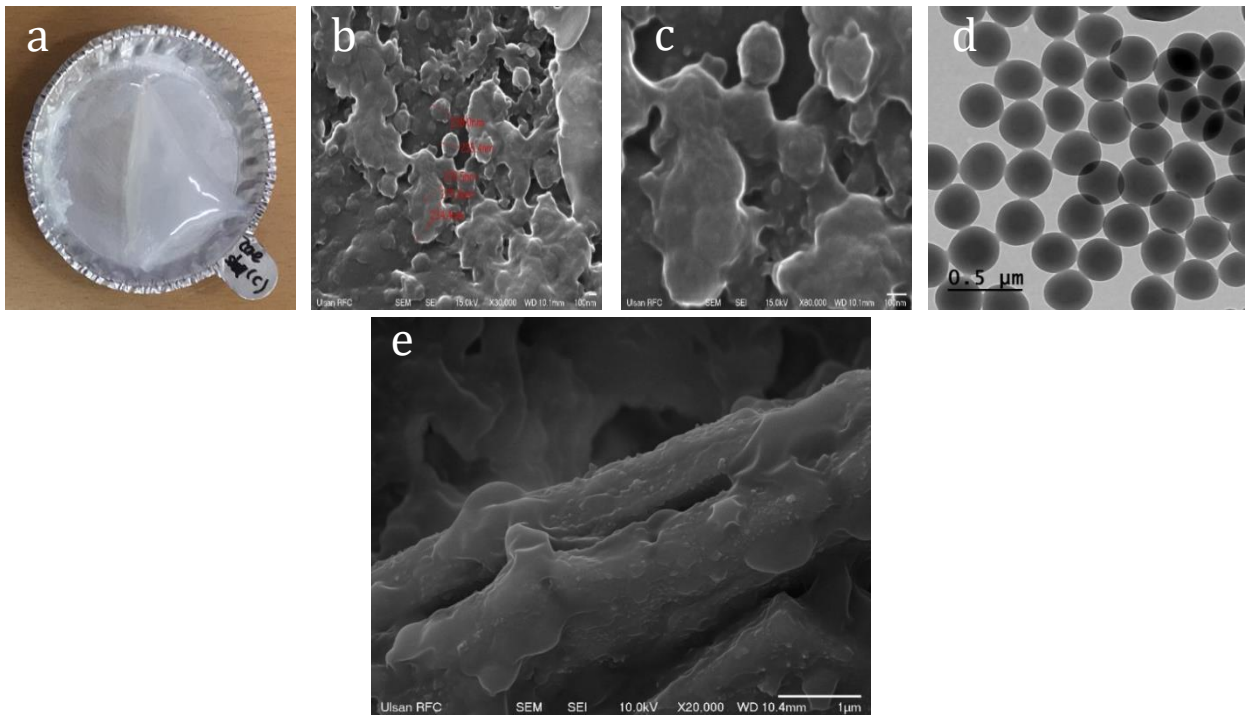


Figure 50: (a) Polymer after dry (b,c) SEM image of polymer (d) TEM image of polymer € SEM image of MX/CS.

4.4.1.3 Contact angle

For investigating the compatibility of binder film to electrolyte. The contact angle of polymer binder film has been conducted while electrolyte droplet fell onto the binder films for 60 s and shown as Fig. 51. As time goes by, the contact angle of all binder films decreased, so the contact angle change during the 60s has been calculated and displayed in Table 12. The core-shell structured binder film has the largest contact angle change comparing with others. This is due to the core of core-shell structured binder is normally used as poly electrolyte for lithium ion battery and supercapacitor, so the affinity of core of core-shell structured binder is better than SBR. However, at the present of MXene sheets the MXs/CS binder film declined the affinity of electrolyte a little but still bigger than SBR binder film. The contact angle change can evaluate the binder film's affinity to electrolyte. a good compatibility of binder film to electrolyte can increase the ion conductivity of binder while applied on lithium ion battery or supercapacitor, so that the better rate performance can be achieved.

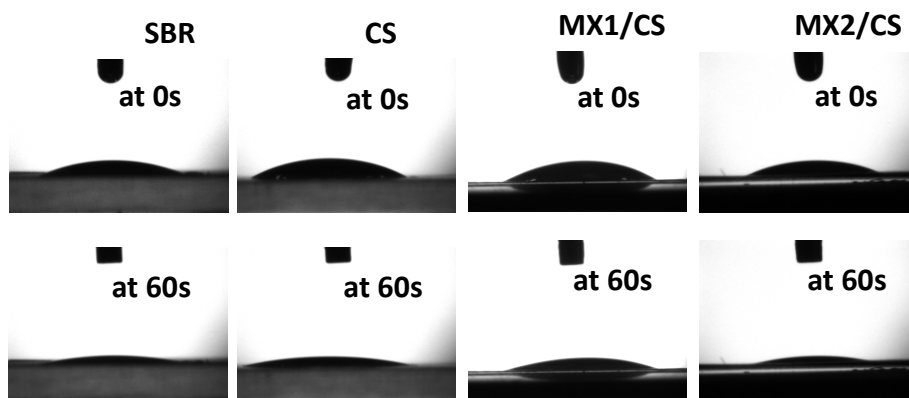
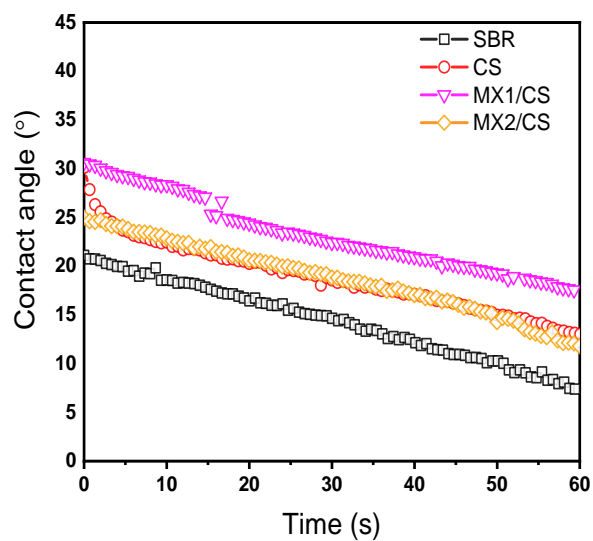


Figure 51: Contact angle of an electrolyte droplet fell onto the binder films during the 60 s.

Table 12: Contact angle change of an electrolyte droplet fell onto the binder films during the 60 s.

Contact angle change during 60s	
SBR	$20.11^{\circ} - 8.39^{\circ} = 11.72^{\circ}$
CS	$30.14^{\circ} - 13.12^{\circ} = 17.02^{\circ}$
MX1/CS	$30.63^{\circ} - 17.55^{\circ} = 13.08^{\circ}$
MX2/CS	$24.98^{\circ} - 11.79^{\circ} = 13.19^{\circ}$

4.4.1.4 Thermal property of binder film

Generally, all the components of energy storage device should be thermal stable in a wide range. This is due to the temperature may change during charge and discharge progresses. A good thermal property of binder can reduce the energy storage device suffer from serious risk issues. Therefore, the TGA of dried binder film has been conducted and shown as Fig. 52. All the binder can be thermal stable up to 350°C. as temperature over than 400°C, the binder film thermal decomposition starts rapidly. In addition, the thermal stability doesn't have obvious change at the present of MXene which indicating that the core-shell structured binder and MXs/CS binder have as good thermal stability as SBR possess. The CS and MXs/CS binder are qualified to applied in energy storage device for additional tests. The DSC also shows that CS series binder are flexible enough to hold its integrity at room temperature. (Table. 13.)

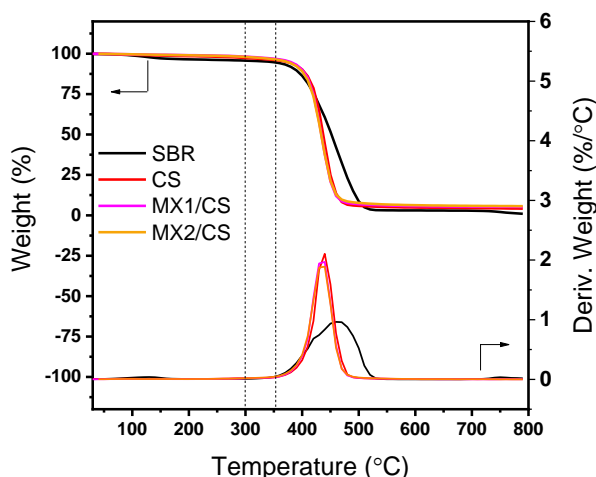


Figure 52: Thermogravimetry (TGA) of polymer film.

Table 13: Glass transition temperature of different polymer.

	SBR	CS	MX1/CS	MX2/CS
T_g (°C)	-11.25±0.02	12.44±0.08	13.69±0.05	12.76±0.07

4.4.1.5 Ion conductivity of binder solution and sheet resistance of binder film

Ion conductivity of binder solution is a crucial property for binder applying on energy storage devices, especially for energy storage devices charge and discharge at high current density. From Figure. 53, the ion conductivity of CS and MXs/CS have been compared with SBR and they all have a higher ion conductivity than SBR which implying a better rate performance they will have than SBR while applied on energy storage devices. The MXs/CS has higher ion conductivity property may due to the metallic characters of MXene sheets or function groups on MXene surface. Besides, the dired binder film sheet electronic conductivity has been studied as listed in Table. 14. Due to the good electronic conductivity of MXene sheets. The MXs/CS has a significantly lower sheet resistance than CS and SBR which can deliver electrons faster while charging and discharging processes and resulting in a better rate performance.

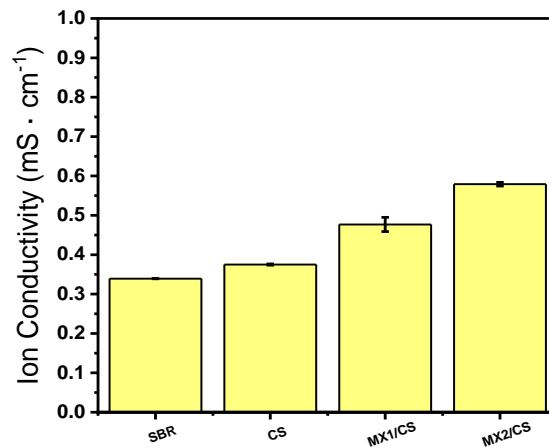


Figure 53: Ion conductivity of polymer solution.

Table 14: Sheet resistance of different polymer.

	SBR	CS	MX1/CS	MX2/CS
R (Ω/sq)	64.48±6.01	60.40±1.11	35.91±1.21	46.96±1.27

4.4.1.6 CV of binder film

One of the most important property of polymer used as binder for energy storage system is the electrochemical stability. It is due to the binder is a polymeric chemical addition, so it should be both electrochemical stable in anodic and cathodic environment in the operating voltage range. Therefore, the CV of only binder film coating on etching Al-foil at different scan rate have been investigated in half coin cells and shown as Fig. 54. All binder film do not have any obvious chemical reaction peaks which indicating the electrochemical stability in the voltage range 0.0-3.0 V. we can conclude that CS and MXs/CS polymer can be used as binder while the operating voltage range 0.0-3.0 V.

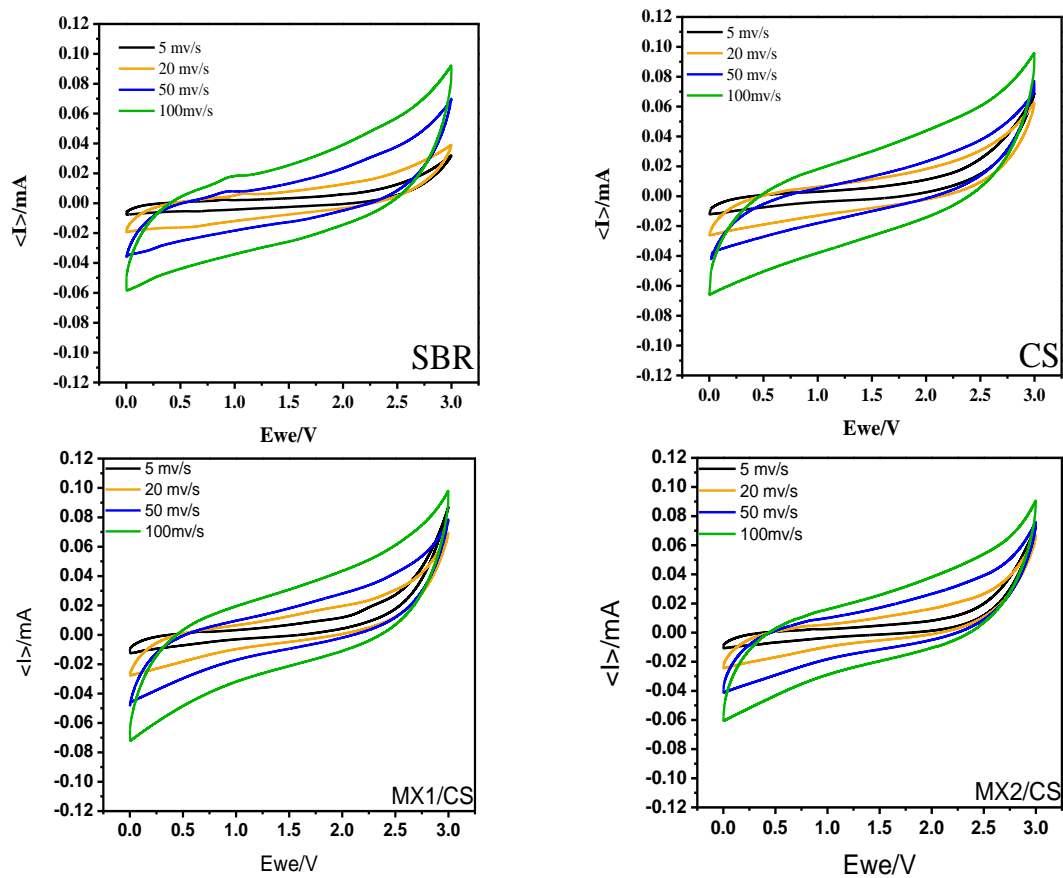


Figure 54: Cyclic voltammetry (CV) of binder film coating on e-Al foil.

4.4.1.7 Electrode adhesive property

In general, the function of binder in an energy storage device is to keep the integrity of electrode, so majority of researchers devote to improve adhesive strength of binder. So, in this study, the adhesive property of electrode has been conducted by peeling test in 180° in a speed 60 mm/min and the results with error bars shown as Fig. 55. Comparing the SBR, CS binder shows half adhesive strength (80 gf/cm). the addition of MXene slightly decreased the adhesive strength of CS binder. This is due to the MXene sheets are metallic material with low adhesive property. For this reason, the higher ratio of MXene sheets did not studied here.

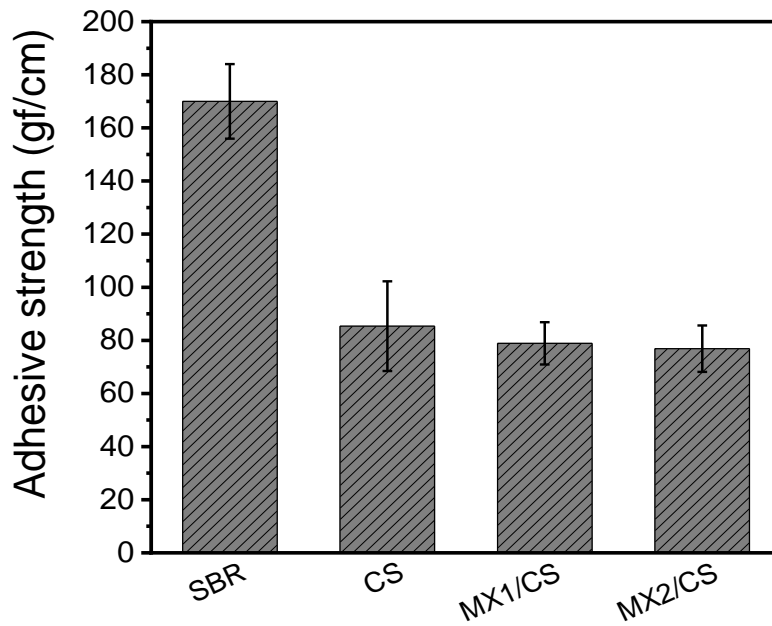


Figure 55: The adhesion strength value of electrodes of different binder with an error bar.

4.4.1.8 BET

Before electrochemical tests of electrode with different binder system, the BET of electrodes has conducted for investigating the surface area of electrode particles which is an important characteristic for EDLCs. The nitrogen adsorption and desorption isotherms curves shown as Fig. 56, and the porosity information of EDLCs electrodes are displayed in Table. 15. The surface area of CS is about $1200 \text{ m}^2 \text{ g}^{-1}$, and at the present of MXene, the BET surface area decreased a little bit. This is probably due to the large sheets size of MXene, it is around $7 \text{ }\mu\text{m}$. Besides, the declined total pore volume of MXs/CS also indicating partial of pores have been blocked by MXene sheets. However, this blocking effect can be usually found in binder system, and the blocking effect is acceptable for EDLCs tests.

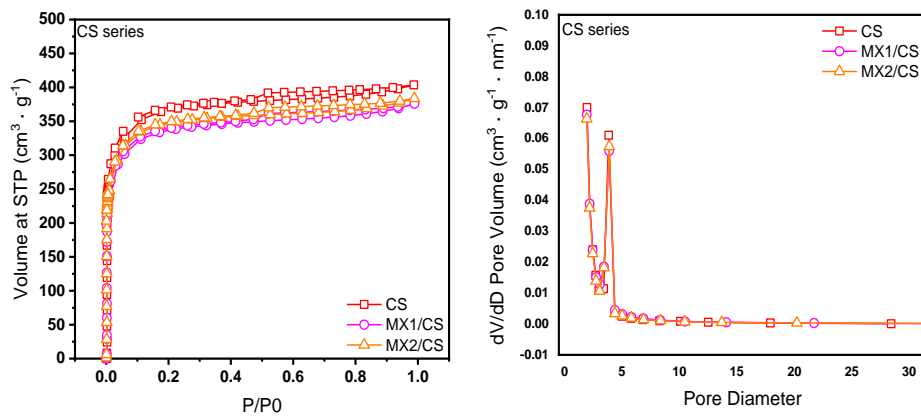


Figure 56: (up) Nitrogen adsorption/desorption isotherms curves of supercapacitor electrodes excluding current collectors; (down) Electrodes pore diameter distribution based on the BJH method.

Table 15: Porosity information of EDLCs electrodes with different binder.

	S_{BET} ($\text{m}^2 \text{ g}^{-1}$)	S_{micro} ($\text{m}^2 \text{ g}^{-1}$)	S_{meso} ($\text{m}^2 \text{ g}^{-1}$)	$V_{\text{total pore}}$ ($\text{cm}^3 \text{ g}^{-1}$)	$V_{\text{micropore}}$ ($\text{cm}^3 \text{ g}^{-1}$)	Pore width aver (nm)
CS	1206.95	929.25	277.70	0.62	0.44	2.07
MX1/CS	1166.47	909.69	256.77	0.58	0.41	1.99
MX2/CS	1162.44	914.59	247.85	0.59	0.43	2.04

4.4.2 Electrochemical properties

4.4.2.1 CV

The CV of EDLCs have been conducted in a voltage range 0.0-3.0 V at various scan rate and shown as Fig. 57. All groups show a typical shape of supercapacitor that without any obvious peaks in operating voltage range which indicating there isn't any chemical reaction happened in EDLCs with different binder. As increasing scan rate, the response current gets higher. And the rectangular shape of CV curve shows that the reduction and oxidation scan are repeatable and reversible. All the properties mentioned above imply a good cycling performance with good columbic efficiency can be obtained with CS and MXs/CX binder.

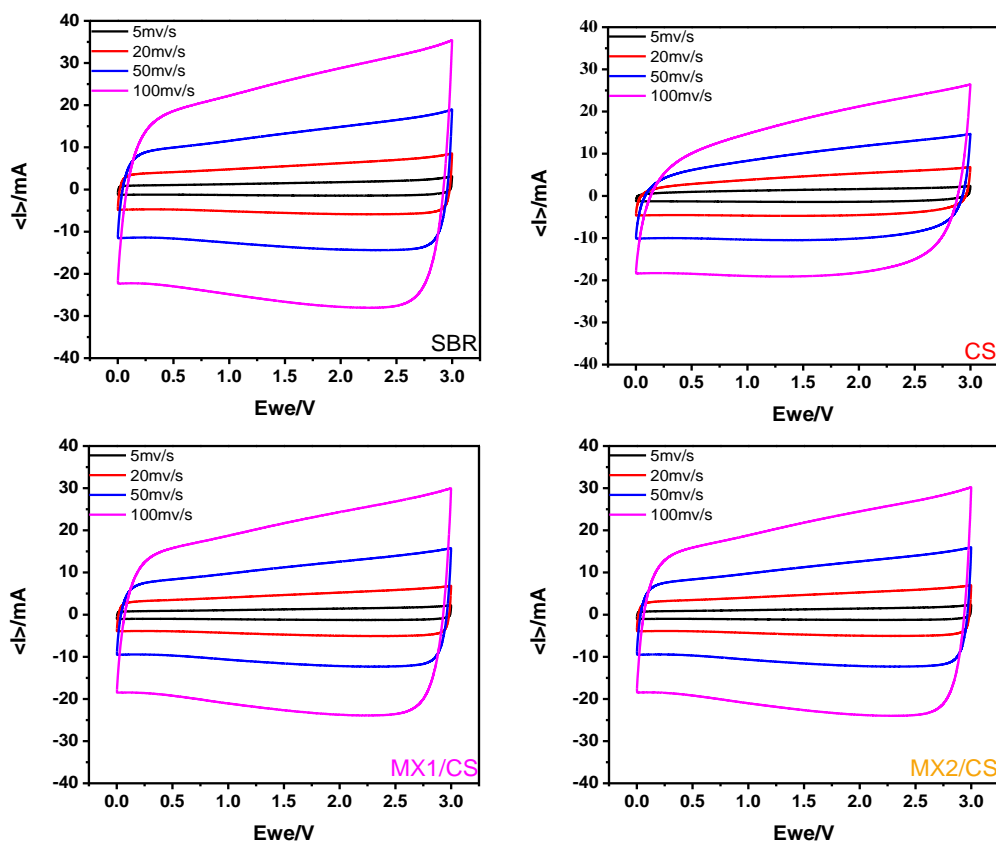


Figure 57: Cyclic voltammety (CV) of EDLCs.

4.4.2.2 IMP

The impedance of EDLCs with different binder have been studied in a frequency range 10^{-2} - 10^6 Hz at a voltage 0 V and the Nyquist plot shows as Fig. 58. There is a small semicircle and a large semicircle at high frequency range and middle frequency range, respectively. This probably due to the structure of binder is core-shell, so there are two times electrons transmission in electrode. With the addition of high electronic conductive MXene, the charge transfer resistances have been significant decreased comparing with only core-shell (CS) structured binder in EDLCs. Moreover, at low frequency range, the MX1/CS and MX2/CS shows a much steeper slope than CS which indicating a faster ion diffusion. This probably due to the higher ion conductivity of MXs/CS that has been discussed before. Overall, the superior charge transfer property and ion diffusion property may lead to an advanced charge and discharge performance.

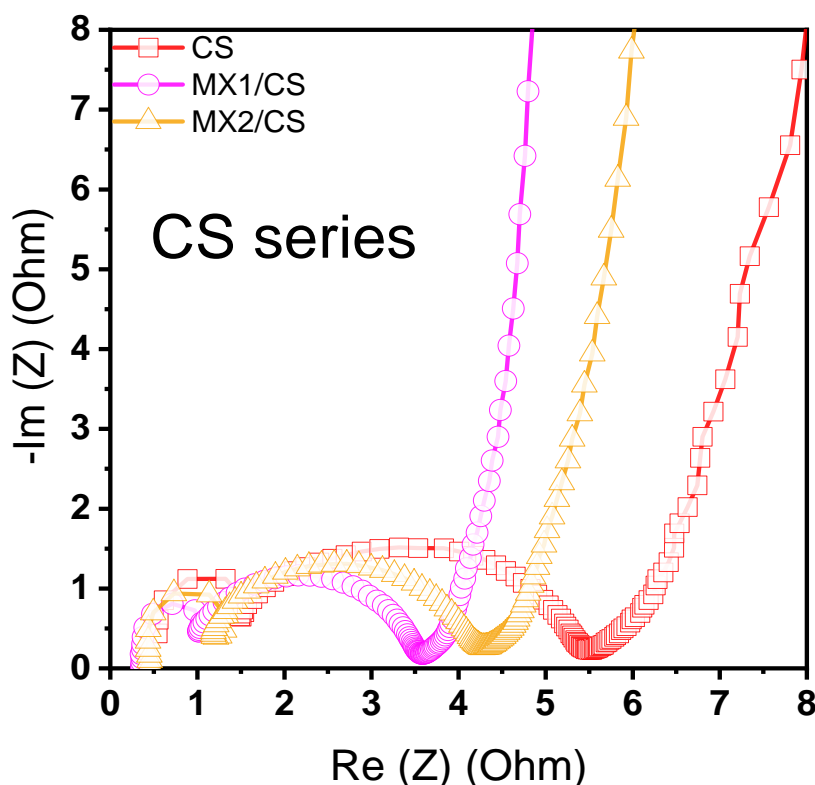


Figure 58: Nyquist plot of EDLCs with the frequency from 10^6 Hz to 10^{-2} Hz at $E = 0$ V after 10,000 cycles.

4.4.2.3 Cycling and high rate performance

For evaluating the charge and discharge performance, the cycling test at a voltage range 0.1-2.7 V has been conducted, and the EDLCs with different binder have been charge and discharge for 10,000 cycles. For comparison, the commercial water-based binder SBR has also been studied here, and the discharge capacitance of single electrodes have been shown as Fig. 59 (left). All of groups can be charge and discharge stably during 10,000 cycles. Both EDLCs with CS and MXs/CS as binder show higher discharge capacitance than commercial SBR. Furthermore, the rate performance of EDLCs also show a higher discharge capacitance at various current density (Fig. 59 right). This may contribute to the good mechanical strength of CS binder and the good electrical conductivity of MXs/CS binder. Moreover, the MXs/CS rate performance at current density 50 mA cm⁻² shows the highest discharge capacitance while that of EDLCs with CS shows the worst. This may contribute to the good electrical conductivity of MXene sheets, improved the MXs/CS binder conductivity, so that more electrons can be delivered fastly. Overall, we can conclude that MXs/CS can be qualified and used as binder for EDLCs at a voltage range 0.1-2.7 V. The electrochemical performance of MXs/CS is satisfactory while comparing with commercial SBR.

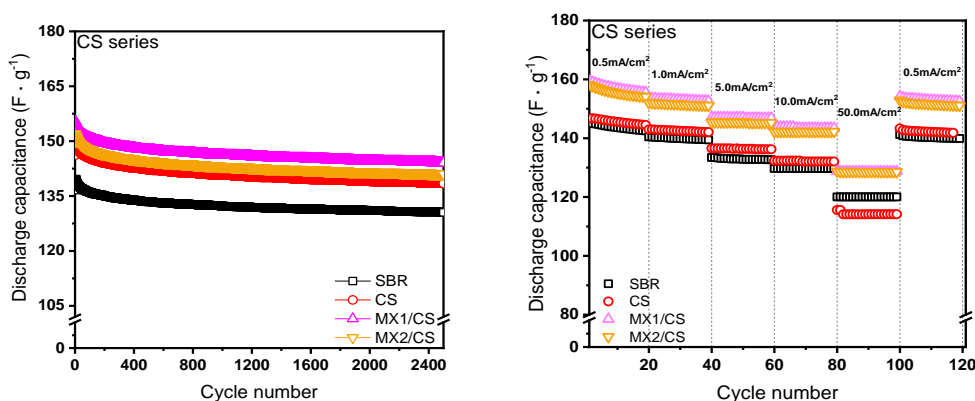


Figure 59: EDLCs cycling performance(left), high rate performance(right) with different binder.

4.5 MXENE/ HOLLOW CORE SHELL STRUCTURED POLY (STYRENE-ACRYLONITRILE-BUTYL ACRYLATE)

4.5.1 Physical properties

4.5.1.1 Raman and FTIR

First of all, the Raman and FTIR have been conducted to check the existence of poly styrene, polyacrylonitrile and poly butyl acrylate. In Raman spectra (Fig. 60), the Raman shift at around 1000 cm^{-1} and 1450 cm^{-1} are belong to the benzene ring of polystyrene. The Raman shift at 1730 cm^{-1} is belong to the C=O of poly butyl acrylate. The Raman shift at 2240 cm^{-1} is belong to the C \equiv N of polyacrylonitrile. All of the peaks above can be found in CS series and HCS series binder. Moreover, in MXs/CS and MXs/HCS samples we can be found typical peaks of MXene sheets at around 200 cm^{-1} . In a word, the polymerization of poly(styrene-acrylonitrile-butyl acrylate) has been synthesized successfully. We can find MXenes sheets exist in MXs/CS and MXs/HCS series samples. Besides, for futher check the inter molecular hydrogen bond between MXene sheets and polymer, the FTIR has been conducted as well, and the intensity of all samples have been shown in Fig. 61. We can be found that the strong peaks at wavenumber 3500 cm^{-1} are contribute to the inter molecular hydrogen bond between MXene sheets and polymer particles. Moreover, the COO- peaks can be found clearly in HCS series binder, which means the core polymer come out from core and dissolved in solutions. Overall, we can conclude that the inter reaction between MXene sheets and polymer, this kind of strong chemical connection may result in a superior electrochemical performance when applied them as binder in energy storage systems.

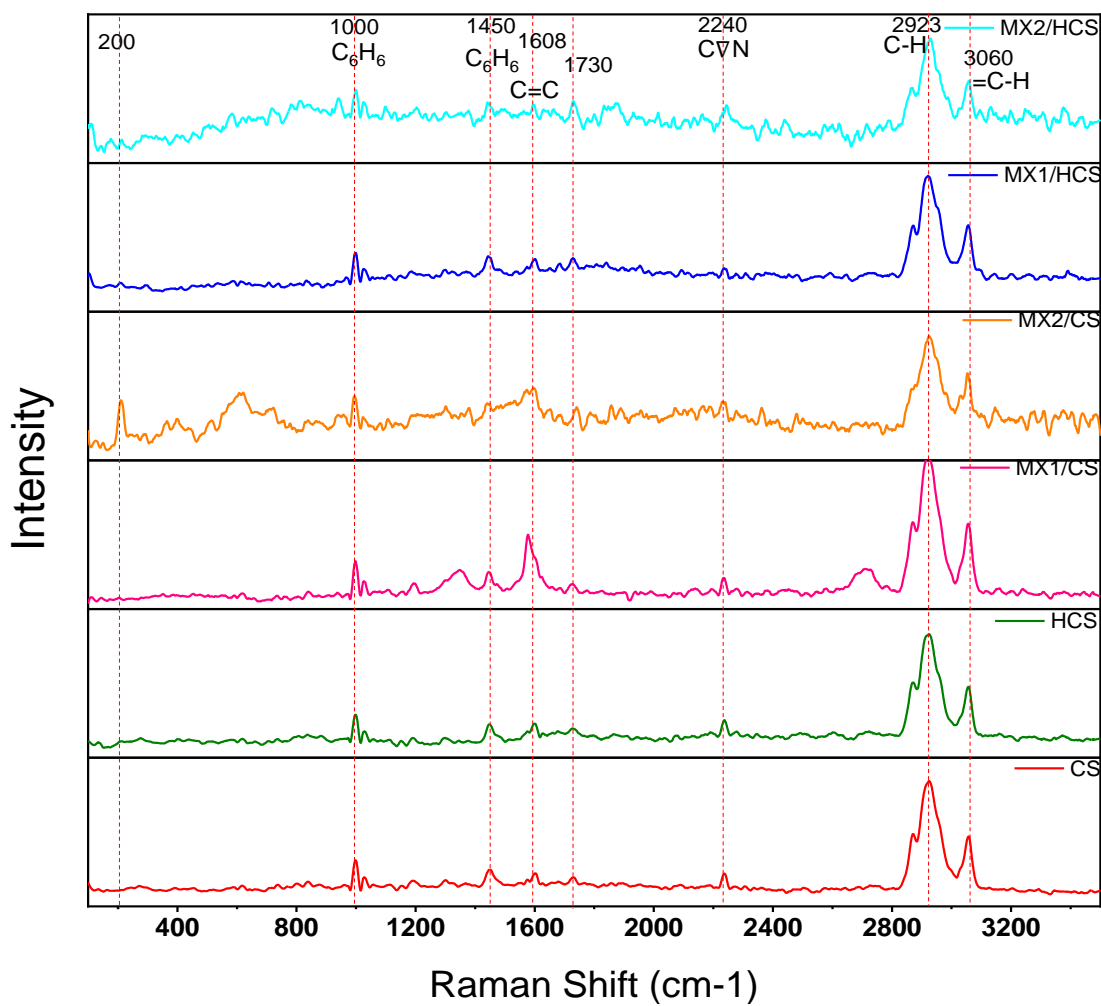


Figure 60: Raman spectra of polymer film.

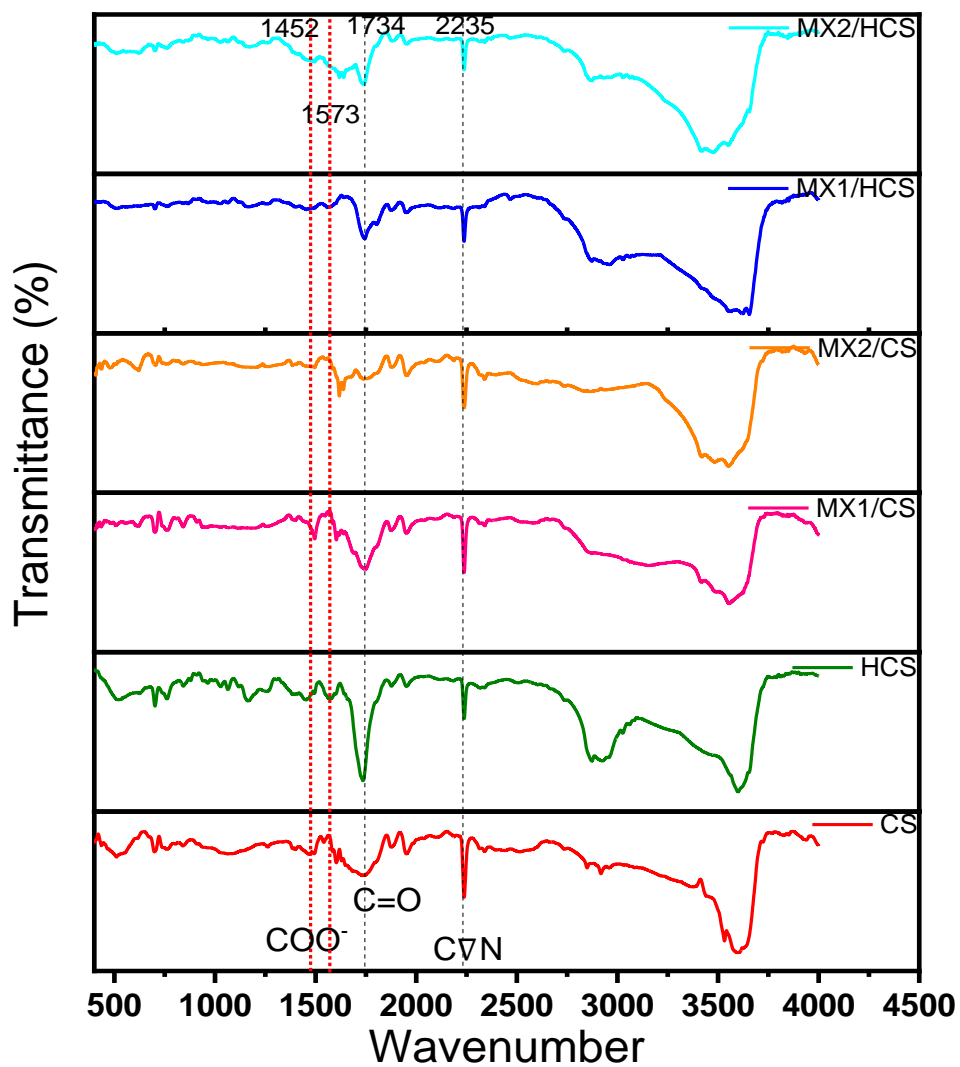


Figure 61: FT-IR spectra of polymer film.

4.5.1.2 SEM

After alkalization, the polymer has been dried in an aluminum dish and shown as Fig. 62 (a). It is clear that the alkalization destroyed the structure of polymer film, so that the mechanical strength of polymer film has been decreased significantly. Furthermore, in the SEM pictures of HCS polymer particles are shown as Fig. 62 (b-c). The HCS polymer particles are about 400 nm large, and they are very uniform. The small holes can be found on each polymer particle surface. They are the trace of core polymer coming out from core of core shell particles. This is agreeing with the TEM pictures of HCS particles that shown in Fig. 62 (d). The lighter color of polymer particles implying the empty space in HCS polymer particles. These empty spaces may later can be occupied with electrolyte when applied as binder in energy storage system. This kind of binder with electrolyte filled may lead a high ion conductivity and improve electrochemical performance.

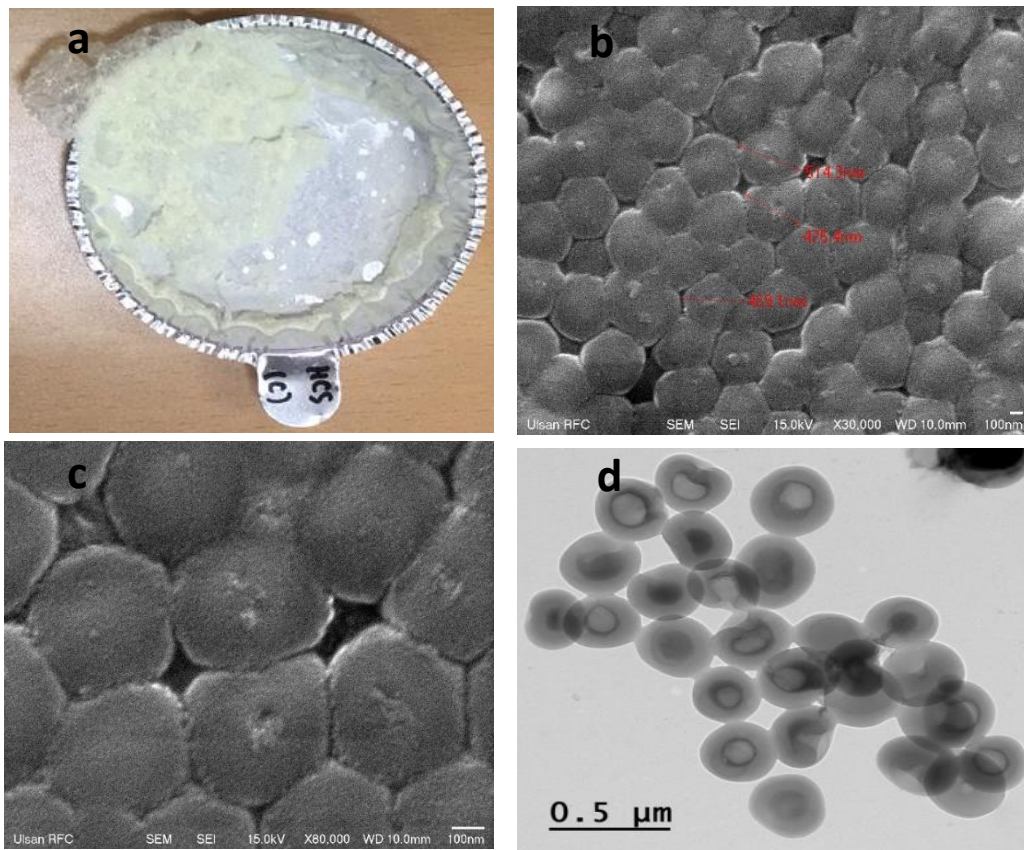


Figure 62: (a) Polymer after dry (b,c) SEM image of hollow core-shell polymer.

4.5.1.3 Contact angle

The contact angle has been recorded during 60s and shown in Fig. 64. The contact angle change during the 60s has been calculated and listed in Table 16. For comparison, the contact angle change of CS series binder has also been listed in Table 16. After remove core from CS binder, the contact angle change of HCS series binder is larger than CS series binder. This is implying a good affinity of HCS to electrolyte. This is due to the electrolyte can absorb into the vacancy of HCS polymer particles. Moreover, the contact angle of MXs/HCS is also higher than MXs/CS series binder. As a result, MXs/HCS can achieve both high electronic conductivity and high ion conductivity which is important characters for binder on energy storage system.

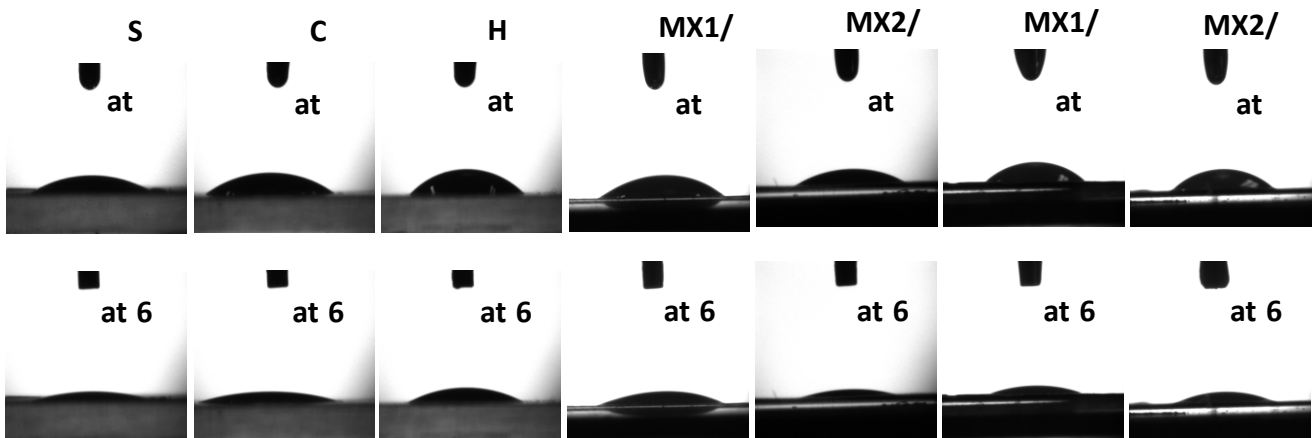
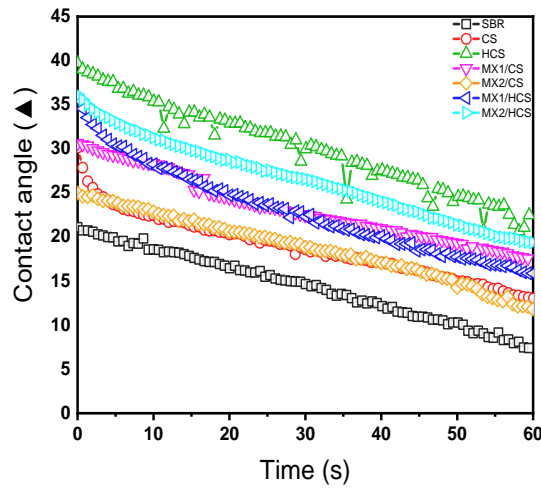


Figure 63: Contact angle of an electrolyte droplet fell down onto the binder films during the 60 s.

Table 16: Contact angle change of an electrolyte droplet fell onto the binder films during the 60 s.

contact angle change during 60s	
SBR	$20.11^{\circ} - 8.39^{\circ} = 11.72^{\circ}$
CS	$30.14^{\circ} - 13.12^{\circ} = 17.02^{\circ}$
HCS	$39.71^{\circ} - 22.47^{\circ} = 17.24^{\circ}$
MX1/CS	$30.63^{\circ} - 17.55^{\circ} = 13.08^{\circ}$
MX2/CS	$24.98^{\circ} - 11.79^{\circ} = 13.19^{\circ}$
MX1/HCS	$35.57^{\circ} - 15.86^{\circ} = 19.71^{\circ}$
MX2/HCS	$36.13^{\circ} - 19.36^{\circ} = 16.77^{\circ}$

4.5.1.4 Thermal property of binder film

The TGA was studied for comparing the thermal stability of CS series and HCS series binder. All the samples can be thermal stable under 280 °C. The HCS series binder start weight lost when temperature over than 300 °C, whereas CS series binder can be thermal stable up to 300 °C and start weight lost when temperature over than 350 °C. Therefore, the CS series binder has a better thermal stability than HCS series binder. This is probably due to the lost mechanical property of HCS series binder and it should be used at not high temperature operation conditions. In addition, the DSC of all polymer has been displayed in Table 17. The HCS series binder has a bigger T_g than CS series binder which indicating a hard polymer chains property of HCS series binder. Moreover, the MXs/HCS binder has a bigger T_g than HCS binder. This is due to the big MXene sheets prevented the HCS polymer chains mobility. No matter how, all the binder shows a satisfactory T_g range for applying as binder for energy storage system.

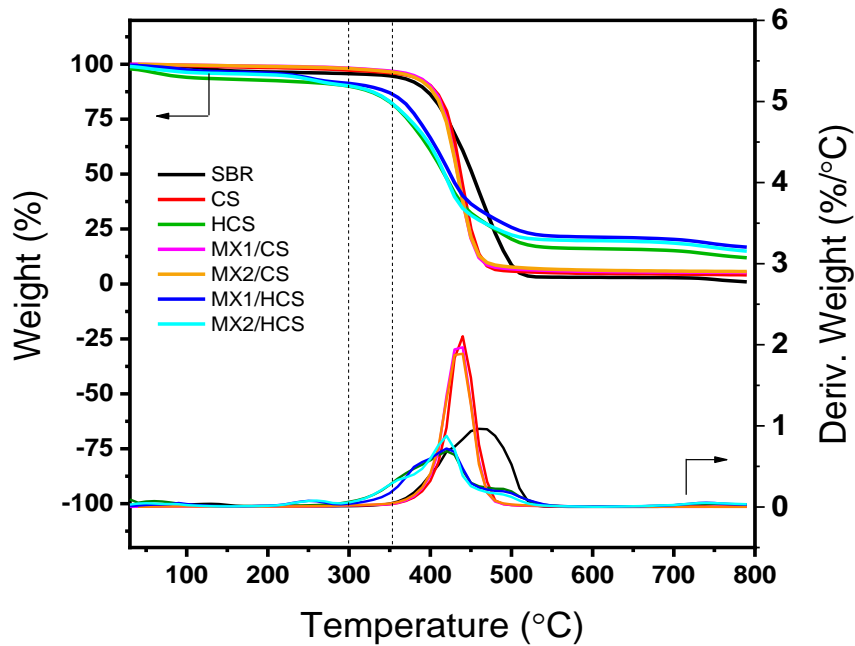


Figure 64: Thermogravimetry (TGA) of polymer film.

Table 17: Glass transition temperature of different polymer.

	SBR	CS	HCS	MX1/CS	MX2/CS	MX1/HCS	MX2/HCS
T _g (°C)	-11.25±0.02	12.44±0.08	16.87±0.02	13.69±0.05	12.76±0.07	17.80±0.06	17.31±0.01

4.5.1.5 Ion conductivity of binder solution

The ion conductivity of polymer solution is shown as Fig. 66. The HCS binder series shows high ion conductivity than CS series binder and SBR binder. This is due to the core polymer come out from core shell structure binder with COO- function groups which possess a good ion conductivity. And at the present of MXene, the MXs/HCS binder still can hold their good ion conductivity value which may improve the electrochemical performance when applied as binder in EDLCs.

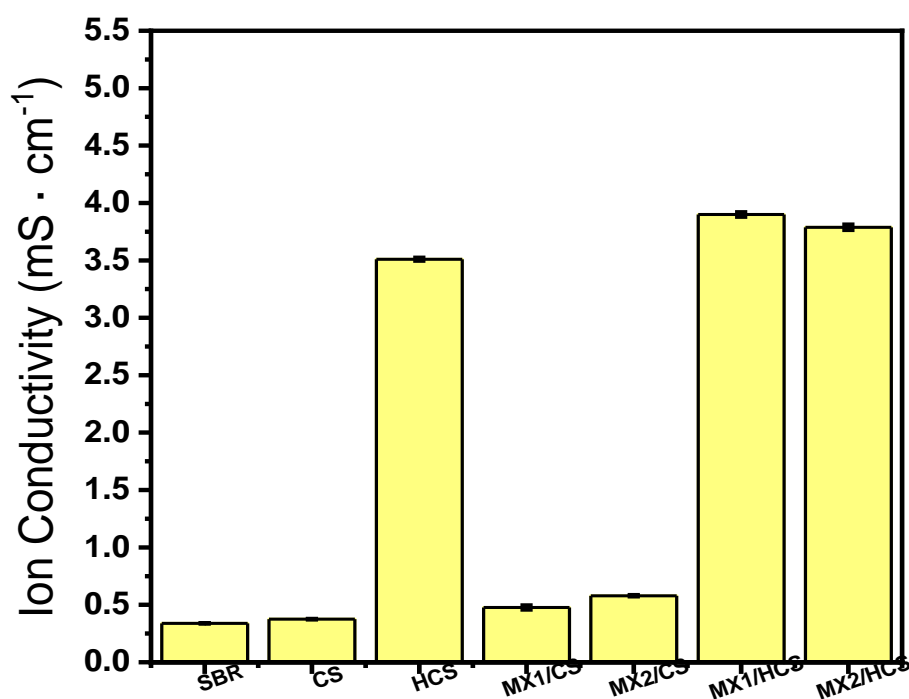


Figure 65: Ion conductivity of polymer solution.

4.5.1.6 Electrode adhesive property

The one of the most important property of binder is their adhesive strength that used for keeping all the components of electrode can have a good conductive network for achieve a good application performance. Therefore, the adhesive strength was measured by 180 ° peeling force test with a speed 60 mm/min and the adhesive strength value with error bar is shown in Fig. 67. The SBR has the strongest adhesive strength, and HCS series binder followed. This is because the COO- is a kind of sticky function group for attach electrode components on etching Al-foil. So, all the HCS series binder show a sticky property than CS series. Besides, MXene sheets didn't reduce the adhesive strength very much comparing with HCS binder. So, all of the samples in the figure can be used as binder with enough adhesive strength to keep electrode integrity.

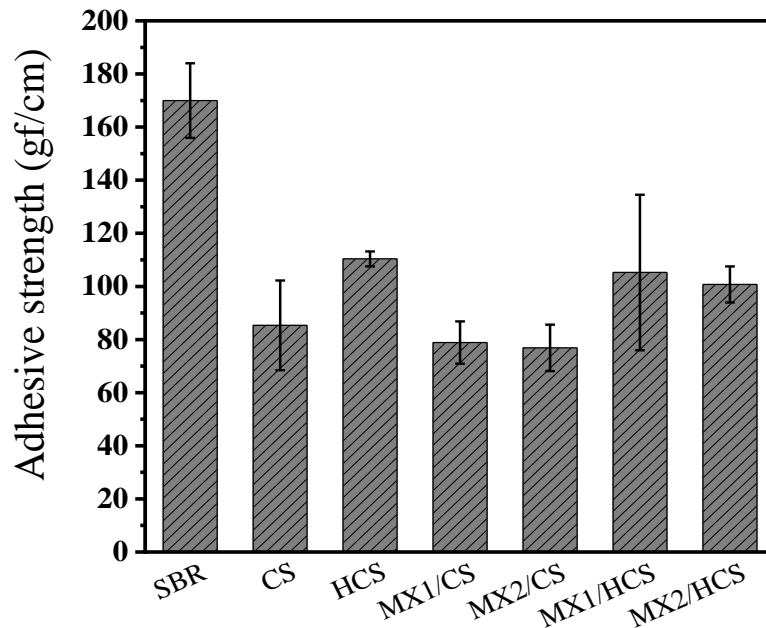


Figure 66: The adhesion strength value of electrodes of different binder with an error bar.

4.5.1.7 BET

Similar with CS series binder, the BET of electrodes has conducted first for investigating the surface area of electrode particles which is an important characteristic for EDLCs. The nitrogen adsorption and desorption isotherms curves shown as Fig. 68, and the porosity information of EDLCs electrodes are displayed in Table. 18. The surface area of HCS is about $1168 \text{ m}^2 \text{ g}^{-1}$, and at the present of MXene, the BET surface area decreased a little bit. This is probably due to the large sheets size of MXene, it is around $7 \mu\text{m}$. Besides, the declined total pore volume of MXs/HCS also indicating partial of pores have been blocked by MXene sheets. However, this blocking effect can be usually found in binder system, and the blocking effect is acceptable for EDLCs tests.

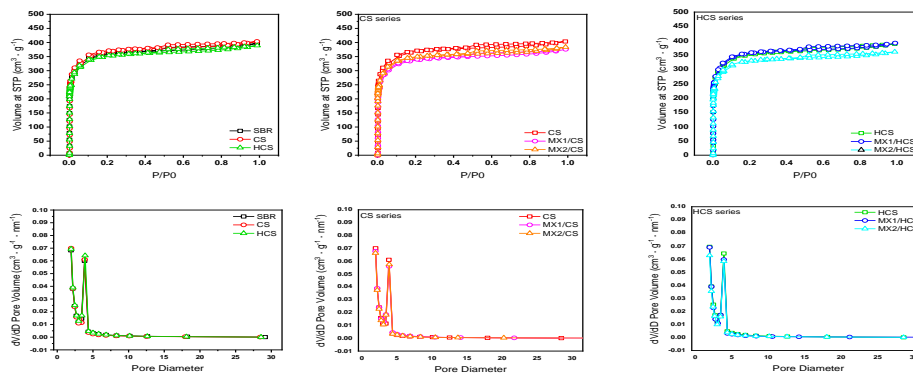


Figure 67: (up) Nitrogen adsorption/desorption isotherms curves of supercapacitor electrodes excluding current collectors; (down) Electrodes pore diameter distribution based on the BJH method.

Table 18: Porosity information of EDLCs electrodes with different binder.

	S_{BET} ($\text{m}^2 \text{ g}^{-1}$)	S_{micro} ($\text{m}^2 \text{ g}^{-1}$)	S_{meso} ($\text{m}^2 \text{ g}^{-1}$)	$V_{\text{total pore}}$ ($\text{cm}^3 \text{ g}^{-1}$)	$V_{\text{micropore}}$ ($\text{cm}^3 \text{ g}^{-1}$)	Pore width aver (nm)
SBR	1193.51	943.85	258.66	0.61	0.44	2.06
CS	1206.95	929.25	277.70	0.62	0.44	2.07
MX1/CS	1166.47	909.69	256.77	0.58	0.41	1.99
MX2/CS	1162.44	914.59	247.85	0.59	0.43	2.04
HCS	1168.50	907.42	261.09	0.60	0.43	2.06
MX1/HCS	1154.69	901.04	253.65	0.60	0.43	2.06
MX2/HCS	1140.01	880.58	259.43	0.56	0.40	1.96

4.5.2 Electrochemical properties

4.5.2.1 CV of EDLCs with different binder

The CV of EDLCs with different binder are shown as Fig. 70. The CV was conducted with scan rate from 5 mV/s to 100 mV/s. The response current increase as increasing the scan rate. All the figures show a typical supercapacitor CV curves without any obvious peaks at a voltage range 0.0-3.0 V. This is indicating that there is not any chemical reaction happened in the EDLCs, and binders are electrochemical stable enough to apply on EDLCs. So, we can conclude that the electrode with different binder system can be operated in a volage range 0.0-3.0 V without any electrochemical reaction happen. As a result, we choose the voltage range 0.1-2.7 V as charge and discharge measurement settings. And further electrochemical tests were conducted as follows.

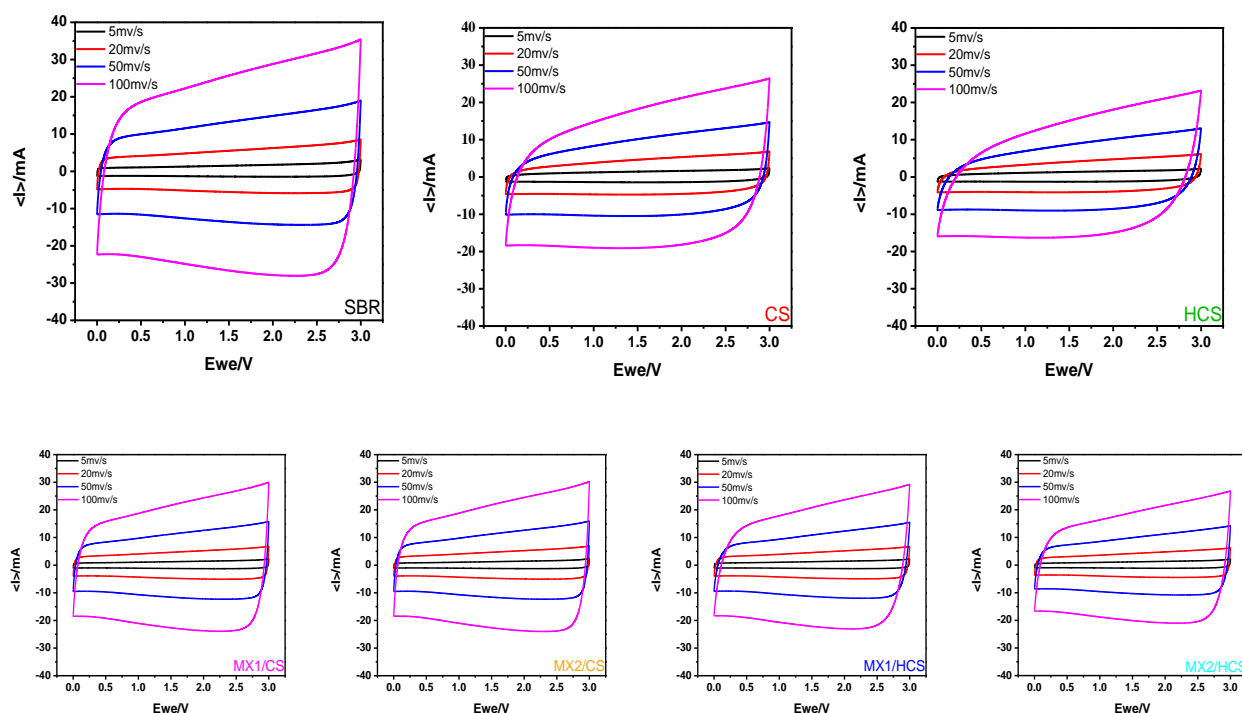


Figure 68: Cyclic voltammetry (CV) of EDLCs.

4.5.2.2 IMP of EDLCs

The charge transfer resistance of HCS series binder has been shown in Fig. 71 and compared with CS series binder. At the present of MXene sheets, the charge transfer resistance of MXs/HCS is smaller than HCS binder base on a smaller semicircle in the middle frequency range. This is due to the good electronic conductivity of MXene sheets and reduced the charge transfer resistance of HCS polymer binder. However, the HCS series binder's charge transfer resistance is slightly larger than CS series binder. This may be due to the good mechanical strength of CS series binder and leading to a good electrode condition comparing with HCS series binder. No matter how, there is no doubt of the effect of MXene sheets in polymer matrix. So, the electronic conductive binder can improve the electrode charge transfer ability.

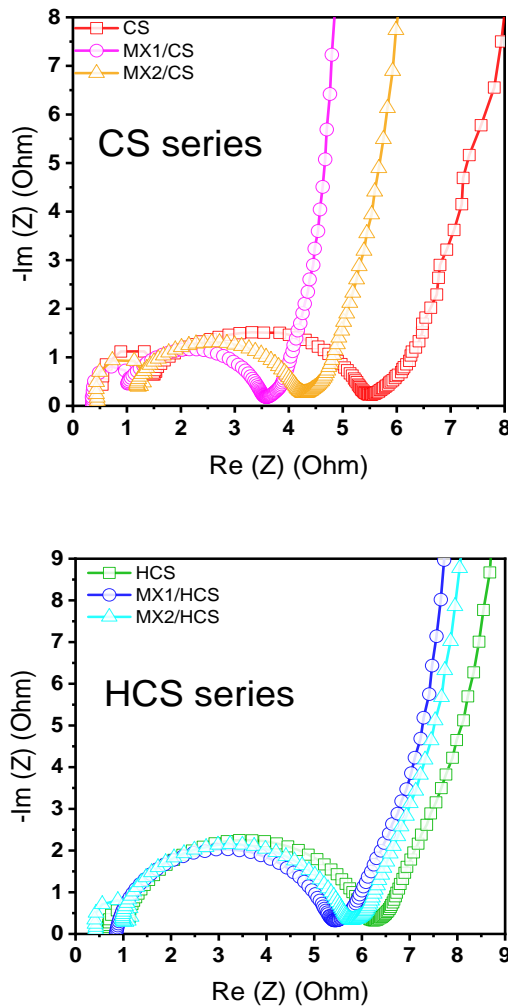


Figure 69: Nyquist plot of EDLCs with the frequency from 10^6 Hz to 10^{-2} Hz at $E = 0$ V after 10,000 cycles.

4.5.2.3 Cycling and high-rate performance of EDLCs

The high adhesive HCS series binder was applied as binder on EDLCs, and charge discharge for more than 10,000 cycles at a voltage range 0.1-2.7 V. the discharge capacitance was calculated and shown as Fig. 72. All the EDLCs can be charge and discharge stability and with a good columbic efficiency. The EDLCs with HCS series binder show higher discharge capacitance than commercial SBR binder, and with high electronic conductive binder MXs/HCS help, the discharge capacitance has been improved. So, the MXs/HCS can be a promising binder for EDLCs. Besides, both CS series and HCS series binder cycling performance were compared in same figure so that the performance of both binders can be studied carefully. The MXs/CS binder show the highest discharge capacitance overall, this is due to the good mechanical strength, good electronic conductivity, and flexibility of MXs/CS binder. These characters effect can also be futher proved by high-rate performance that shown in Fig. 73. At high current density, the binder with good mechanical strength and good electronic conductivity is more important for improve the electrochemical performance of EDLCs. So, the EDLCs with MXs/CS binder shows the highest discharge capacitance at the current density 50 mA/cm². Above all, a good binder for energy storage system should not only have good adhesive property but also good mechanical strength, electronic conductivity and good ion diffusion property. So we can conclude that MXs/CS and MXs/HCS are qualified to be used as binder for EDLCs.

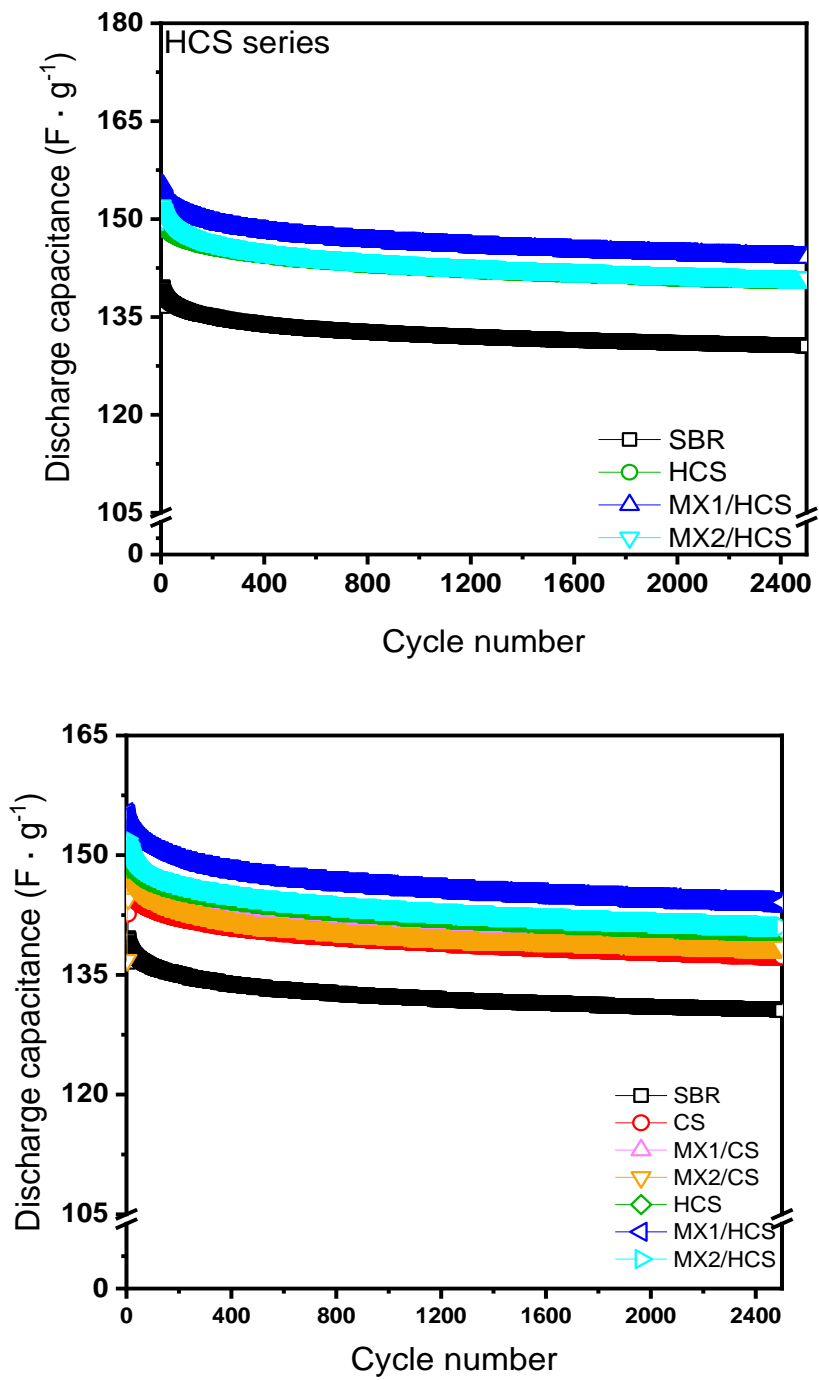


Figure 70: EDLCs cycling performance with different binder for 2500 cycles.

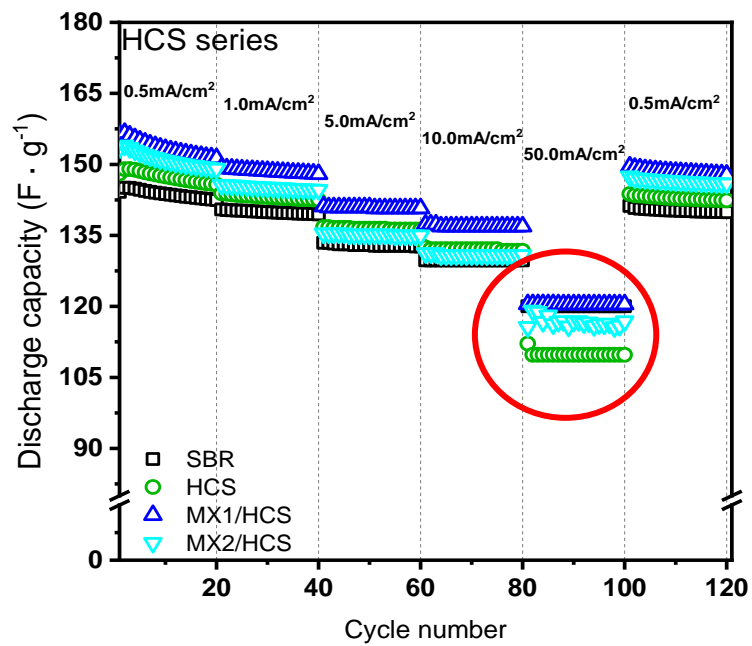
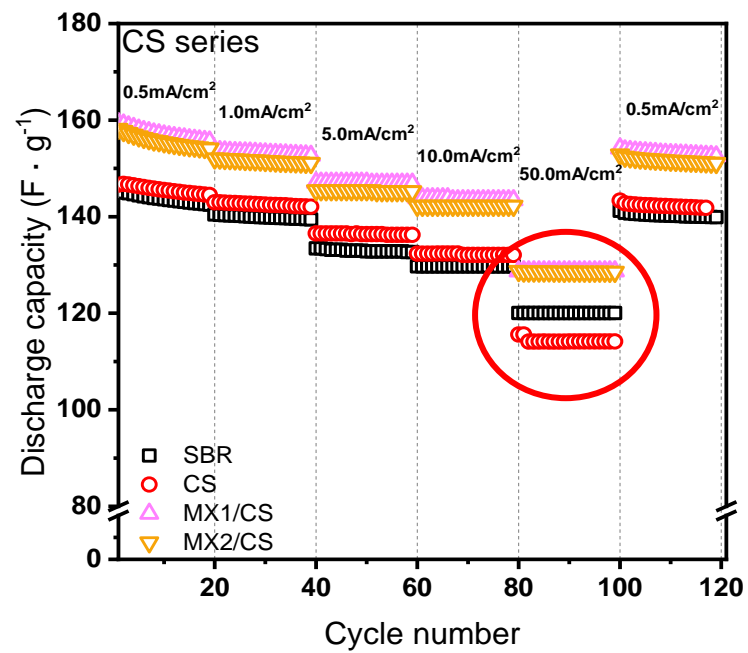


Figure 71: EDLCs rate capability performance with different binder for 20 cycles at each current.

CHAPTER 5: CONCLUSIONS

A conductive PPy component was incorporated successfully into a water dispersed PANBA binder using a two-step emulsion polymerization process. The conductive PANBA-PPy emulsified binders were applied to LTO electrodes for the first time. The LTO electrodes containing the conductive PANBA-PPy binders showed outstanding rate capability and stable long-life cycling performance. This was attributed to the combination of the adhesive segment of PANBA with the conductive segment PPy in the binder system. Among the LTO electrodes, the LTO electrode containing the PANBA-PPy4 binder, which was copolymerized with 4 g of pyrrole in 30 g of PANBA, had lower charge transfer and electrical resistance, and thus better initial discharge capacity, coulombic efficiency, and capacity retention during the charge/discharge process at a 1 C current rate than the other electrodes containing the other conductive PANBA-PPy binders and non-conductive PANBA binder. In contrast, PANBA-PPy2 showed remarkable performance in the high current-rate cycling test: discharge capacities of 152 mAh g⁻¹ and 136 mAh g⁻¹ at 5 C and 10 C, respectively. This is because PANBA-PPy2 has stronger adhesion capability than PANBA-PPy4 that allows it to endure the impact caused by the high current density.

The conductive polymer composite poly(pyrrole/acrylonitrile-co-butyl acrylate) (PPyANBA) has been successfully synthesized by an in-situ two step emulsion polymerization with PPy as a conductive filler and PANBA as a main polymer matrix, as well as applied to EDLCs as the water-based binder, where it has shown promising electrochemical performance. The first step is to polymerize pyrrole in water medium, followed by the emulsion polymerization of poly(acrylonitrile-co-butyl acrylate) using the water-dispersed polypyrrole. The emulsion polymerization is a good way to polymerize the conductive polymer composite, because the continuous stirring force can form uniform polymer particles and a long-term stable polymer solution without sacrificing thermal stability. These polymer particles have a good distribution as well as less electrode pore blocking, which is beneficial for EDLCs cycling performance. The conductive polymer composite binder PPyANBA decreases not only the electrodes resistance but also the interface resistance between the electrode and the current collector. Furthermore, charges can be also moved easier in electrode pores with the PPyANBA

binder when alternative current is applied. Overall, the EDLCs containing the conductive PPyANBA binder are superior to those containing the nonconductive PANBA binder in long-term cycles at moderate current densities up to 10 mA cm^{-2} .

For the first time, in-situ polymerization method is used to synthesize MXene clay/poly (acrylonitrile-co-butyl acrylate) (MXC/PANBA) conducting binder. We show that an activated carbon EDLC electrode with in-situ polymerized MXC/PANBA binder shows superior performance (23.6 Wh kg^{-1} at 8510 W kg^{-1}) than the one with only PANBA binder (no MXene clay) (23 Wh kg^{-1} at 1472.6 W kg^{-1}). Further, the MXC/PANBA-containing EDLCs maintain excellent performance at very high current densities up to 50 mA cm^{-2} , whereas the PANBA-containing EDLCs do not survive at such high currents. We show that activated carbon EDLC electrodes with MXC/PANBA binder reduce the electrode resistance (electronic, interface and charge transfer resistance) as compared to the one with PANBA binder alone. The strong interaction in the MXC/PANBA provide an improved pathway for the movement of electrons in the binder film. We also show that addition of MXC to the PANBA enhance the physical stability of the binder emulsion and the mechanical toughness of the binder film, without affecting the thermal and electrochemical stability of the PANBA alone. Moreover, the MXC in the PANBA binder does not seriously block the pores in the activated carbon. The enhanced performance of in-situ polymerized MXene clay/PANBA binder is attributed to improved conductivity, toughness, and adhesion to the electrode components due to superior interactions between MXene clay and PANBA via in-situ polymerization method. To summarize, the use of conductive MXC in the nonconducting polymer binder is an efficient way to improve the high-power performance of the EDLCs.

The water-based core shell structure polymer binder and hollow core shell structure polymer binder have studied and compared. Recording to the results that discussed above, we can conclude that MXs/CS and MXs/HCS are qualified to be used as binder for EDLCs. A good binder for energy storage system should not only have good adhesive property but also good mechanical strength, electronic conductivity, and good ion diffusion property. And more experiments need to be carried out for comprehensive understanding of water-based CS and HCS series binder.

CHAPTER 6: REFERENCES

- [1] D. Bresser *et al.*, “Perspectives of automotive battery R&D in China, Germany, Japan, and the USA,” *J. Power Sources*, vol. 382, pp. 176–178, Apr. 2018, doi: 10.1016/j.jpowsour.2018.02.039.
- [2] B. Scrosati and J. Garche, “Lithium batteries: Status, prospects and future,” *J. Power Sources*, vol. 195, no. 9, pp. 2419–2430, May 2010, doi: 10.1016/j.jpowsour.2009.11.048.
- [3] J.-M. Tarascon and M. Armand, “Issues and challenges facing rechargeable lithium batteries,” *Nature*, vol. 414, no. 6861, Art. no. 6861, Nov. 2001, doi: 10.1038/35104644.
- [4] X. Zuo, J. Zhu, P. Müller-Buschbaum, and Y.-J. Cheng, “Silicon based lithium-ion battery anodes: A chronicle perspective review,” *Nano Energy*, vol. 31, pp. 113–143, Jan. 2017, doi: 10.1016/j.nanoen.2016.11.013.
- [5] A. Manthiram, “An Outlook on Lithium Ion Battery Technology,” *ACS Cent. Sci.*, vol. 3, no. 10, pp. 1063–1069, Oct. 2017, doi: 10.1021/acscentsci.7b00288.
- [6] K. D. Fong, T. Wang, and S. K. Smoukov, “Multidimensional performance optimization of conducting polymer-based supercapacitor electrodes,” *Sustain. Energy Fuels*, vol. 1, no. 9, pp. 1857–1874, 2017, doi: 10.1039/C7SE00339K.
- [7] J.-H. Choi *et al.*, “High capacitance and energy density supercapacitor based on biomass-derived activated carbons with reduced graphene oxide binder,” *Carbon*, vol. 132, pp. 16–24, Jun. 2018, doi: 10.1016/j.carbon.2018.01.105.
- [8] K. D. Fong, T. Wang, H.-K. Kim, R. V. Kumar, and S. K. Smoukov, “Semi-Interpenetrating Polymer Networks for Enhanced Supercapacitor Electrodes,” *ACS Energy Lett.*, vol. 2, no. 9, pp. 2014–2020, Sep. 2017, doi: 10.1021/acsenerylett.7b00466.
- [9] B. Hu *et al.*, “The existence of optimal molecular weight for poly(acrylic acid) binders in silicon/graphite composite anode for lithium-ion batteries,” *J. Power Sources*, vol. 378, pp. 671–676, Feb. 2018, doi: 10.1016/j.jpowsour.2017.12.068.
- [10] P.-F. Cao *et al.*, “Effect of Binder Architecture on the Performance of Silicon/Graphite Composite Anodes for Lithium Ion Batteries,” *ACS Appl. Mater. Interfaces*, vol. 10, no. 4, pp. 3470–3478, Jan. 2018, doi: 10.1021/acsam.7b13205.
- [11] M. H. T. Nguyen and E.-S. Oh, “Application of a new acrylonitrile/butylacrylate water-based binder for negative electrodes of lithium-ion batteries,” *Electrochem. Commun.*, vol. 35, pp. 45–48, Oct. 2013, doi: 10.1016/j.elecom.2013.07.042.
- [12] J. Garche, C. K. Dyer, P. T. Moseley, Z. Ogumi, D. A. J. Rand, and B. Scrosati, *Encyclopedia of Electrochemical Power Sources*. Newnes, 2013.
- [13] J. Christensen and J. Newman, “Stress generation and fracture in lithium insertion materials,” *J. Solid State Electrochem.*, vol. 10, no. 5, pp. 293–319, May 2006, doi: 10.1007/s10008-006-0095-1.
- [14] J. Li and J. R. Dahn, “An In Situ X-Ray Diffraction Study of the Reaction of Li with Crystalline Si,” *J. Electrochem. Soc.*, vol. 154, no. 3, p. A156, Jan. 2007, doi: 10.1149/1.2409862.
- [15] B. A. Boukamp, G. C. Lesh, and R. A. Huggins, “All-Solid Lithium Electrodes with Mixed-Conductor Matrix,” *J. Electrochem. Soc.*, vol. 128, no. 4, p. 725, Apr. 1981, doi: 10.1149/1.2127495.

- [16] S. Megahed and B. Scrosati, "Lithium-ion rechargeable batteries," *J. Power Sources*, vol. 51, no. 1, pp. 79–104, Aug. 1994, doi: 10.1016/0378-7753(94)01956-8.
- [17] T. Tanaka, K. Ohta, and N. Arai, "Year 2000 R&D status of large-scale lithium ion secondary batteries in the national project of Japan," *J. Power Sources*, vol. 97–98, pp. 2–6, Jul. 2001, doi: 10.1016/S0378-7753(01)00502-X.
- [18] R. Fong, U. von Sacken, and J. R. Dahn, "Studies of Lithium Intercalation into Carbons Using Nonaqueous Electrochemical Cells," *J. Electrochem. Soc.*, vol. 137, no. 7, p. 2009, Jul. 1990, doi: 10.1149/1.2086855.
- [19] S. Sun, F. Han, X. Wu, and Z. Fan, "One-step synthesis of biomass derived O, N-codoped hierarchical porous carbon with high surface area for supercapacitors," *Chin. Chem. Lett.*, Nov. 2019, doi: 10.1016/j.ccllet.2019.11.023.
- [20] D. Kasprzak, I. Stepniak, and M. Galiński, "Electrodes and hydrogel electrolytes based on cellulose: fabrication and characterization as EDLC components," *J. Solid State Electrochem.*, vol. 22, no. 10, pp. 3035–3047, Oct. 2018, doi: 10.1007/s10008-018-4015-y.
- [21] D. Bresser, D. Buchholz, A. Moretti, A. Varzi, and S. Passerini, "Alternative binders for sustainable electrochemical energy storage – the transition to aqueous electrode processing and bio-derived polymers," *Energy Environ. Sci.*, vol. 11, no. 11, pp. 3096–3127, 2018, doi: 10.1039/C8EE00640G.
- [22] C. Dong *et al.*, "3D binder-free Cu₂O@Cu nanoneedle arrays for high-performance asymmetric supercapacitors," *J Mater Chem A*, vol. 2, no. 43, pp. 18229–18235, Sep. 2014, doi: 10.1039/C4TA04329D.
- [23] C. Zheng, X. Zhou, H. Cao, G. Wang, and Z. Liu, "Synthesis of porous graphene/activated carbon composite with high packing density and large specific surface area for supercapacitor electrode material," *J. Power Sources*, vol. 258, pp. 290–296, Jul. 2014, doi: 10.1016/j.jpowsour.2014.01.056.
- [24] B. Pal, S. Yang, S. Ramesh, V. Thangadurai, and R. Jose, "Electrolyte selection for supercapacitive devices: a critical review," *Nanoscale Adv.*, vol. 1, no. 10, pp. 3807–3835, Oct. 2019, doi: 10.1039/C9NA00374F.
- [25] M. Yoshio, R. J. Brodd, and A. Kozawa, Eds., *Lithium-Ion Batteries: Science and Technologies*. New York: Springer-Verlag, 2009.
- [26] S. Hu, Y. Li, J. Yin, H. Wang, X. Yuan, and Q. Li, "Effect of different binders on electrochemical properties of LiFePO₄/C cathode material in lithium ion batteries," *Chem. Eng. J.*, vol. 237, pp. 497–502, Feb. 2014, doi: 10.1016/j.cej.2013.08.119.
- [27] M. Ling, J. Qiu, S. Li, H. Zhao, G. Liu, and S. Zhang, "An environmentally benign LIB fabrication process using a low cost, water soluble and efficient binder," *J. Mater. Chem. A*, vol. 1, no. 38, p. 11543, 2013, doi: 10.1039/c3ta12159c.
- [28] S. Zhang and R. Jow, "047. Study of poly(acrylonitrile-methyl methacrylate) as binder for graphite anode and LiMn₂O₄ cathode of Li-ion batteries," *J. Power Sources*, vol. 109, pp. 422–426, Jul. 2002, doi: 10.1016/S0378-7753(02)00107-6.
- [29] L. Gong, M. H. T. Nguyen, and E.-S. Oh, "High polar polyacrylonitrile as a potential binder for negative electrodes in lithium ion batteries," *Electrochem. Commun.*, vol. 29, pp. 45–47, Apr. 2013, doi: 10.1016/j.elecom.2013.01.010.
- [30] "Effect of Copolymer Composition on the Dynamic Mechanical and Thermal Behaviour of Butyl Acrylate-Acrylonitrile Copolymers - Suresh - 2003 - Macromolecular Materials and Engineering - Wiley Online Library."

<https://onlinelibrary.wiley.com/doi/full/10.1002/mame.200300116> (accessed Apr. 23, 2020).

- [31] N. A. Mohd Radzuan, A. B. Sulong, and J. Sahari, "A review of electrical conductivity models for conductive polymer composite," *Int. J. Hydrog. Energy*, vol. 42, no. 14, pp. 9262–9273, Apr. 2017, doi: 10.1016/j.ijhydene.2016.03.045.
- [32] H. Deng, L. Lin, M. Ji, S. Zhang, M. Yang, and Q. Fu, "Progress on the morphological control of conductive network in conductive polymer composites and the use as electroactive multifunctional materials," *Prog. Polym. Sci.*, vol. 39, no. 4, pp. 627–655, Apr. 2014, doi: 10.1016/j.progpolymsci.2013.07.007.
- [33] W. Zeng *et al.*, "Enhanced Ion Conductivity in Conducting Polymer Binder for High-Performance Silicon Anodes in Advanced Lithium-Ion Batteries," *Adv. Energy Mater.*, vol. 8, no. 11, p. 1702314, 2018, doi: 10.1002/aenm.201702314.
- [34] K. Lee and T.-H. Kim, "Poly(aniline-co-anthranilic acid) as an electrically conductive and mechanically stable binder for high-performance silicon anodes," *Electrochimica Acta*, vol. 283, pp. 260–268, Sep. 2018, doi: 10.1016/j.electacta.2018.06.175.
- [35] Y. Luo *et al.*, "Applications of polyaniline for Li-ion batteries, Li-sulfur batteries and supercapacitors," *ChemSusChem*, Oct. 2018, doi: 10.1002/cssc.201802186.
- [36] M. Naguib *et al.*, "Two-Dimensional Nanocrystals Produced by Exfoliation of Ti_3AlC_2 ," *Adv. Mater.*, vol. 23, no. 37, pp. 4248–4253, Oct. 2011, doi: 10.1002/adma.201102306.
- [37] J. Yan *et al.*, "Flexible MXene/Graphene Films for Ultrafast Supercapacitors with Outstanding Volumetric Capacitance," *Adv. Funct. Mater.*, vol. 27, no. 30, p. 1701264, Aug. 2017, doi: 10.1002/adfm.201701264.
- [38] M. Boota *et al.*, "Interaction of Polar and Nonpolar Polyfluorenes with Layers of Two-Dimensional Titanium Carbide (MXene): Intercalation and Pseudocapacitance," *Chem. Mater.*, vol. 29, no. 7, pp. 2731–2738, Apr. 2017, doi: 10.1021/acs.chemmater.6b03933.
- [39] F. Shahzad *et al.*, "Electromagnetic interference shielding with 2D transition metal carbides (MXenes)," *Science*, vol. 353, no. 6304, pp. 1137–1140, Sep. 2016, doi: 10.1126/science.aag2421.
- [40] J. Fu, J. Yun, S. Wu, L. Li, L. Yu, and K. H. Kim, "Architecturally Robust Graphene-Encapsulated MXene Ti_2CT_x @Polyaniline Composite for High-Performance Pouch-Type Asymmetric Supercapacitor," *ACS Appl. Mater. Interfaces*, vol. 10, no. 40, pp. 34212–34221, Oct. 2018, doi: 10.1021/acsami.8b10195.
- [41] Y. Huang *et al.*, "Conductive Polymer Composites from Renewable Resources: An Overview of Preparation, Properties, and Applications," *Polymers*, vol. 11, no. 2, p. 187, Jan. 2019, doi: 10.3390/polym11020187.
- [42] G. Mittal, V. Dhand, K. Y. Rhee, S.-J. Park, and W. R. Lee, "A review on carbon nanotubes and graphene as fillers in reinforced polymer nanocomposites," *J. Ind. Eng. Chem.*, vol. 21, pp. 11–25, Jan. 2015, doi: 10.1016/j.jiec.2014.03.022.
- [43] C. S. Chern, "Emulsion polymerization mechanisms and kinetics," *Prog. Polym. Sci.*, vol. 31, no. 5, pp. 443–486, May 2006, doi: 10.1016/j.progpolymsci.2006.02.001.
- [44] S. Maruthamuthu, J. Chandrasekaran, D. Manoharan, and R. Magesh, "Conductivity and dielectric analysis of nanocolloidal polypyrrole particles functionalized with higher weight percentage of poly(styrene sulfonate) using the dispersion

- polymerization method,” *J. Polym. Eng.*, vol. 37, no. 5, Jan. 2017, doi: 10.1515/polyeng-2015-0321.
- [45] Y. Fu, Y.-S. Su, and A. Manthiram, “Sulfur-Polypyrrole Composite Cathodes for Lithium-Sulfur Batteries,” *J. Electrochem. Soc.*, vol. 159, no. 9, pp. A1420–A1424, 2012, doi: 10.1149/2.027209jes.
- [46] C. Li, J. Tan, H. Li, J. Gu, B. Zhang, and Q. Zhang, “Fast magnetic-field-induced formation of one-dimensional structured chain-like materials via sintering of Fe₃O₄/poly(styrene-co-n-butyl acrylate-co-acrylic acid) hybrid microspheres,” *RSC Adv.*, vol. 5, no. 36, pp. 28735–28742, Mar. 2015, doi: 10.1039/C4RA16809G.
- [47] H. Wu *et al.*, “A novel multifunctional biomedical material based on polyacrylonitrile: Preparation and characterization,” *Mater. Sci. Eng. C*, vol. 62, pp. 702–709, May 2016, doi: 10.1016/j.msec.2016.02.026.
- [48] U. Geißler, M. L. Hallensleben, and L. Toppare, “Conducting polymer composites of poly(N-methylpyrrole) and poly(bisphenol-A-carbonate),” *Adv. Mater.*, vol. 3, no. 2, pp. 104–106, 1991, doi: 10.1002/adma.19910030207.
- [49] B.-R. Lee and E.-S. Oh, “Effect of Molecular Weight and Degree of Substitution of a Sodium-Carboxymethyl Cellulose Binder on Li₄Ti₅O₁₂ Anodic Performance,” *J. Phys. Chem. C*, vol. 117, no. 9, pp. 4404–4409, Mar. 2013, doi: 10.1021/jp311678p.
- [50] S.-L. Chou, J.-Z. Wang, H.-K. Liu, and S.-X. Dou, “Rapid Synthesis of Li₄Ti₅O₁₂ Microspheres as Anode Materials and Its Binder Effect for Lithium-Ion Battery,” *J. Phys. Chem. C*, vol. 115, no. 32, pp. 16220–16227, Aug. 2011, doi: 10.1021/jp2039256.
- [51] Y. Qi, M. H. T. Nguyen, and E.-S. Oh, “Enhancement of the lithium titanium oxide anode performance by the copolymerization of conductive polypyrrole with poly(acrylonitrile/butyl acrylate) binder,” *J. Appl. Electrochem.*, vol. 50, no. 4, pp. 431–438, Apr. 2020, doi: 10.1007/s10800-020-01401-8.
- [52] K. Arora *et al.*, “Application of electrochemically prepared polypyrrole–polyvinyl sulphonate films to DNA biosensor,” *Biosens. Bioelectron.*, vol. 21, no. 9, pp. 1777–1783, Mar. 2006, doi: 10.1016/j.bios.2005.09.002.
- [53] M. A. Chougule, S. G. Pawar, P. R. Godse, R. N. Mulik, S. Sen, and V. B. Patil, “Synthesis and Characterization of Polypyrrole (PPy) Thin Films,” *Soft Nanosci. Lett.*, vol. 01, no. 01, pp. 6–10, 2011, doi: 10.4236/snsl.2011.11002.
- [54] L. Chen, L. Bromberg, H. Schreuder-Gibson, J. Walker, T. Alan Hatton, and G. C. Rutledge, “Chemical protection fabrics via surface oximation of electrospun polyacrylonitrile fiber mats,” *J. Mater. Chem.*, vol. 19, no. 16, p. 2432, 2009, doi: 10.1039/b818639a.
- [55] A. Ding, G. Lu, H. Guo, and X. Huang, “Double-bond-containing polyallene-based triblock copolymers via phenoxyallene and (meth)acrylate,” *Sci. Rep.*, vol. 7, no. 1, p. 43706, May 2017, doi: 10.1038/srep43706.
- [56] P. L. Taberna, P. Simon, and J. F. Fauvarque, “Electrochemical Characteristics and Impedance Spectroscopy Studies of Carbon-Carbon Supercapacitors,” *J. Electrochem. Soc.*, vol. 150, no. 3, p. A292, 2003, doi: 10.1149/1.1543948.
- [57] B. C. Ennis and V.-T. Truong, “Thermal and electrical stability of polypyrrole at elevated temperatures,” *Synth. Met.*, vol. 59, no. 3, pp. 387–399, Aug. 1993, doi: 10.1016/0379-6779(93)91170-7.
- [58] B. Song, F. Wu, Y. Zhu, Z. Hou, K. Moon, and C.-P. Wong, “Effect of polymer binders on graphene-based free-standing electrodes for supercapacitors,”

- Electrochimica Acta*, vol. 267, pp. 213–221, Mar. 2018, doi: 10.1016/j.electacta.2018.02.072.
- [59] Y. Hu, H. Liu, Q. Ke, and J. Wang, “Effects of nitrogen doping on supercapacitor performance of a mesoporous carbon electrode produced by a hydrothermal soft-templating process,” *J. Mater. Chem. A*, vol. 2, no. 30, p. 11753, Jun. 2014, doi: 10.1039/C4TA01269K.
- [60] M. Aslan, D. Weingarh, N. Jäckel, J. S. Atchison, I. Grobelsek, and V. Presser, “Polyvinylpyrrolidone as binder for castable supercapacitor electrodes with high electrochemical performance in organic electrolytes,” *J. Power Sources*, vol. 266, pp. 374–383, Nov. 2014, doi: 10.1016/j.jpowsour.2014.05.031.
- [61] H. Moon *et al.*, “Ag/Au/Polypyrrole Core-shell Nanowire Network for Transparent, Stretchable and Flexible Supercapacitor in Wearable Energy Devices,” *Sci. Rep.*, vol. 7, no. 1, p. 41981, Feb. 2017, doi: 10.1038/srep41981.
- [62] School of Applied Physics, Faculty of Science and Technology, Universiti Kebangsaan Malaysia, 43600 Bangi, Selangor, Malaysia and N. S.M. Nor, “Supercapacitors using Binderless Activated Carbon Monoliths Electrodes consisting of a Graphite Additive and Pre-carbonized Biomass Fibers,” *Int. J. Electrochem. Sci.*, pp. 2520–2539, Mar. 2017, doi: 10.20964/2017.03.48.
- [63] K. J. Cai, Y. Zheng, P. Shen, and S. Y. Chen, “TiC_x-Ti₂C nanocrystals and epitaxial graphene-based lamellae by pulsed laser ablation of bulk TiC in vacuum,” *CrystEngComm*, vol. 16, no. 24, pp. 5466–5474, 2014, doi: 10.1039/C4CE00358F.
- [64] R. B. Rakhi, B. Ahmed, M. N. Hedhili, D. H. Anjum, and H. N. Alshareef, “Effect of Postetch Annealing Gas Composition on the Structural and Electrochemical Properties of Ti₂CT_x MXene Electrodes for Supercapacitor Applications,” *Chem. Mater.*, vol. 27, no. 15, pp. 5314–5323, Aug. 2015, doi: 10.1021/acs.chemmater.5b01623.
- [65] R. Liu and W. Li, “High-Thermal-Stability and High-Thermal-Conductivity Ti₃C₂T_x MXene/Poly(vinyl alcohol) (PVA) Composites,” *ACS Omega*, vol. 3, no. 3, pp. 2609–2617, Mar. 2018, doi: 10.1021/acsomega.7b02001.
- [66] S. Xu, G. Wei, J. Li, W. Han, and Y. Gogotsi, “Flexible MXene–graphene electrodes with high volumetric capacitance for integrated co-cathode energy conversion/storage devices,” *J. Mater. Chem. A*, vol. 5, no. 33, pp. 17442–17451, 2017, doi: 10.1039/C7TA05721K.
- [67] M. Claudino, J.-M. Mathevet, M. Jonsson, and M. Johansson, “Bringing d-limonene to the scene of bio-based thermoset coatings via free-radical thiol–ene chemistry: macromonomer synthesis, UV-curing and thermo-mechanical characterization,” *Polym. Chem.*, vol. 5, no. 9, pp. 3245–3260, 2014, doi: 10.1039/C3PY01302B.
- [68] L. Yin, J. Wang, F. Lin, J. Yang, and Y. Nuli, “Polyacrylonitrile/graphene composite as a precursor to a sulfur-based cathode material for high-rate rechargeable Li–S batteries,” *Energy Environ. Sci.*, vol. 5, no. 5, p. 6966, 2012, doi: 10.1039/c2ee03495f.
- [69] S.-J. Kim, B.-R. Lee, and E.-S. Oh, “Application of a bio-derivative, rosin, as a binder additive for lithium titanium oxide electrodes in lithium-ion batteries,” *J. Power Sources*, vol. 273, pp. 608–612, Jan. 2015, doi: 10.1016/j.jpowsour.2014.09.160.
- [70] B. Anasori, M. R. Lukatskaya, and Y. Gogotsi, “2D metal carbides and nitrides (MXenes) for energy storage,” *Nat. Rev. Mater.*, vol. 2, no. 2, p. 16098, Feb. 2017, doi: 10.1038/natrevmats.2016.98.

- [71] R. Li, L. Zhang, L. Shi, and P. Wang, "MXene Ti_3C_2 : An Effective 2D Light-to-Heat Conversion Material," *ACS Nano*, vol. 11, no. 4, pp. 3752–3759, Apr. 2017, doi: 10.1021/acsnano.6b08415.
- [72] M. Naguib *et al.*, "Two-Dimensional Transition Metal Carbides," *ACS Nano*, vol. 6, no. 2, pp. 1322–1331, Feb. 2012, doi: 10.1021/nn204153h.
- [73] S. N. Patel, A. E. Javier, G. M. Stone, S. A. Mullin, and N. P. Balsara, "Simultaneous Conduction of Electronic Charge and Lithium Ions in Block Copolymers," *ACS Nano*, vol. 6, no. 2, pp. 1589–1600, Feb. 2012, doi: 10.1021/nn2045664.
- [74] A. Nicolau, A. M. Nucci, E. M. A. Martini, and D. Samios, "Electrical impedance spectroscopy of epoxy systems II: Molar fraction variation, resistivity, capacitance and relaxation processes of 1,4-butanediol diglycidyl ether/succinic anhydride and triethylamine as initiator," *Eur. Polym. J.*, vol. 43, no. 6, pp. 2708–2717, Jun. 2007, doi: 10.1016/j.eurpolymj.2007.03.018.
- [75] A. M. Nucci, A. Nicolau, E. M. A. Martini, and D. Samios, "Electrical impedance spectroscopy of epoxy systems: The case of 1,4-butanediol diglycidyl ether/cis-1,2-cyclohexanedicarboxylic anhydride and triethylamine as initiator," *Eur. Polym. J.*, vol. 42, no. 1, pp. 195–202, Jan. 2006, doi: 10.1016/j.eurpolymj.2005.05.016.
- [76] S. B. Aziz, T. J. Woo, M. F. Z. Kadir, and H. M. Ahmed, "A conceptual review on polymer electrolytes and ion transport models," *J. Sci. Adv. Mater. Devices*, vol. 3, no. 1, pp. 1–17, Mar. 2018, doi: 10.1016/j.jsamd.2018.01.002.
- [77] Y. Yoo, S. Kim, B. Kim, and W. Kim, "2.5 V compact supercapacitors based on ultrathin carbon nanotube films for AC line filtering," *J. Mater. Chem. A*, vol. 3, no. 22, pp. 11801–11806, May 2015, doi: 10.1039/C5TA02073E.
- [78] C.-M. Wang *et al.*, "The Influence of Specific Surface Area on the Capacitance of the Carbon Electrodes Supercapacitor," presented at the The 3rd International Conference on Industrial Application Engineering 2015 (ICIAE2015), Feb. 2015, Accessed: Jan. 10, 2018. [Online]. Available: <https://www2.ia-engineers.org/iciae/index.php/iciae/iciae2015/paper/view/544>.
- [79] W.-C. Liao, F.-S. Liao, C.-T. Tsai, and Y.-P. Yang, "Preparation of Activated Carbon for Electric Double Layer Capacitors," *China Steel Tech. Rep.*, vol. 25, pp. 36–41, 2012.
- [80] I. Cho, J. Choi, K. Kim, M.-H. Ryou, and Y. M. Lee, "A comparative investigation of carbon black (Super-P) and vapor-grown carbon fibers (VGCFs) as conductive additives for lithium-ion battery cathodes," p. 7, 2015.
- [81] B.-A. Mei, O. Munteshari, J. Lau, B. Dunn, and L. Pilon, "Physical Interpretations of Nyquist Plots for EDLC Electrodes and Devices," *J. Phys. Chem. C*, vol. 122, no. 1, pp. 194–206, Jan. 2018, doi: 10.1021/acs.jpcc.7b10582.
- [82] K.-B. Li *et al.*, "Studies on the equivalent serial resistance of carbon supercapacitor," *Electrochimica Acta*, vol. 174, pp. 596–600, Aug. 2015, doi: 10.1016/j.electacta.2015.06.008.
- [83] Z. Li, J. Liu, K. Jiang, and T. Thundat, "Carbonized nanocellulose sustainably boosts the performance of activated carbon in ionic liquid supercapacitors," *Nano Energy*, vol. 25, pp. 161–169, Jul. 2016, doi: 10.1016/j.nanoen.2016.04.036.
- [84] R. Kötz and M. Carlen, "Principles and applications of electrochemical capacitors," *Electrochimica Acta*, vol. 45, no. 15, pp. 2483–2498, May 2000, doi: 10.1016/S0013-4686(00)00354-6.
- [85] C. Portet, G. Yushin, and Y. Gogotsi, "Electrochemical performance of carbon onions, nanodiamonds, carbon black and multiwalled nanotubes in electrical double

- layer capacitors,” *Carbon*, vol. 45, no. 13, pp. 2511–2518, Nov. 2007, doi: 10.1016/j.carbon.2007.08.024.
- [86] Y.-R. Nian and H. Teng, “Influence of surface oxides on the impedance behavior of carbon-based electrochemical capacitors,” *J. Electroanal. Chem.*, vol. 540, pp. 119–127, Jan. 2003, doi: 10.1016/S0022-0728(02)01299-8.
- [87] K. Hung, C. Masarapu, T. Ko, and B. Wei, “Wide-temperature range operation supercapacitors from nanostructured activated carbon fabric,” *J. Power Sources*, vol. 193, no. 2, pp. 944–949, Sep. 2009, doi: 10.1016/j.jpowsour.2009.01.083.
- [88] I. Yang, S.-G. Kim, S. H. Kwon, M.-S. Kim, and J. C. Jung, “Relationships between pore size and charge transfer resistance of carbon aerogels for organic electric double-layer capacitor electrodes,” *Electrochimica Acta*, vol. 223, pp. 21–30, Jan. 2017, doi: 10.1016/j.electacta.2016.11.177.
- [89] Q. Li, Y. Q. Zhu, and S. J. Eichhorn, “Structural supercapacitors using a solid resin electrolyte with carbonized electrospun cellulose/carbon nanotube electrodes,” *J. Mater. Sci.*, vol. 53, no. 20, pp. 14598–14607, Oct. 2018, doi: 10.1007/s10853-018-2665-x.
- [90] R. Vicentini, L. M. Da Silva, E. P. Cecilio Junior, T. A. Alves, W. G. Nunes, and H. Zanin, “How to Measure and Calculate Equivalent Series Resistance of Electric Double-Layer Capacitors,” *Molecules*, vol. 24, no. 8, p. 1452, Apr. 2019, doi: 10.3390/molecules24081452.
- [91] D. Yang *et al.*, “Coupled ultrasonication-milling synthesis of hierarchically porous carbon for high-performance supercapacitor,” *J. Colloid Interface Sci.*, vol. 528, pp. 208–224, Oct. 2018, doi: 10.1016/j.jcis.2018.05.050.
- [92] P. Simon and Y. Gogotsi, “Materials for electrochemical capacitors,” *Nat. Mater.*, vol. 7, no. 11, pp. 845–854, Nov. 2008, doi: 10.1038/nmat2297.
- [93] Z. Zou, J. Zhao, J. Xue, R. Huang, and C. Jiang, “Highly porous carbon spheres prepared by boron-templating and reactive H₃PO₄ activation as electrode of supercapacitors,” *J. Electroanal. Chem.*, vol. 799, pp. 187–193, Aug. 2017, doi: 10.1016/j.jelechem.2017.06.005.
- [94] M. Canal-Rodríguez, A. Arenillas, N. Rey-Raap, G. Ramos-Fernández, I. Martín-Gullón, and J. A. Menéndez, “Graphene-doped carbon xerogel combining high electrical conductivity and surface area for optimized aqueous supercapacitors,” *Carbon*, vol. 118, pp. 291–298, Jul. 2017, doi: 10.1016/j.carbon.2017.03.059.
- [95] D. Zhang *et al.*, “Scalable synthesis of hierarchical macropore-rich activated carbon microspheres assembled by carbon nanoparticles for high rate performance supercapacitors,” *J. Power Sources*, vol. 342, pp. 363–370, Feb. 2017, doi: 10.1016/j.jpowsour.2016.12.072.
- [96] D. Zhang, C. He, Y. Wang, J. Zhao, J. Wang, and K. Li, “Oxygen-rich hierarchically porous carbons derived from pitch-based oxidized spheres for boosting the supercapacitive performance,” *J. Colloid Interface Sci.*, vol. 540, pp. 439–447, Mar. 2019, doi: 10.1016/j.jcis.2019.01.038.